ABSTRACT

Title of Dissertation: Synthesis and Characterization of Binary Clusters to Controllable Binary Nanoparticles "The New Role of Zintl Anions"

Melanie J Moses, Doctor of Philosophy, 2004

Dissertation Directed By: Professor Bryan W Eichhorn
Department of Chemistry and Biochemistry

Zintl anions are best described as polyatomic main group clusters (i.e. E_7^{3-}; E = P, As, Sb) with structures characteristic of isoelectronic clusters (i.e. hydrocarbon and borohydride clusters). Combining these main group clusters and transition-metal precursors ($Ni(COD)_2$; COD = cyclooctadiene, and $Pd(PCy_3)_2$; PCy_3 = tricyclohexyl phosphine) with very labile ligands allows for the isolation of novel binary molecular clusters. The freedom these structures experience due to the absence of organic ligands lends itself to the very unique structure growth the binary clusters exhibit. Direct oxidation of these binary molecular clusters results in the formation of binary phases (i.e. $PdAs_2$, NiAs, $NiAs_2$). More control of the phase-specific binaries obtained can be achieved by controlling the reaction of the precursors, eliminating the need to isolate the clusters. Binary nanoparticles are in the forefront of heterogeneous catalyst development and application, making this an area of intense investigation. Structural characteristics of the binary clusters, $[As@Ni_{12}@As_{20}]^{3-}$, $[(Ni_2Sb_2)(Sb_7)_2]^{4-}$, $[Ni_5Sb_{17}]^{4-}$, $[Pd_7As_{16}]^{4-}$ and $[Pd_2(E_7)_2]^{4-}$ (E = P, As), and evidence for the formation of

phase-specific binary nanoparticles (Ni_5As_2, $Ni_{11}As_8$, NiAs and $NiAs_2$) under very mild conditions will be presented.

SYNTHESIS AND CHARACTERIZATION OF BINARY CLUSTERS TO CONTROLLABLE BINARY NANOPARTICLES
"THE NEW ROLE OF ZINTL ANIONS"

By

Melanie Jean Moses

Dissertation submitted to the Faculty of the Graduate School of the
University of Maryland, College Park, in partial fulfillment
of the requirements for the degree of
Doctor of Philosophy
2004

Advisory Committee:
Professor Bryan Eichhorn, Chair
Professor Lawrence Sita
Associate Professor Ichiro Takeuchi
Assistant Professor Doug English
Assistant Professor Andrei Vedernikov

Dedication

In memory of my dad, Frank S. Moses, IV, for making me believe I could do anything I put my mind to, and in memory of my high school chemistry teacher, Kevin Brown, for fascinating me with all the aspects of chemistry. Both were great men who were lost to early and are sorely missed.

Acknowledgements

I would like to express my enormous appreciation to my advisor, Prof. Bryan Eichhorn for the guidance and support he has given me over the past years. Working with him has expanded my appreciation for inorganic chemistry and science as a whole. The confidence I have attained from the many conversations we have had will benefit me in my future scientific endeavors and life in general.

I am also indebted to Dr. Jim Fettinger for the time and effort he put into determining the many complicated crystal structures. I want thank Dr. Bindu Varughese for collecting the XPS data and giving me guidance in how to fit my data. The instructions of Tim Maugel were invaluable in my ability to run the SEM/EDAX and TEM microscopes. I also want to thank him for the SEM image used in Chapter 5. Thanks to Kevin McIlwrath at Hitachi for the HRTEM images.

I want to bestow a tremendous amount of gratitude to my past and present labmates and friends for helping me keep my sanity: Dr. Banu Kesänli, Dr. Serpil Gönen, Chad Stoltz, Emren Nalbant-Esentürk, Capt. D'Anne Spence, Oktay Demircan, Dr. K. Ramesha, Shenghu Zhou, Selim Alayoglu, Dan Paluchowski, and Jordan Halsig. My friends outside of the lab also provided my a great deal support and friendship: Stefanie Kotch, Dr. Frank Kotch, Dr. Suzanne Bogaczyk, Dr. Chai Engtrakul, Dr. Trent Vorlicek, Kathleen Dwyer, Carla Neuberger, Bill McElroy, Andy Kung, Allison Madsen, Rahul Goel, Dr. Bhakti Petigara, and Fiaza Malik.

My family has given me constant support and encouragement throughout my life and especially during my graduate career. I want to thank my Mom and Dad fro teaching me I could do anything I set my mind to. I have the best sisters I could ask

for in Jenni, Beth and Stephanie. Thank you to my brother-in-law, Chris, and my nephew, Knox, for always make my trips home enjoyable.

Table of Contents

List of Tables

List of Figures and Schemes

Chapter 1:

Introduction

1.1 Introduction

Interest in the construction of customized nanomaterials from small molecular clusters has been growing ever since the isolation of C_{60}.[1] Size control and elemental composition are currently of most interest. The use of binary clusters with known sub-nanometer size and elemental composition are ideal precursors for binary nanoalloys. Molecular binaries have distinctly different properties than bulk phase binaries. Binary phase nanomaterials have been known to have properties that are distinctly different from both the molecular and bulk phase binaries; such as different "band edge" luminescence spectrum that change with particle size of CdSe and CdS.[2,3] The potential of new properties afforded by nanoparticles of binary phases opens up new possibilities in the magnetic, catalytic and optical industries.

Transition-metal / main group binary nanoparticles are of great interest in the boom of nano-regime investigations. Presently, chalcogenide binaries receive a large portion of the attention due to their superconducting properties and the quantum effects on their photophysical and photochemical properties displayed in this size range.[4,5] While their practical applications may have fueled the insurgence of investigations, the available synthetic methods for preparing the binary nanomaterials have allowed the chalcogenide phases to remain at the forefront of scientific interest.[6]

Other transition-metal / main group phases in the nanometer size range have attracted some attention.[7,8] However, the properties and applications of these materials in the nano-regime have not been as well studied. In some cases, they have never been investigated due to the lack of synthetic methods available to prepare the binary nanoparticles. Transition-metal tetrelide (group 14) binaries have been shown to enhance metallic catalysts (i.e. Pt/Sn)[9,10], but scientists are uncertain which phase is responsible for the enhancement.[11] Transition-metal pnictide (group 15) binaries, on the other hand, have received even less attention.

While methods for synthesizing binary nanomaterials have progressed due to the use of cluster precursors that contain preformed transition-metal - main group bonds, the cluster precursors have stabilizing ligands that often contaminate the resulting nanoparticles.[12-14] Zintl ion precursors are polyatomic main group clusters free of supporting ligands. Therefore, if transition-metal precursors with labile ligands are employed, binary complexes free of stabilizing ligands should be accessible. Traditionally, reported transition-metal / Zintl ion complexes have ligands (i.e. PR_3 and CO) stabilizing the transition-metal fragments. Dramatically fewer ligands are involved in stabilizing the Zintl complexes compared to other transition-metal / main group complexes.[15,16] Efforts to remove the ligands from Zintl ion complexes after formation have been unsuccessful.[17,18]

The objective of the research presented in this thesis was to 1) isolate ligand-free transition-metal / pnictogen Zintl ion binary complexes, 2) study their structure

and bonding, and 3) to employ the charged binary anions to develop a generic but controllable phase-specific synthetic route to nanoparticles.

In the next section, an overview of Zintl complexes, which are integral to every aspect of this thesis, will be presented. In the following section, the evolution of binary phases with special attention given to transition-metal / pnictogen phases will be presented.

1.2 Zintl Chemistry

Initial work in this are began in the 1890's by Johannis, when he dissolved sodium and lead metal in liquid ammonia.[19,20] The mixture resulted in a green solution that later decomposed precipitating out $NaPb_4$ and $NaPb_2$, depending on conditions.[21] A few decades later in the early 20th century electrolysis studies by Kraus indicated that these solutions behaved in the same manor as salts.[22] Thus, suggesting that anions of metallic elements can occur (Pb_2^{1-}) if in the presence of more electropositive elements (Na^{1+}). Other electrolysis studies that followed on newly discover metallic anions indicate that reactions of sodium and lead produce solutions that contain 2.25 Pb atoms for every Na atom.[23] Similarly, reactions of sodium and excess antimony give solutions with a maximum of 2.33 Sb atoms for every Na atom.[24] Restricted to the recently determined negative charges assigned to metallic anions, in which group 16 (chalcogens) anions carry a -2 charge, the group 5 (pnictogens) anions carry a -3 charge and group 4 (tetrels) anions carry -4 charges,

Kraus determined the formulas of these two salts were $Na_4Pb{\bullet}Pb_8$ and $Na_3Sb{\bullet}Sb_6$ and in solution were present as anions, Pb_9^{4-} and Sb_7^{3-}, respectively.[25]

However, it is the work of Eduard Zintl, in the 1930's, that is best known in the area of polyatomic main-group anions. Potentiometric titration of normal-valent, main-group metal salts (i.e. PbI_2) into liquid ammonia solutions of metallic sodium were used to elucidate a variety of polyatomic anions of main-group metals, according to equation 1.1.[26]

$$(4+2x)\ Na + x\ PbI_2 \rightarrow Na_4Pb_x + 2x\ NaI \qquad \textit{1.1}$$

Extensive studies by Zintl suggested that E_9^{4-} (E = Pb, Sn), E_7^{3-} (E = Sb, Bi), E_5^{3-} (E = As, Bi), E_3^{3-} (E = As, Sb, Bi) and some Se and Te polyatomic anions could by prepared by electrochemical methods.[26-28] It was this massive contribution to this area of research that eventually resulted in these polyatomic anions being labeled as "Zintl ions".

The X-ray crystal structure of $Na_4(en)_7Sn_9$ was the first confirmation that any of the Zintl ions proposed by Zintl existed, Sn_9^{4-}.[29] A study reporting[30] enhanced solubility of alkali metals by adding 2,2,2-crypt, [4,7,13,16,21,24-hexaoxa-1,10-diazobicyclo(8,8,8)hexaxcosane], steered Corbett's group in the mid 1970's to use the macrocyclic molecule to help isolate crystals of the Zintl ions.[31] Using 2,2,2-crypt to sequester the alkali metals of the Zintl salts many of the anions proposed by Zintl, as

well as other polyatomic anions, have been crystallographically determined; including E_9^{4-} (E = Ge, Sn), Ge_9^{2-}, E_5^{2-} (E = Sn, Pb, Bi), E_4^{2-} (E = Sb, Bi), E_{11}^{3-} (E = As, P), E_7^{3-} (E = As, Sb, P) and P_{16}^{2-}.[31-42] Some of the structural variety in these Zintl ions are illustrated in figure 1.1.

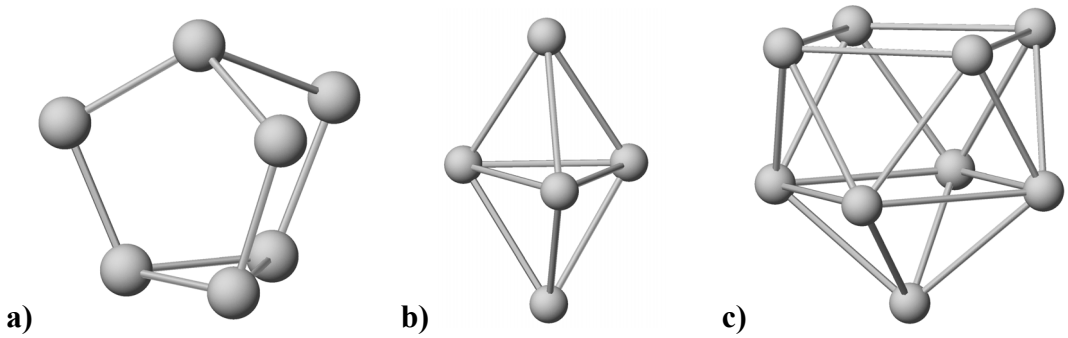

Figure 1. 1. Structural orientation of some isolated Zintl ions. a) E_7^{3-}, b) E_5^{2-}, and c) E_9^{4-}.

The tetrel polyatomic cluster anions have structures similar to the borohydrides and are electron deficient. However, pnictogen Zintl ions form polycyclic hydrocarbon-like clusters, such as E_7^{-3} (E = P, As, Sb) (figure 1a), and are electron precise where E and E^- (E = P, As, Sb) are isoelectronic to CH and CH_2, respectively. Work presented in this thesis will focus on the chemistry involving the pnictogen Zintl ions.

Once the pnictogen Zintl ions were structurally characterized by X-ray crystallography, interest in their reactivity grew. With the alkali metal sequestered by 2,2,2-crypt, the strong ion pairing between the alkali metal and the Zintl anion is diminished making it easier for the Zintl ions to react with transition-metals in solution. The crystallographic structures of the first transition-metal / Zintl ion

complexes were reported in the 1980's, $[Cp(CO)_2Fe]_3P_7$ and $^1_\infty[(Rb{\bullet}NbAs_8)^{2-}]$.[43,44] While both of these clusters can be considered Zintl complexes, a Zintl ion precursor was only used in the isolation of $[Cp(CO)_2Fe]_3P_7$.

The first structurally characterized transition-metal / Zintl ion complex in which a Zintl ion precursor had under gone a topological rearrangement was the $[Rb(2,2,2\text{-crypt})]^{1+}$ salt of $[(CO)_3CrAs_7]^{3-}$, according to equation 1.2.[16]

$$Rb_3As_7 + Cr(CO)_3(\eta^6\text{-}Me_3C_6H_3) + 2(2,2,2\text{-crypt}) \xrightarrow{en/tol} [Rb(2,2,2\text{-crypt})]_3[(CO)_3CrAs_7] \qquad 1.2$$

The anion $[(CO)_3Cr(\eta^4\text{-}As_7)]^{3-}$ has an As_7 norbornadiene-like cage (figure 1.2a) that differed from $[Cp(CO)_2Fe]_3P_7$, which maintains the nortricyclic-like E_7 arrangement of the parent E_7^{3-} Zintl ion. Continued studies of the reactivity of transition-metal precursors with E_7^{3-} (E = P, As, Sb) Zintl ions indicated that this Zintl ion rearrangement from the nortricyclic to the norbornadiene-like structure is quite stable. There are only a few examples of the E_7 transition-metal derivatives that maintain the

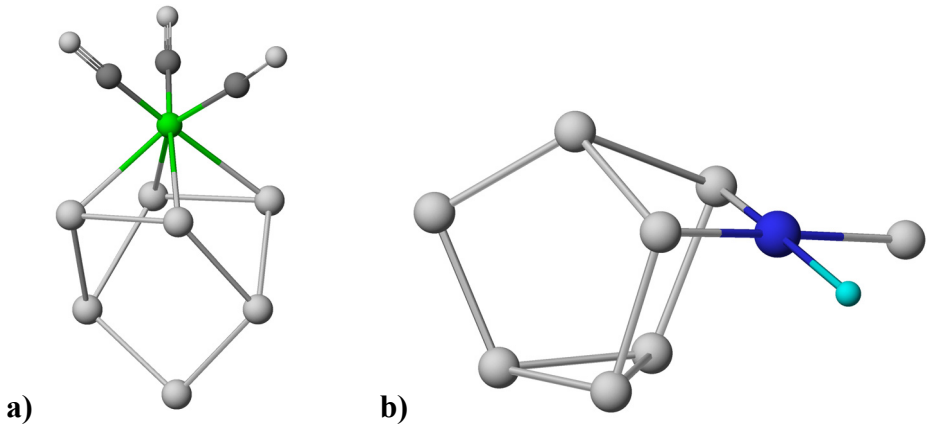

Figure 1. 2. Structural representation of a) $[(CO)_3Cr(\eta^4\text{-}As_7)]^{3-}$ and b) $[(PPh_3)HPt(\eta^2\text{-}E_7)]^{2-}$. The benzene groups of the phosphine ligand in (b) have been omitted for clarity.

nortricyclic arrangement (e.g. $[(PPh_3)HPt(\eta^2\text{-}E_7)]^{2-}$ (E = P, As) (figure 1.2b and) and $[Cp(CO)_2Fe]_3P_7$.[45,46],[43]

Other studies have utilized different pnictogen Zintl ions, such as LiP_5. This anion reacts with metal hexacarbonyl precursors to give $[M(CO)_3(\eta^5\text{-}P_5)]^n$ (M = Cr, Mo, W; n = 1-, M = Mn; n = 0).[47] However, the majority of transition-metal / pnictogen Zintl ion research has focused on the use of the E_7^{3-} (E = P, As, Sb) ions. In the mid-1990's, interest in transition-metal / Zintl ion complexes grew. Bolle et. al. isolated the isostructural antimony-molybdenum analog of $[(CO)_3CrAs_7]^{3-}$, $[(CO)_3MoSb_7]^{3-}$.[48] Shortly after that, Charles et. al. reported the synthesis, structure, bonding, and spectroscopy of the entire isostructural series of $[(CO)_3ME_7]^{3-}$ (M = Cr, Mo, W; E = P, As, Sb).[18] He proceeded to study the reactivity of this metallated Zintl ion series. Protonation, alkylation and metallation of the $[(CO)_3MP_7]^{3-}$ (M = Mo, W) series indicated that the most reactive site of the anions was at the apical pnictogen atom of the norbornadiene-like cages, E1 site (scheme 1.1).[17] Interestingly, when the

P_7 analogs were exposed to carbon monoxide gas, the metal atoms coordinated a fourth CO ligand and rearranged back to a nortricyclic arrangement similar to $[(PPh_3)HPtP_7]^{2-}$.[17] Scheme 1.1 highlights the reactive studies on $[(CO)_3WP_7]^{3-}$.

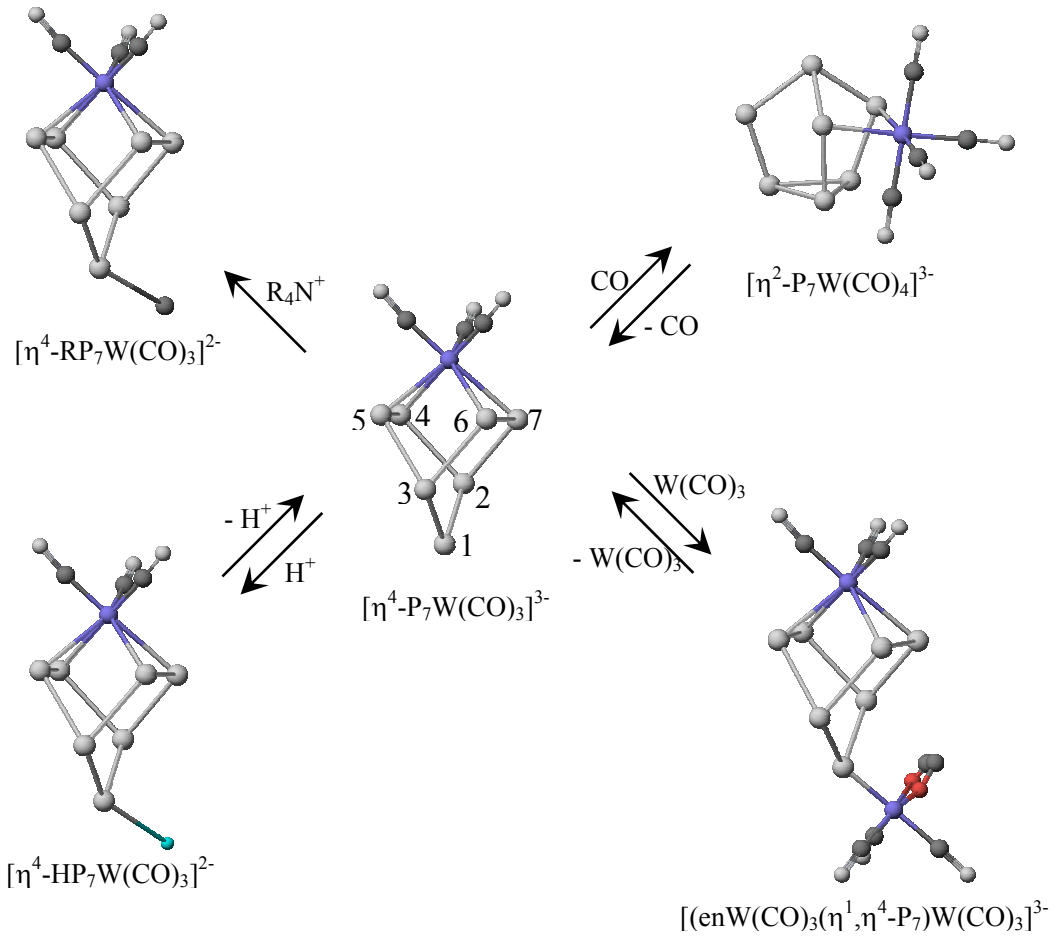

Scheme 1. 1

The reaction of $Ni(CO)_2(PPh_3)_2$ and K_3P_7 in the presence of both 2,2,2-crypt and Bu_4PBr gave $[(CO)Ni(\eta^4\text{-}HP_7)]^{3-}$.[45] This anion is isoelectronic to $[(PPh_3)HPt(\eta^2\text{-}P_7)]^{2-}$ (figure 1.2b) but is in a norbornadiene-like arrangement similar to the $[(CO)_3MP_7]^{3-}$ complexes previously discussed. However, when the same nickel

precursor is reacted with K_3Sb_7 giving $[(CO)_3Ni_3Sb_7]^{3-}$, an entirely new structure type was obtained.[49] The structure of $[(CO)_3Ni_3Sb_7]^{3-}$ (figure 1.3a) can be considered to have a 10-atom nido-$[Ni_3Sb_7]$ core. This structure type is more reminiscent of the deltahedral structures seen for the tetrel Zintl complexes rather than another known pnictogen complexes.

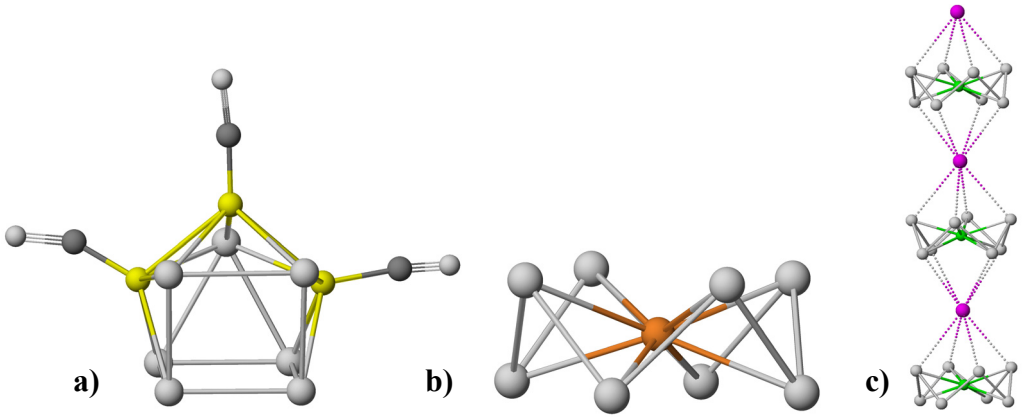

Figure 1. 3. Structural representation of a) $[(CO)_3Ni_3Sb_7]^{3-}$, b) $[MoAs_8]^{2-}$, and c) a piece of the chain polymer $^1{}_\infty[(K{\bullet}CrAs_8)^{2-}]$.

One of the first transition-metal / Zintl ion complexes, $^1{}_\infty[(Rb{\bullet}NbAs_8)^{2-}]$, was not synthesized from a Zintl ion precursor, but the As_8 crown-like ring could be considered a Zintl ion. The As_8 structure has never been isolated as a free-Zintl ion; however, the As_8^{8-} ion is isoelectronic to both cyclooctane (C_8H_{16}) and S_8, where each two atom coordinated As^{1-} is isoelectronic to CH_2 and S. This complex was unique from other transition-metal / Zintl ion complexes because it was free of carbon-containing ligands. Transition-metal precursors with more labile ligands than the

phosphines and carbonyls that have been used before must be employ to make this complex by way of a typical Zintl ion synthesis (equation 1.3),

$$K_3E_7 + ML_x + n(2,2,2\text{-crypt}) \rightarrow [K(2,2,2\text{-crypt})]_n[L_yME_z] + (x\text{-}y)L \qquad 1.3$$

Eichhorn et. al. succeeded in using the highly labile Mo(Me-naphthalene)$_2$ to isolate $[MoAs_8]^{2-}$ (figure 1.3b), which is analogous to the subunit of the $^1{}_\infty[(Rb{\bullet}NbAs_8)^{2-}]$ polymer chain.[44] Further work by Kesanli et. al. in the early 21st century extended these carbon-free binary clusters to include $[ME_8]^{n-}$ (M = Cr, Mo, Nb; E = As, Sb; n = 2, 3) and a one-dimensional chain polymer, $^1{}_\infty[(K{\bullet}CrAs_8)^{2-}]$ (figure 1.3c) using M(naphthalene)$_2$ (M = Cr, Mo) and Nb(toluene)$_2$ as precursors, respectively.[50,51] The only other transition-metal / pnictogen Zintl ion binary cluster free of hydrocarbyl ligands is $[Ti(P_5)_2]^{2-}$; however, it was not isolated from a Zintl ion precursor.[52]

Employing precursors with more labile ligands is the most efficient way to obtain carbon-free transition-metal / Zintl ion clusters. Efforts were made to remove CO and PPh_3 ligands from existing complexes by methods such as oxidative decarbonylation and thermoylsis but were unsuccessful.[18,45] The complexes presented in the following chapters discuss the preparation of new carbon-free transition-metal / Zintl ion clusters.

1.3 Binary Phases

Interest in the binary clusters free of organic and organometallic ligands that can be obtained using Zintl ions arise not just from interest in better understanding the chemistry of inorganic anions but also their use as material precursors. Carbon-free transition-metal / Zintl ion clusters are unique precursors to binary phases that only require removal of a few electrons. A variety of applications for transition-metal / main group binaries have been developed over the years, from optical and semiconductor materials to catalysis.[53-58]

The synthesis of bulk binary phases of transition-metals and main group elements has been well studied. Various stoichiometric phases, which vary with each pair of elements, can be accessed by high temperature reactions of appropriate ratios of the elements. Other methods for isolating binary phases of transition-metals and either pnictides or chalcogenides have been used, such as electroplating, single or dual-source chemical vapor deposition and direct reduction of metal oxoanion precursors.[59-61] However, high temperature elemental combination reactions are the most universally applicable method for making bulk binary phases. Most transition-metal pnictide (phosphorous, arsenic and antimony) binary systems have a wide range of known phases, such as the Ni/P system which has eight different stoichiometric phases.[62] Binary chalcogenide systems, on the other hand, generally have only one or two different stoichiometric phases.

Recently, a new method for synthesizing binary transition-metal pnictides through a liquid-mediated metathetical synthesis has been reported.[63] Metal (II)

halides and sodium pnictides were refluxed in toluene for two days, according to equation 1.4.

$$3MX_2 + 2Na_3E \xrightarrow[\Delta]{tol} 2ME + 6NaX + M \qquad 1.4$$

(M = Ni, Co; E = P, As, Sb; X = Cl, Br)

The toluene solvent employed in this reaction (eq. 1.4) provides a heat sink for the highly exothermic metathesis reaction keeping the temperature of the reaction around its 110.6 ºC boiling point. The metal and salt byproducts are removed when the samples are washed. The resulting binaries are amorphous with particles in the 2-5 μm size range. After annealing of the amorphous material at 500 ºC for 48h, powder X-ray diffraction confirmed the phases isolated. This method is an alternative for preparing a variety of binary phase but does not offer control over the specific phases formed.

Early work on lower temperature reaction methods of bulk binary phases were not directed toward preparing nanoparticles[63] but the lower temperature approaches frequently resulted in nanoparticles. The materials in the nano-size regime often have properties distinctly different from their bulk phase counter-parts. This was recently exemplified by a study on the catalytic properties of gold nanoparticles.[64] Bulk gold shows no catalytic activity towards CO oxidation reactions nor do most sizes of gold

nanoparticles. However, 1.4 nm (55 atom) gold nanoparticles show a surprising efficiency as CO oxidation catalysts,[65] hinting at the vast chemistry that may be accessible by materials in the nano-regime.

Many of the methods employed for the formation of transition-metal / main group binary phases as nanoparticles alter only slightly from bulk phase preparation methods. Parkin et. al. modified their liquid-mediated metathetical approach to bulk transition-metal pnictides, previously mentioned, successfully isolating metal pnictide and chalcogenide binary nanoparticles at lower temperatures.[66] The main difference is that liquid ammonia is used as a solvent in place of the toluene used in equation 1.4. By switching the solvent, the reaction proceeds at room temperature, likely mediated by a solvent initiated change in state and driven by exothermic production of sodium chloride. The liquid ammonia metathesis reactions reportedly produce binary particles that are smaller than 100 nm and agglomerate into 1-8 μm aggregates.

Gopalakrishnan et. al. reduced metal oxoanion precursors (i.e. $CoAs_2O_6$, $NH_4NiAsO_4 \bullet CH_3CN \bullet 2H_2O$, $NH_4MnPO_4 \bullet H_2O$) with H_2 gas at elevated temperatures (400 – 1000 ºC) to produce single-phase binary products that match the precursor compositions.[61] A few metal phosphate precursors do not produce binary phases of corresponding compositions producing instead single-phase binary products with a

lower P:M ratio. The excess phosphorous is present as an elemental by-product (i.e. equation 1.5).[61]

$$RuP_2O_7 + {}^{17}/_2\, H_2 \rightarrow RuP + P + {}^{3}/_2\, H_2 + 7\, H_2O \qquad 1.5$$

The reduction method of metal oxoanion precursors for obtaining single-phase binary materials was enhanced by Brock et. al. to attain the binary phosphide materials as nanoparticles.[8] Brock's group determined that aggregation of the material could be suppressed by immobilizing the phosphate precursors on a single-crystal mica support before the reduction step. By reducing the concentration of the phosphate precursor, even smaller particles could be obtained. The lower precursor concentration facilitated deposition on the mica substrate with increased particle separation. Therefore, despite the high reduction temperatures required to obtain phase pure-FeP (700 ºC) and Fe_2P (1100 ºC), agglomeration that would normally occur at these temperatures is halted producing 1.41 ± 0.5 nm FeP particles (0.19 mg/mL precursor concentration).

It was expected that the reduction of metal oxoanion precursor immobilized on a substrate would be a general method for wide range of metal / pnictogen binary phases.[8] However, attempts to extend this method to MnP nanoparticles were unsuccessful.[67] The MnP nanoparticles were eventually obtained through decomposition of organometallic precursors ($Mn_2(CO)_{10}$ and $P(SiMe_3)_3$) in the

presence of coordinating solvents like triocylphosphine oxide (TOPO) or triocylphosphine (TOP).[67] These solvents have high boiling points that allow the reactions to be conducted at elevated temperature (up to 350 ºC for TOPO), which enhances nanoparticle crystallinity. The long carbon chains of these coordination solvents prevent particle agglomeration when they coordinate to growing particles, see scheme 1.2. At a temperature of 220 ºC for 24 hours in a TOPO/ myristic acid solution, monodispersed spherical particles of MnP (5.11 ± 0.48 nm) are achieved. Efforts to extend the decomposition method using $P(SiMe_3)_3$ to Fe_2P proved unsuccessful. However, this method can be used to obtain similar sized

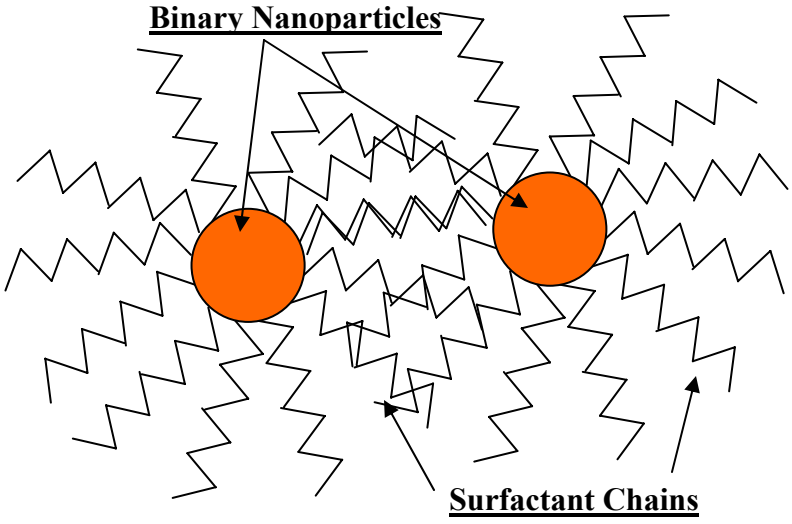

Scheme 1. 2

nanoparticles of FeP and CoP by adjusting the transition-metal precursors.[68] The high reactivity and expense of $P(SiMe_3)_3$ make it an unfavorable precursor. The Brock group reported that TOP could be used as both the phosphorous precursor and a

coordinating solvent with nanoparticle size and quality similar to those obtained using $P(SiMe_3)_3$ for the production of both MnP and FeP phases.

While phosphide binary phases dominate the research aimed at transition-metal pnictide nanoparticles, a few arsenide phases have been studied. Two low-temperature methods for single-phase FeAs, CoAs and NiAs nanoparticles are known. Reduction of transition-metal chlorides by potassium borohydride in the presence of arsenic metal under ultrasonic mixing condition and subsequent heating at 100 ºC for 24 hours produces nanoparticles of FeAs, CoAs and NiAs (35, 30, 20 nm, respectively), see equation 1.6.[69]

$$MCl_x + As + KBH_4 \xrightarrow[\Delta]{en} MAs + KCl + H_2 \qquad 1.6$$

M = Fe (x = 3), M = Co or Ni (x = 2)

The second low-temperature method uses zinc powder to reduce the metal chloride instead of potassium borohydride and is carried out in an ethanol solution.[7] The reduced metal reacts with elemental arsenic when irradiated with a high intensity ultrasonic probe for 4 hours at room temperature. This sonochemical method was applied to iron, cobalt and nickel chlorides to give monoarsenide nanoparticles of FeAs, CoAs, and NiAs (18, 20, 12 nm, respectively).

Both of the methods for the production of metal monoarsenide phases as nanoparticles are closely related to a previously known solvothermal reaction for FeAs nanoparticles.[70] The previously known method uses zinc metal as a reducing agent in an ethanol solution of iron chloride and the highly toxic $AsCl_3$ at 150 ºC. In light of the two newer methods which use less toxic elemental arsenic to excess to the monoarsenide binary phases, this solvothermal reaction using $AsCl_3$ is no longer a desirable method.

Nanoparticle formation of metal chalcogenide phases have been more extensively investigated than pnictide binary phases. The increased interest in smaller devices that require quantum-dots (small semiconductors) is likely one reason concentrated interest in transition-metal chalcogenide nanoparticles.

Single-source molecular precursors that contain both the transition-metal and chalcogenide elements, metal dithio- and diselenocarbamante complexes, can be used to produce CdS, ZnS, ZnSe, and CdSe nanoparticles.[71] This method proceeds by thermal decomposition of the single-source precursors in coordinating solvents (TOPO and TOP).

The single-source decomposition method proved to be even more successful when inorganic clusters were used as the single source precursors.[13] The structures of inorganic clusters used in the thermal decomposition method, $[M_{10}Se_4(SPh)_{16}]^{4-}$ (M = Cd, Zn), have cores that are discrete pieces of MSe bulk phases surrounded by phenyl thiolate ligands. The MSe core presumably acts as a template for particle formation,

and the alklyamine solvent (hexadecylamine) passivates the surface to produce spherical nanoparticles.

Similarly, $[Cd_{10}S_4Br_4(SR)_{12}]^{4-}$, which has a tetra-adamantane core that resembles a piece of cubic CdS, can be used to generate CdS nanoparticles.[14] The heating of the Cd/S cluster and six equivalents of elemental sulfur are needed to obtain the CdS nanoparticles. A coordinating solvent is not needed to passivate the surface of CdS particles, but the lack of a coordinating solvent does produce a higher degree of polydispersity.

A variety of preparation methods from the literature sources have been outlined here for metal pnictide nanoparticles. Each transition-metal pnictogen binary system is comprised of multiple different phases. However, the methods presented in the literature generally only allow access to the most thermally stable phase from the respective binary systems. A new preparation method for binary nanoparticles (Ni/As) which allows selective single-phase preparation of every phase on the phase diagram (Ni_5As_2, $Ni_{11}As_8$, NiAs and $NiAs_2$) is presented in this thesis.

1.3 Organization

In the proceeding chapters of this thesis, the synthesis and characterization of several transition-metal / Zintl ion binary anions, their use as precursors to binary nanoparticles, and the use of the Zintl ion, As_7^{3-}, to access the entire Ni/As binary phase diagram producing single-phase binary nanoparticles of each phase are presented.

The synthesis and characterization of a very novel cluster which contains an unprecedented As_{20} fullerene-like cage, $[As@Ni_{12}@As_{20}]^{3-}$, will be presented in Chapter 2. Chapter 3 presents a new preparation method for Ni/As binary phases using the Zintl ion, As_7^{3-}, which allows all known Ni/As binary phases (Ni_5As_2, $Ni_{11}As_8$, NiAs, and $NiAs_2$) to be selectively isolated at near room-temperature conditions. The synthesis of $[(Ni_2Sb_2)(Sb_7)_2]^{4-}$, $[Ni_5Sb_{17}]^{4-}$ and $[Pd_7As_{16}]^{4-}$, and discussion on the unique structure and bonding of these anions is presented in Chapter 4. Chapter 5 discusses the synthesis and characterization of $[Pd_2(E_7)_2]^{4-}$ (E = P, As) and the use of the inorganic cluster, $[Pd_2(As_7)_2]^{4-}$, as a single-source precursor to Pd/As binary phase nanoparticles. Chapter 6 summarizes the importance of the research presented in chapters 2-4. It outlines how this research advances scientific knowledge of inorganic anionic clusters and preparation of controllable binary nanoparticles.

Chapter 2

Interpenetrating As_{20} Fullerene and Ni_{12} Icosahedra in the Onion-Skin $[As@Ni_{12}@As_{20}]^{3-}$ ion

2.1 Introduction

The high symmetry often encountered in large inorganic polyhedral cages presents very interesting bonding environments. The high connectivity of atoms in these cages imparts unusual stability and/or reactivity. Interest in this area grew with discovery of carbon fullerenes.[1] The carbon fullerenes were named for there resemblance to the architectural geodesic dome of Buckminster Fuller.[72] Carbon fullerenes are comprised of an icosahedral array of pentagonal rings that are interconnected by hexagonal rings. The carbon atoms are sp^2 hybridized connected by a 2c-2e sigma bonded network and a conjugated π system. Geodesic domes have a similar icosahedral arrangement of pentagonal rings connected by hexagonal rings; however, there is a vertice slightly above the centroid of every 5 and 6-member ring, which creates triangular faces. It is the network of triangular faces that provides architectural support to the geodesic domes.

The similarities between fullerenes and heavy element polyhedra of the carbon subgroup known as Zintl ions (i.e. E_9^{4-}, E = Ge, Sn, Pb) have been more recently noted, such has there high symmetry and reactivity.[73] Extension of the chemical studies and applications on the carbon fullerenes to inorganic "fuller" cages,

which structurally resemble the 5 and 6-member framework of carbon fullerenes, has received much attention. A few carbon-free fullerene cages, In_{70}, In_{74} In_{78} and M_{60} ($M = Na_{12}In_{48}$), have been experimentally isolated in extended solids, $Na_{96}In_{97}Z_2$ (Z = Ni, Pd).[74] Another carbon-free fullerene-like cluster, Si_{20} cage, was also seen as part of the clathrate-II compound, $Cs_8Na_{16}Si_{136}$.[75] However, all of these examples occur as parts of three dimensional extended solids unlike the free-standing carbon fullerenes.

Many theoretical studies in the area of both organic and inorganic fullerenes have been reporte since the first report on C_{60}. While free-standing inorganic fullerenes have not been crystallographically isolated, they have not escaped scrutiny by the theoretical community. According to some studies, the stability of E_{20} dodecahedral cage, smallest possible fullerene, from the pnictogen family (group 15) vary going down the periodic table.[76] The carbon atoms of the fullerenes can sp^2 hybridize which makes π-bonding favorable. Double bonds between heavier pnictogen elements are less stable and are not favored to form. Therefore, the formation of E_{20} pnictogen fullerene-like cages would favor a sigma bonding framework with the atoms sp^3 hybridized. The high stability of N_2 and P_4 make crystallization of N_{20} and P_{20} less favorable.[77,78] However, the stability of P_{20} is approaching the stability of P_4. Further theoretical studies indicate that this trend of increasing stability from N_{20} to P_{20} over their respective smaller polyatomic cluster extends to As_{20} and As_4, which have similar stabilities. Some theoreticians believe that this trend will continue for the remaining E_{20} vs. E_4 pnictogens, E = Sb and Bi.[76]

Herein, the synthesis and characterization of the first free-standing inorganic fullerene in the $[As@Ni_{12}@As_{20}]^{3-}$ ion, **2.1**, is presented. Since the report[79] of $[Bu_4P]_3[As@Ni_{12}@As_{20}]$•1.5en, new theoretical studies on the dodecahedral As_{20} cage have emerged and will be addressed by comparison to experimental results.[80]

2.2 Results

2.2.1 Synthesis

Ethylenediamine (en) solutions of K_3As_7 and $Ni(COD)_2$ react in the presence of Bu_4PBr to give air sensitive black, needle-like crystals of $[Bu_4P]_3[As@Ni_{12}@As_{20}]\cdot$ 1.5en , in a 37% yield. The complexity of the chemistry involved in this reaction and the low yield making writing a balanced equation difficult, which is common in Zintl chemistry. Reductive decomposition of excess Bu_4PBr and/or reductive fragmentation of Zintl ions, As_7^{3-}, are potential sinks for electrons generated in the oxidative coupling production of $[Bu_4P]_3[As@Ni_{12}@As_{20}]\cdot$ 1.5en. The complex was characterized by laser desorption ionization time-of-flight mass spectrometry (LDI-TOF-MS), EDX, single crystal X-ray diffraction and extended Hückel calculations. Unit cells of crystals isolated from multiple reaction mixtures were obtained by single crystal X-ray diffraction to confirm the consistence synthesis of the $[As@Ni_{12}@As_{20}]^{3-}$ complex.

2.2.2. Solid State Structure

The $[Bu_4P]_3[As@Ni_{12}@As_{20}]\cdot 1.5en$ salt has monoclinic crystal structure with $P2_1/n$ crystal symmetry. The unit cell has non-interacting anions, cations and solvent molecules. The cell is well ordered except for one en solvate molecule that possesses three orientations. Select crystallographic data is presented in table 2.1. The anion, $[As@Ni_{12}@As_{20}]^{3-}$, **2.1**, consists of an arsenic-centered Ni_{12} icosahedron encapsulated in an As_{20} pentagonal dodecahedron (see figure 2.1). While the anion resides on a general position in the crystal lattice and is devoid of any crystallographically imposed symmetry, both the arsenic-centered Ni_{12} icosahedron and the As_{20} pentagonal dodecahedron have virtual undistorted I_h point symmetry. The overall structure of $[As@Ni_{12}@As_{20}]^{3-}$ has near-perfect I_h point symmetry with average bond distances with standard deviations of 0.025 Å or less. Selective bond distances and angles are summarized in table 2.2.

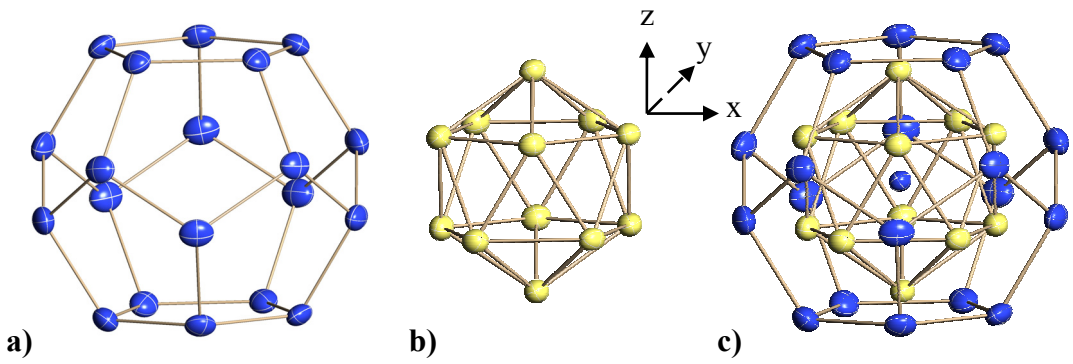

Figure 2. 1. a) An ORTEP drawing of the $[As_{20}]$ dodecahedral subunit of the $[As@Ni_{12}@As_{20}]^{3-}$. b) An ORTEP drawing of the $[As@Ni_{12}]^{3-}$ centered icosahedral subunit of the $[As@Ni_{12}@As_{20}]^{3-}$. c) An ORTEP drawing of the complete $[As@Ni_{12}@As_{20}]^{3-}$ cluster. Blue and gold spheres represent arsenic and nickel atoms, respectively. Ni-As bonds have been omitted for clarity. All thermal ellipsoids are at 50% probability.

The arsenic dodecahedron and nickel icosahedron positions in $[As@Ni_{12}@As_{20}]^{3-}$ make it a unique molecular example of interpenetrating reciprocal platonic polyhedra. The situation is similar to the cube and octahedron in $[Pd_{30}(CO)_{26}(PEt_3)_{10}]$.[81] The 32 atoms of an ideal icosahedral-dodecahedral interpenetrating reciprocal platonic polyhedron are equally distributed on the surface of a sphere. The twelve nickel atoms of the icosahedron in complex **2.1** are positioned such that each of the nickel atoms reside ca. 0.498 Å below the centroid of every pentagonal face of the As_{20} dodecahedron. Therefore, when only the As-As and As-Ni bonds are considered, the 32 atoms create 60 triangular faces giving rise to a "dimpled" golf ball-like structure (figure 2.2 a). If the atoms are projected out from the "dimpled" structure so that all 32 atoms sit on the surface of a sphere (figure 2.2 b), **2.1** can be compared to the revolutionizing architectural discovery of geodesic domes by R. Buckminster Fuller. The $[Ni_{12}@As_{20}]$ unit of **2.1** represents an example of a molecular dodecahedral geodesic dome with a frequency of 1.[72]

Table 2. 1. Crystallographic data for $[Bu_4P]_3[As@Ni_{12}@As_{20}]\cdot 1.5en$.

	$[Bu_4P]_3$(**5.X**) •1.5en
Formula	$C_{51}H_{120}P_3N_3Ni_{12}As_{21}$
Fw	3146.25
T [K]	193(2)
$\lambda_{MoK\alpha}$ [Å]	0.71073
space group	$P2_1/n$
a [Å]	13.6996(4)
b [Å]	23.5192(6)
c [Å]	27.5784(8)
α [˚]	90
β [˚]	93.3250(10)
γ [˚]	90
V [$Å^3$]	8870.9(4)
Z	4
ρ_{calcd} [g cm^{3-}]	2.356
μ [mm^{-1}]	10.344
crystal size [mm]	0.109 x 0.111 x 0.382
reflections collected	140346
independent	20352 [R(int) = 0.0453]
final R [I >2σ(I)]	R1 = 0.0311, wR2 = 0.0755[a]
R indices (all data)	R1 = 0.0616, wR2 = 0.0840[a]

[a]. The function minimized during the full-matrix least-squares refinement was Σw(Fo2-Fc2) where w=1/[σ2(Fo2)+(0.0380*P)2+5.4664*P] and P=max(Fo2,0)+2*Fc2)/3.

Table 2. 2. Select bond distances (Å) and angles (°) for $[As@Ni_{12}@As_{20}]^{3-}$.

As(1)-As(2)	2.7109(6)	As(21)-Ni(9)	2.5512(6)
As(1)-As(5)	2.7598(7)	As(21)-Ni(2)	2.5537(6)
As(1)-As(8)	2.7855(7)	As(21)-Ni(10)	2.5602(6)
As(2)-As(3)	2.7807(7)	As(21)-Ni(12)	2.5617(6)
As(3)-As(4)	2.7343(7)	As(21)-Ni(1)	2.5623(6)
As(4)-As(5)	2.7930(7)		
As(1)-Ni(1)	2.3947(7)	Ni(1)-As(1)-Ni(2)	68.60(2)
As(1)-Ni(2)	2.3966(7)	Ni(1)-As(1)-Ni(6)	68.55(2)
As(1)-Ni(6)	2.3980(6)	Ni(2)-As(1)-Ni(6)	68.16(2)
As(2)-Ni(1)	2.3925(7)	Ni(2)-As(1)-As(5)	109.20(2)
As(2)-Ni(2)	2.3929(7)	Ni(1)-As(1)-As(8)	109.31(2)
As(2)-Ni(3)	2.3945(7)	Ni(6)-As(1)-As(2)	110.15(2)
As(14)-Ni(6)	2.3872(7)	Ni(1)-As(1)-As(2)	55.470(18)
As(14)-Ni(8)	2.3952(7)	Ni(6)-As(1)-As(5)	54.576(18)
As(14)-Ni(7)	2.4038(7)	Ni(1)-As(1)-As(5)	54.907(19)
Ni(1)-Ni(5)	2.6751(7)	Ni(2)-As(1)-As(8)	54.389(19)
Ni(1)-Ni(3)	2.6904(7)	Ni(6)-As(1)-As(8)	54.576(18)
Ni(1)-Ni(4)	2.6972(8)	As(2)-As(1)-As(5)	108.59(2)
Ni(1)-Ni(6)	2.6992(7)	As(2)-As(1)-As(8)	107.90(2)
Ni(1)-Ni(2)	2.7001(8)	As(5)-As(1)-As(8)	107.41(2)
Ni(4)-Ni(10)	2.6674(8)	As(1)-As(2)-As(3)	108.20(2)
Ni(5)-Ni(6)	2.7007(8)	As(2)-As(3)-As(4)	108.13(2)
Ni(9)-Ni(12)	2.6979(7)	As(3)-As(4)-As(5)	107.56(2)
Ni(10)-Ni(12)	2.6926(8)	As(4)-As(5)-As(1)	107.52(2)

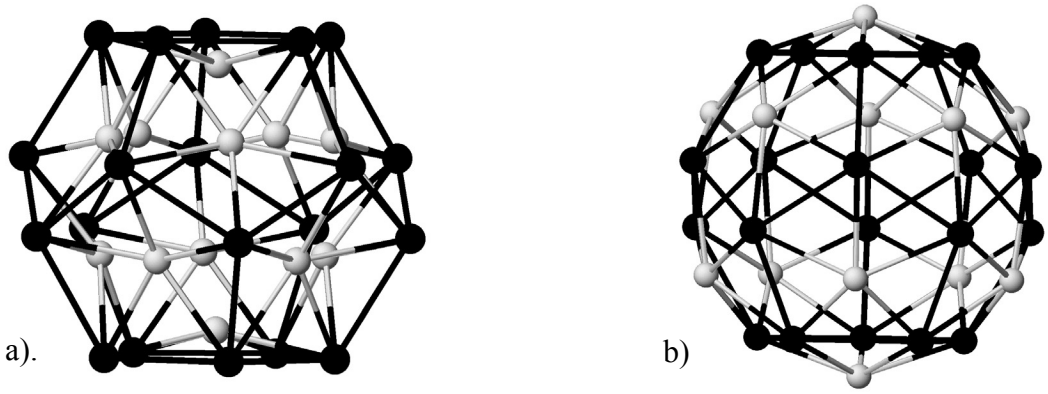

Figure 2. 2. [79] a). "Dimpled" golf ball representation of [As@Ni12@As20]3-. The centered arsenic atom and Ni-Ni bonds have been removed. b). A representation of what the "dimpled" golf ball structure would look like if the nickel atoms were positioned outward from the faces of the As20 cage by 0.498 Å.

The As_{20} pentagonal dodecahedron is the first example of a free-standing inorganic fuller cage; the smallest fullerene structure possible. The overall anion is similar to the endohedral carbon fullerene cages.[82] The diameter of the As_{20} fuller cage of **2.1** is only 10% larger than the C_{60} fuller cage, but only single atoms have been enclosed in crystal structures of the latter.[83]

Each nickel atom in $[As@Ni_{12}@As_{20}]^{3-}$ is within bonding distance of the centered arsenic atom (avg. 2.557 ± 0.012 Å) and is bound η^5 to one face of the dodecahedral arsenic cage (avg. 2.396 ± 0.008 Å). The longer interactions to the centered As atom are still shorter than the Ni-As interaction (2.610 to 2.641(6) Å) between the As atoms and the centered Ni atom in $[Ni_9(\mu_4\text{-}As)_6(PPh_3)_5Cl_3]$.[84] The shorter Ni-As distances are more typical of organometallic complexes (i.e. 2.340(7) to 2.474(6) Å).[85]

The encapsulated icosahedron of **2.1** closely resembles the $[Ni_{12}(\mu_{12}\text{-}E)(CO)_{22}]^{2-}$ (E = Ge, Sn) ions.[86] In comparison, the atomic radius of the centered main group metal appears to control the Ni_{cap}-Ni_{cap} distances of the icosahedra, As (5.16Å) to Ge (5.38Å) to Sn (5.48Å). However, the elongation along a psuedo-C_5 axis reported for the Ge and Sn nickel carbonyl clusters was not seen for the arsenic centered nickel icosahedral cage reported here, making complex **2.1** the only example to have virtual I_h point symmetry. The average Ni-Ni distance of **2.1** is 2.689 ± 0.011 Å, which falls within typical Ni-Ni distance of molecular deltahedra (2.417(2) to 2.846(5) Å).[84,85]

The average arsenic-arsenic distances of the dodecahedral cage are 2.752 ± 0.012Å. This is longer than typical As-As distances[87] of 2.3 to 2.6Å; however, the anion remains intact in the gas phase (see next section).

2.2.3. Laser Desorption Ionization Time-of-Flight Mass Spectrometry

The laser desorption ionization time-of-flight (LDI-TOF) mass spectrum (figure 2.3) was recorded in the negative ion mode from a dried sample of a concentrated dmf solution of complex **2.1**. The most abundant peak in the high mass range of the LDI-TOF mass spectrum represents the oxidized molecular anion of **2.1** with z = 1. The isotopic envelope seen in the MS spectrum at 2278 m/z is in excellent agreement with the simulated pattern for $Ni_{12}As_{21}$ (figure 2.3, inset) confirming the atomic identity of the crystallographic structure. Other peaks are observed that represent a successive loss of arsenic atoms, $[Ni_{12}As_{21-n}]^{1-}$ (n = 0-21), which is consistent with the weak As-As bonding of the dodecahedron. Other cluster series such as $[Ni_{11}As_n]^{1-}$ and $[Ni_{10}As_n]^{1-}$ overlap the mass envelopes of the lower *n*

members the $[Ni_{12}As_{21-n}]^{1-}$ series. These series as well as smaller cluster series seen in the spectra obtained by LDI-TOF-MS suggest that when the arsenic atoms of the As_{20} cage are removed in the gas phase the nickel atoms of the $As@Ni_{12}$ unit are not as stable and can be removed. Resolution of these different series would require tandem MS experiments. Two peaks are also observed at higher mass to charge ratios than $[Ni_{12}As_{21}]^{1-}$ peak which represent the addition of a nickel and arsenic atom, $[Ni_{13}As_{21}]^{1-}$ and $[Ni_{13}As_{22}]^{1-}$. The higher mass peaks are likely the result of a solid state or gas phase reaction that occurs when the sample is ablated by the laser.

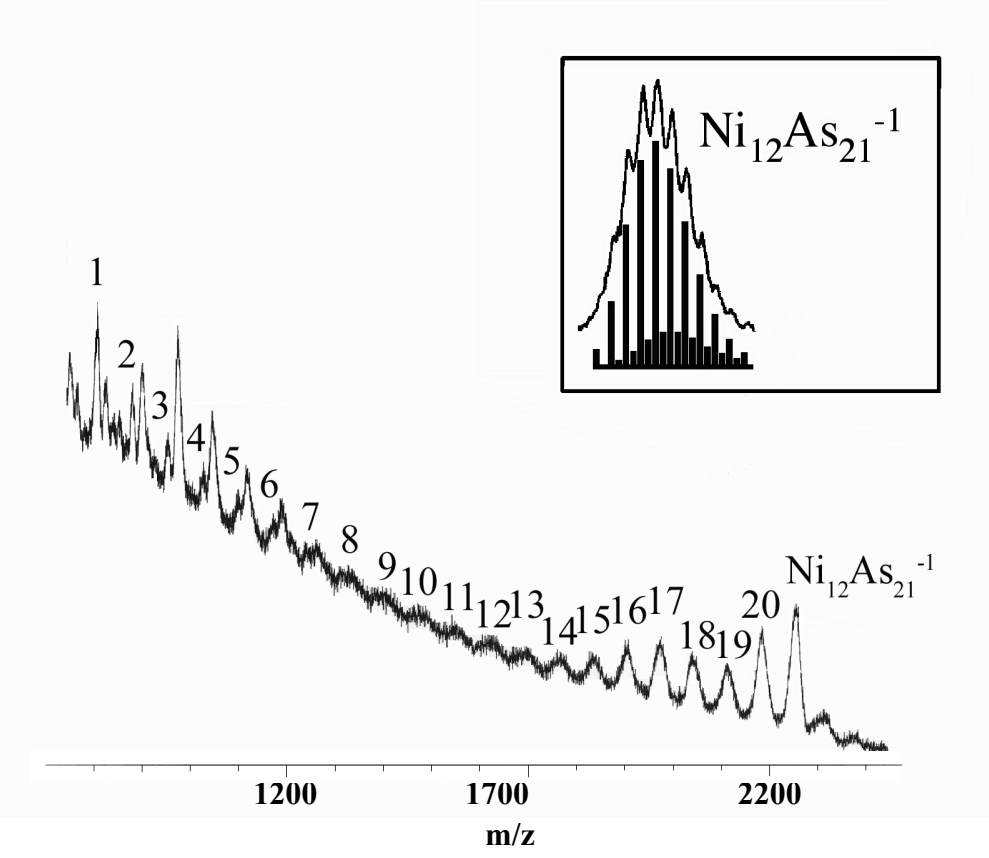

Figure 2. 3. [79] Spectra of $[Bu_4P]_3[As@Ni_{12}@As_{20}]$•1.5en by LDI-TOF-MS. The numbers denote the $[Ni_nAs_{21}]^{1-}$ series. (**Inset**) An enlarged view of the $[Ni_{12}As_{21}]^{1-}$ ion and its corresponding simulated mass envelope.

2.2.4. Extended Hückel Theoretical Calculations

The electronic states of this highly symmetric cluster, $[As@Ni_{12}@As_{20}]^{3-}$, and its subunits, $[As_{20}]$ and $[As@Ni_{12}]^{3-}$, were studied using the semi-quantitative Extended Hückel (EH) method. The results obtained from this theoretical method were used in conjunction with an extensive group theory analysis to construct a qualitative molecular orbital (MO) diagram, see figure 2.4. The order of the molecular orbitals may not be exact due to the low level of accuracy associated with the EH method. The average bond distances indicate that the cluster has virtual I_h point symmetry. Therefore, the average bond distances were used to construct a cluster with perfect I_h on which to run the calculations. The MO diagram was constructed to address three important questions: (1) Is the integrity of the As-As bonds of the As_{20} dodecahedral cage maintained in **2.1** or are the bonds broken in order to interact with the encapsulated $[As@Ni_{12}]^{3-}$ subunit? (2) Do the lone pairs of the $[As_{20}]$ subunit interact with Ni orbitals, from the $[As@Ni_{12}]^{3-}$ unit, of the same symmetry? (3) Is the anionic, endohedral cluster diamagnetic, with a large HOMO-LUMO gap?

The As_{20} dodecahedral cage has 100 valence electrons. The octet rule dictates that a neutral $[As_{20}]$ molecular subunit will have 30 As-As bonds requiring 60 of the 100 valence electrons with the remaining 40 electrons present as As lone pairs. The structure of the dodecahedral cage suggests that each of the 20 lone pairs is located in a local p_z orbital of one of the 20 arsenic atoms and extends radially from the dodecahedral cage. The EH results in conjunction with the group theory analysis reveals that the As-As bonds of the As_{20} dodecahedral cage show negligible

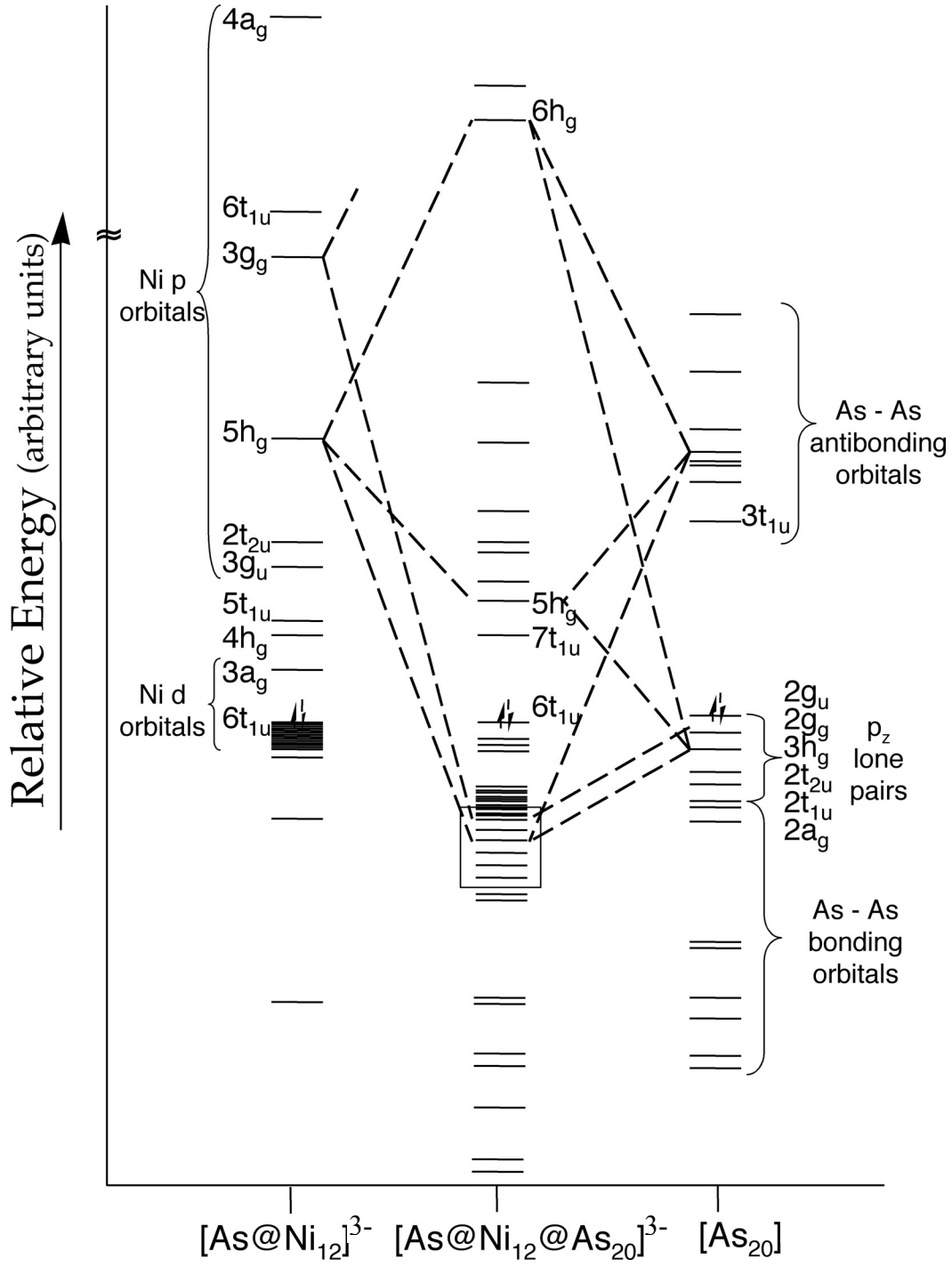

Figure 2. 4. [79] A Qualitative MO diagram of the cluster $[As@Ni_{12}@As_{20}]^{3-}$ (center) from its subunits, $[As@Ni_{12}]^{3-}$ and $[As_{20}]$. All HOMOs are normalized for comparison. Only the h_g and g_g interactions are labeled for clarity. The 20 molecular orbitals inside the box are from the interaction of the $[As_{20}]$ p_z lone pairs and the virtual Ni p orbitals from $[As@Ni_{12}]^{3-}$. Each line represents a an orbital energy level and not the number of degenerate orbitals.

interaction with the $[As@Ni_{12}]^{3-}$ subunit. This observation implies that the arsenic dodecahedral frame work is maintained in the formation of the "onion skin" cluster (figure 2.5 a). Orbital projections indicate that the lone pairs are located in the As p_z orbitals which are normal to the centroids of the Ni_3 faces of the Ni_{12} icosahedra (figure 2.5 b).

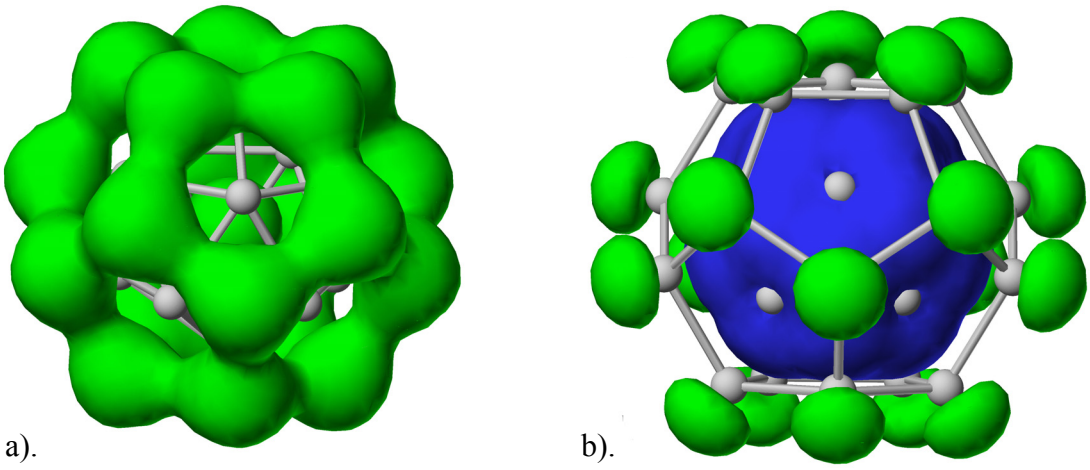

a). b).

Figure 2. 5. [79] a). The 1 a_g MO of the $[As@Ni_{12}@As_{20}]^{3-}$, depicting the As-As interaction of the As_{20} cage. b). The 3 a_g MO of the $[As@Ni_{12}@As_{20}]^{3-}$, depicting the interaction between the As_{20} p_z lone pairs and the Ni p orbitals.

The radial orientation of the p_z orbitals of the As_{20} cage, in which the lone pairs are located, is a favorable position for them to interact with the nickel atoms of the $[As@Ni_{12}]^{3-}$ subunit. Group theory requires that the $[As@Ni_{12}]^{3-}$ subunit have virtual molecular orbitals of the same irreducible representation for interactions with the arsenic lone pairs. In the initial EH analysis of the $[As@Ni_{12}]^{3-}$ subunit, the Ni d orbitals were involved in Ni-Ni bonding of the icosahedral cage and the Ni s orbitals

were primarily involved in Ni-As bonds to the centered arsenic atom. When the complete cluster was analyzed, these interactions remained essentially unaltered. Therefore, the virtual molecular orbitals of the $[As@Ni_{12}]^{3-}$ subunit that had the same irreducible representations, $a_g + t_{1u} + t_{2u} + g_u + h_g$, as the 20 arsenic lone pairs were composed primarily of p-type, Ni-based states mixed with some s-character. The interactions between the virtual Ni p orbitals and the lone pairs from the As_{20} cage create the 20 filled MOs of the $[As@Ni_{12}@As_{20}]^{3-}$ cluster, located inside the box in figure 2.4, which indicate bonding between the polyhedra. An integral overlap representation of the $3a_g$ molecular orbital which depicts the interaction between the As lone pairs and the virtual Ni p orbitals is shown in figure 2.5 b.

The EH MO analysis of the I_h symmetric $[As@Ni_{12}@As_{20}]^{3-}$ anion has 168 cluster valence electrons (CVEs) and gives a diamagnetic system with a sizable HOMO-LUMO gap. 168 CVEs are obtained when Wade-Mingos electron-counting rules[88-90] are used for the $[As@Ni_{12}@As_{20}]^{3-}$ ion. The 168 CVEs originate from the $[As@Ni_{12}]^{3-}$ subunit (128 CVEs) and the $[As_{20}]$ subunit (60 CVEs). Magnetic susceptibility measurements (Evans' method)[91] support the diamagnetism of the cluster.

However, previously reported Wade-Mingos electron counting was done for icosahedral $[Ni_{12}(\mu_{12}\text{-E})]$-type clusters, $[Ni_{12}(\mu_{12}\text{-E})(CO)_{22}]^{2-}$ (E =Ge, Sn) and $[Rh_{12}(\mu_{12}\text{-Sb})(CO)_{27}]^{3-}$, which have 170 CVEs.[92,93] These centered-icosahedral cages have carbonyl ligands surrounding the cage rather than the $[As_{20}]$ cage in $[As@Ni_{12}@As_{20}]^{3-}$. Albano[92] constructed an MO diagram for the $[Ni_{12}(\mu_{12}\text{-As})(CO)_{22}]^{-}$ model anion by the EH method to justify the 170 CVEs. The EH

calculations were only carried out for the $[Ni_{12}(\mu_{12}\text{-As})]^{2-}$ unit but orbitals were filled for all 170 electrons. When MO evaluations are done by this method, the HOMO is has h_g symmetry and all 170 electrons are required for the cluster to be diamagnetic. According to this diagram, the $[As@Ni_{12}@As_{20}]^{3-}$ cluster which has 168 CVEs should be paramagnetic, yet magnetic susceptibility measurements indicate that it is diamagnetic.

The contradiction is likely the result of different chemical environments surrounding the icosahedral cage. The $[As_{20}]$ "ligand" has I_h symmetry while the carbonyl ligands have lower symmetry. The I_h symmetry of $[As_{20}]$ changes the ordering of the virtual orbitals of $[Ni_{12}(\mu_{12}\text{-As})]$ used by Albano *et. a.l*[92] (or filled orbitals in the MO presented here for the complete cluster $[As@Ni_{12}@As_{20}]^{3-}$). Closer examination shows that a g_g set of orbitals in the $[Ni_{12}(\mu_{12}\text{-As})]$ MO diagram are stabilized by metal-"ligand" bonding to the $[As_{20}]$ lone pairs in $[As@Ni_{12}@As_{20}]^{3-}$ MO diagram. Also, a virtual h_g set of orbitals filled in the $[Ni_{12}(\mu_{12}\text{-As})]$ explanation are excluded by symmetry from being filled in the $[As@Ni_{12}@As_{20}]^{3-}$ diagram. In a true I_h symmetric cluster, a filled g_g set of orbitals instead of a h_g set will require two fewer CVEs to be diamagnetic. Scheme 2.1 show this orbital transposition which explains the discrepancies between the MO calculations presented here and the one previously reported.

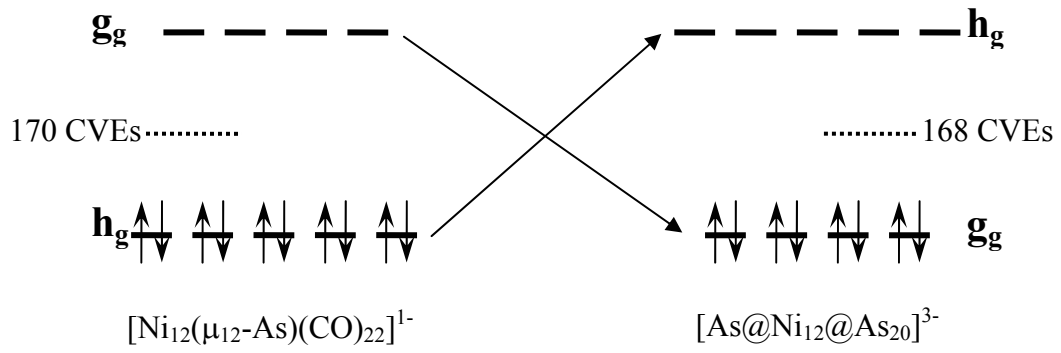

Scheme 2. 1

2.2.5. Molecular Cluster Oxidation

The presence of nickel and arsenic atoms in the $[As@Ni_{12}@As_{20}]^{3-}$ cluster makes them ideal candidates to join a growing class of single-source precursors for binary nanoparticles.[13,14] Unlike most inorganic clusters that can be used as single-source precursors, this cluster is free of organic and organometallic ligands. This ligand-free cluster can be described as a "charged" molecular intermetallic.[94-96] Therefore, an oxidation reaction that will remove this molecular intermetallic's excess electrons should result in the isolation of the binary phase(s) found on the Ni/As phase diagram with atomic ratios that match those in the cluster.[97]

The crystalline $[As@Ni_{12}@As_{20}]^{3-}$ complex was air oxidized and washed to remove ruminates of the cations. An amorphous black powder results from the oxidation step, which was annealed at 500 ºC/2 h. Powder X-ray diffraction (XRD) of the annealed sample shows reflections for the binary phases NiAs and $NiAs_2$ (figure 2.6). The $[As@Ni_{12}@As_{20}]^{3-}$ anion is 63.6% As which corresponds on the Ni/As phase diagram to a mixture of the NiAs and $NiAs_2$ phases in a 1:2 ratio.[97]

Dissolving the cluster complex in dmf with the appropriate amount of $Ni(COD)_2$ followed by air oxidation should in theory shift the stoichiometric oxidation product towards single-phase NiAs binary particles. The shift of the oxidation product towards single-phase NiAs was confirmed by experimental results. However, this process for preparing single-phase binaries was not optimized because a more efficient preparation method was determined and is presented in Chapter 3.

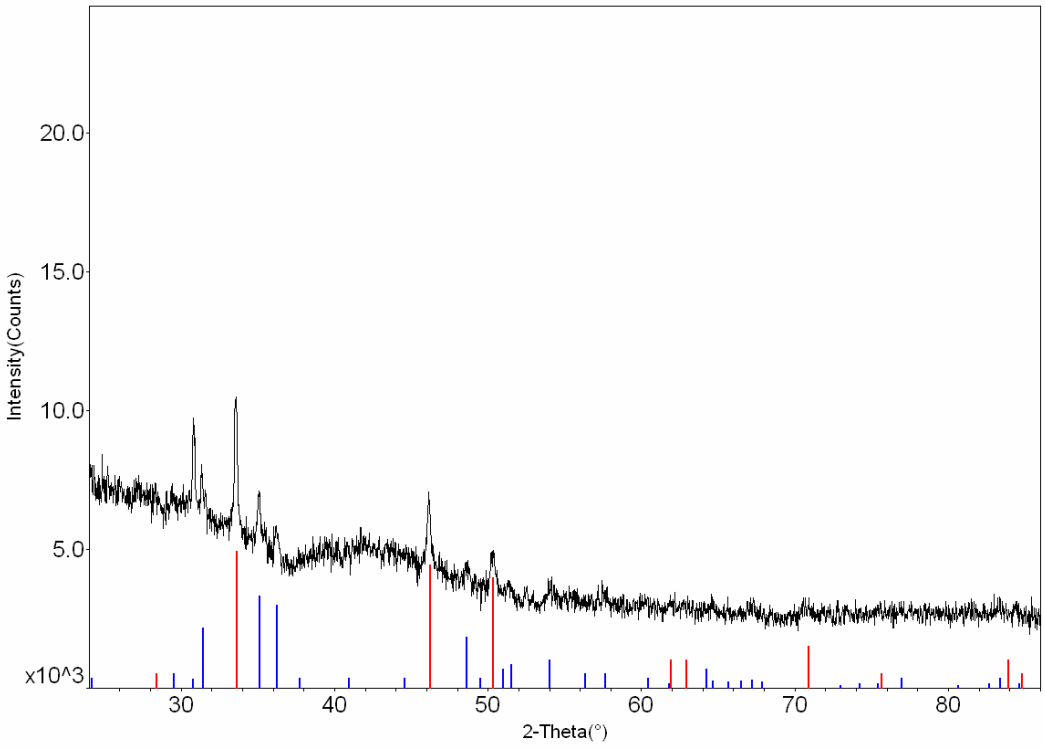

Figure 2. 6. Powder X-ray diffraction pattern of material obtained from air oxidizing the $[As@Ni_{12}@As_{20}]^{3-}$ complex and annealing at 500 ºC/2 h. NiAs (JCPDS # 11-0014)[98] is indicated by red lines, and $NiAs_2$ (JCPDS # 31-0900)[99] is indicated by the blue lines.

2.3. Discussions

The intriguing cluster described here, $[As@Ni_{12}@As_{20}]^{3-}$, resembles a variety of cluster types similar to the carbon fullerenes. It also joins the continually growing

class of ligand-free binary cluster sometimes referred to as "charged" molecular alloys/intermetallics.[94,95,100] Like most members of this growing class of clusters, the $[As@Ni_{12}@As_{20}]^{3-}$ ion can be considered a transition-metal / Zintl ion complex. The As_{20} dodecahedral cage is a new Zintl anion that is isoelectronic with the known $C_{20}H_{20}$ fullerene cluster (As ≈ CH).[101]

The rare I_h symmetry of this complex 33 atom cluster prompted a surge of theoretical studies.[80,102,103] While DFT calculations done by Baruah *et. al.*[80] on the $[As@Ni_{12}@As_{20}]^{3-}$ cluster where performed using T_h symmetry, they found that the optimized geometry is I_h in accordance with the experimental results. These DFT results were done for both charged and neutral clusters and support the diamagnetic nature of the 3- cluster presented earlier. The triply charged cluster gives a large HOMO-LUMO gap by DFT. DFT studies on the singly charged ion observed by LDI-TOF-MS, $[As@Ni_{12}@As_{20}]^{1-}$, also have a high degree of stability. They report that the extra electrons in a $[As@Ni_{12}@As_{20}]^{3-}$ cluster would be energetically unfavorable in the gas phase as result of electrostatic repulsion.

IR and Raman analysis calculated in the DFT study for the neutral cluster indicate interactions between the $[As_{20}]$ and $[As@Ni_{12}]$ cages.[80] However, in contradiction to the EH results, the DFT study suggests that the As-As bonds of $[As_{20}]$ undergo rehybridization in the presence of the $[As@Ni_{12}]$ cage forming strong Ni-As bonds. It is the strong Ni-As interaction that they credit for maintaining the $[Ni_{12}As_{21}]^{1-}$ cluster present in the gas phase.

The $[As@Ni_{12}@As_{20}]^{3-}$ ion has a truly unique structure but the carbon-free binary nature of this novel cluster gives rise to its potential industrial importance.

2.4. Experimental Section

2.4.1. General Data

All reactions were performed in a nitrogen atmosphere dry box (Vacuum Atmospheres Company). Matrix free MALDI-TOF-MS studies were performed on a Bruker Proflex with a 0.1nm spectral bandwidth with a purged glove bag over the sample chamber. The system uses a N_2 plasma laser at 337.1 nm and a 3 ns pulse width. An AMRAY 1820K scanning electron microscope with a potential of 20 kV was used for energy dispersive X-ray (EDX) analysis. Extended Hückel calculations and visualizations were performed using a CACHE® software package. A Bruker D8 Advance θ-θ X-ray Powder Diffractometer (CuK_α radiation, Kevex detector) was used to obtain XRD patterns for phase identification. A step width of 0.02º between of $5º \leq 2\theta \geq 90º$ was used. Analysis of the XRD patterns was done using the JADE® software package equipped with the JC-PDF database and auto indexing. A Hitachi S4700-FE was used to obtain the SEM images.

2.4.2. Chemicals

Melts of nominal composition of K_3E_7 (E = As) were prepared by fusion (at ~1100 ºC) of stoichiometric ratios of the elements. The elements were weighed out in a nitrogen atmosphere drybox then sealed in evacuated, quartz tubes before firing. *Bis*-cyclooctadiene Nickel(0), $Ni(COD)_2$, was purchased from STREM Chemicals. Tetrabutlyphosphonium bromide, Bu_4PBr, was purchased from Aldrich. Elemental

iodine, I_2, was purchase from CERAC. All chemical precursors from manufactures were used without further purifications. Anhydrous ethylenediamine (en) and dimethylformamide (dmf) were purchased from Fischer, vacuum distilled from K_4Sn_9 and stored under dinitrogen. Toluene was distilled from sodium under dinitrogen and stored under dinitrogen.

2.4.3. Synthesis

2.4.3.1 Preparation of [Bu4P]3[As@Ni$_{12}$@As$_{20}$]·1.5en

In vial 1, K_3As_7 (50.0 mg, 0.0779 mmol) and Bu_4PBr (79.0 mg, 0.233 mmol) were dissolved in en (~1.5mL) and stirred for 5 min., yielding a dark red solution. In vial 2, en (~0.5mL) was added to $Ni(COD)_2$ (43.0 mg, 0.156 mmol). The slurry from vial 2 was added to vial 1 and the solution was stirred for 4h. The solution changed form a reddish brown to a dark brown solution and was then filtered through tightly packed glass wool. The filtered solution is heated (~50°C) for 5 mins and filtered again through a hot filter. In 1 hour, tiny black crystals of $[Bu_4P]_3$**2.1**•1.5en begin to precipitate. Crystals continue to form over 1-3 days. Yield 15 mg (37%). EDX As:Ni:P = 20.88:12.00:3.12; MS (MALDI-TOF) m/z = 2278 $[Ni_{12}As_{21}]^-$.

2.4.4. Crystallographic Studies

Dr. James Fettinger performed all single crystal X-ray analysis. The results of the refinement mentioned here are summarized in table 2.1.

Chapter 3

Ni/As Binary Phase Nanoparticles from Zintl Anions

3.1 Introduction

New materials are constantly in demand by the optical, electrical and catalytic industries. These materials are often binary phases composed of transition-metals and main group elements.[104-106] The technological drive toward miniaturization demands synthetic methods that produce nanometer range particles of these compounds. Therefore, it is not surprising that this is an area of growing interest.[107-110]

Monoarsenides, such as GaAs and InAs, are well known semiconductors.[111,112] Transition-metal monoarsenides like FeAs are also used as semiconductor as well as being employed as secondary high-temperature batteries and as catalysts.[113,114] Other transition-metal monoarsenides are also likely to have important properties that can be used for technological applications of this nature. The technological drive to smaller and smaller devices makes nanometer size particles of these materials desirable. Therefore, it is not surprising that new preparations methods of nickel, iron, and cobalt monoarsenides that produce nanocrystalline material are being investigated.[7,69]

The well known method for isolating binary phases is the stoichiometric combinations of the desired elements at high temperatures often approaching

1000 ºC. Phases formed from high temperature reactions agglomerate forming bulk materials rather than nanoparticles due to sintering. Therefore, to produce binary phase nanoparticles reaction methods must be preformed at lower temperatures or include the use of passivating materials or solvents to control particle agglomeration. One new low temperature method for preparing single-phase monoarsenides is by ultrasonically mixing a metal chloride, arsenic metal and potassium borohydride and subsequently heating the mixture at low temperatures (100 ºC).[69] High-intensity ultrasonic irradiation of a mixture of a metal chloride, arsenic metal and zinc metal at room temperature produces the metal monoarsenides at room temperature.[7] Both methods generate nanocrystalline materials (FeAs, CoAs, NiAs); 20-35 nm for the former and 12-20 nm for the later.

While these syntheses produce binary nanoparticles, only the most thermodynamically stable phases of those in the phase diagrams are isolated. Many transition-metal/arsenide phases are not accessible by these methods[7], such as Ni_5As_2, $Ni_{11}As_8$ and $NiAs_2$. These previously unaccessed phases may provide a rich banquet of new electrical, catalytic and optical nanomaterials making a generic synthetic route to all the possible phases essential to these technologically advancing industries.

Most of the nickel arsenide phases form naturally as minerals. $NiAs_2$, NiAs, and $Ni_{11}As_8$ are known to mineralogists as rammelsbergite, niccolite and maucherite. NiAs is a well known structure type where the nickel atoms are octahedrally coordinated to the arsenic atoms, and the arsenic atoms are coordinated in a trigonal prismatic arrangement to the nickel atoms. [115,116] $NiAs_2$ has a pyrite-like structure in which the nickel is in an octahedral coordination with arsenic. [117,118] Nickel arsenic

octahedra share a single edge with adjacent octahedra differing only slightly from pyrite which has no octahedral edge sharing. The $NiAs_2$ and NiAs structures differ only in that every arsenic position in NiAs is replaced by As_2 dimers in $NiAs_2$.

The nickel-rich binary phases, $Ni_{11}As_8$ and Ni_5As_2, have more complex lattice structures. [119,120] Both structures have Ni-Ni separation within typical Ni-Ni bond distances unlike the more arsenic-rich phases. The complexity of the $Ni_{11}As_8$ and Ni_5As_2 structures arise from both having multiple nickel and arsenic coordination environments. $Ni_{11}As_8$ has six non-equivalent nickel atoms, five in a square pyramidal coordination to arsenic and the other in a stretched octahedral coordination.

This chapter presents a generic synthetic route to phase-specific Ni/As binary phases by employing Zintl ions as the main group source. All four of the binary phases on the Ni/As binary phase diagram, Ni_5As_2, $Ni_{11}As_8$, NiAs and $NiAs_2$, can be individually synthesized by this near-room temperature method as nanoparticles for the first time. No other synthetic approach allows access to an entire transition-metal / pnictide phase diagram. This method may prove to be equally useful for a variety of other transition-metal / pnictide phase diagrams (i.e. Pd/As, Ni/P) providing nanoparticle synthesis of materials not previously know in this size range.

3.2 Results

3.2.1. Synthesis

Every phase on the Ni/As phase diagram[62] (Ni_5As_2, $Ni_{11}As_8$, NiAs and $NiAs_2$) can be selectively isolated in high yields from a generic procedure with only slight

modifications, eq. 5.1. Ethylenediamine (en) solutions of K_3As_7 and toluene (tol) solution of $Ni(COD)_2$ are heated and then mixed. After mixing, the solution is exposed to mild heating for a short time and a black material precipitates from the mixed solution. The as-prepared black precipitate is removed from solution and washed with acetonitrile and 0.01M HCl resulting in an amorphous material. The crystallinity of the as-prepared sample was improved by mild annealing.

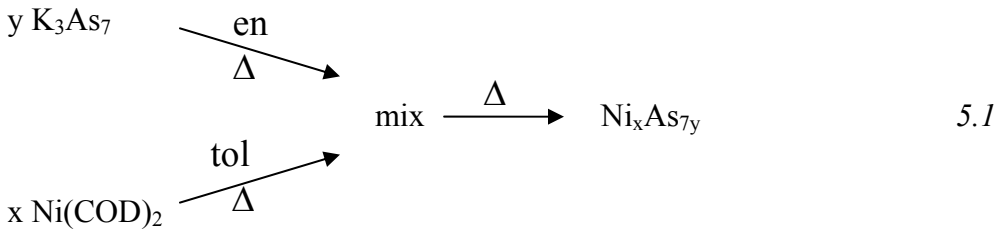

5.1

The synthesis of the two nickel-rich phases, $Ni_{11}As_8$ and Ni_5As_2, required addition of polyvinlylpirolydine (PVP) to the en solution of K_3As_7 before heating. PVP was not used in the preparation of the remaining phases, NiAs and $NiAs_2$. However, a dimethylformamide (dmf) solution of I_2 is required to precipitate the desired As-rich binaries, NiAs and $NiAs_2$, out of solution. The as-prepared amorphous samples were characterized by X-ray photoelectron spectroscopy (XPS) and their particles sizes were imaged by transmission electron microscopy (TEM). The identity of the annealed samples was confirmed by powder X-ray diffraction (XRD) and characterized by XPS for comparison to the as-prepared samples.

3.2.2. Powder X-ray Diffraction

The diffraction patterns of samples with appropriate crystallinity can be obtained by XRD. The diffraction patterns can be compared to diffraction patterns of known materials that have been compiled by the international centre of diffraction data (ICDD). JADE©, an XRD pattern processing and identification program, is used to index peaks on diffraction profile to specific cell parameters allowing them to be compared to those listed by the ICDD.

All four as-prepared samples were amorphous resulting in no X-ray diffraction patterns. Annealing at 400 ºC for 5 hours was used to obtain sufficient crystallinity in all four samples to obtain X-ray diffraction patterns. The XRD patterns of all four annealed samples (Figure 3.1 a-d) are consistent with literature patterns. Cell refinements of each of the annealed diffraction patterns indexed all peaks to the cells previously reported for the respective phases, see table 3.1, indicating only a single crystalline phase after annealing in each diffraction profile except the $NiAs_2$ pattern which shows a small trace of a NiAs impurity.

The $NiAs_2$ diffraction pattern is consistent with literature reports (JCPDS #11-0014). [98] The cell parameters of the $NiAs_2$ pattern calculated by a cell refinement of the diffraction profile are in good agreement with those reported for the $NiAs_2$ mineral, rammelsbergite (JCPDS # 11-0014), see table 3.1. [99]

The diffraction pattern obtained by XRD (figure 3.1b), and the cell parameters calculated from the profile of the annealed NiAs sample (table 3.1) are also in good agreement with literature values (JCPDS #31-0900) [99]. Annealing of this compound

at 200 ºC/2 h or 400 ºC/5 h results in the same NiAs XRD pattern with no other phases

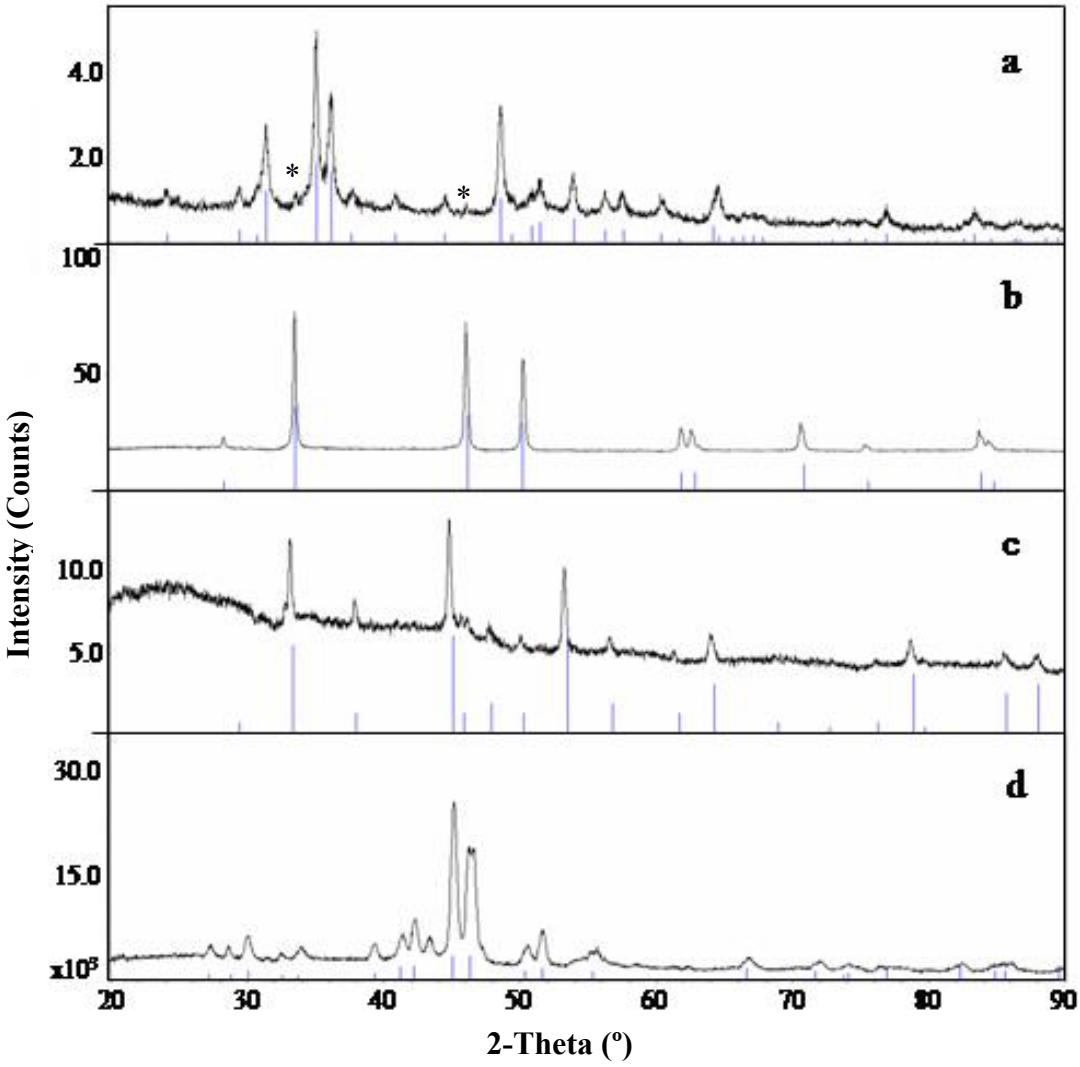

Figure 3. 1. XRD patterns of $NiAs_2$ (a), NiAs (b), $Ni_{11}As_8$ (c), and Ni_5As_2 samples after annealing at 400 ºC/ 5 h. Matching JCPDS line diagrams are also shown (#11-0014, #31-0900, #08-0085 and #10-260, for a-d respectively) [98 99,121,122]. The asterisks indicate a NiAs impurity.

observable (figure 3.2 a-b). However, annealing at the higher temperature produces a more crystalline diffraction pattern distinguishable by sharper and more intense diffraction peaks.

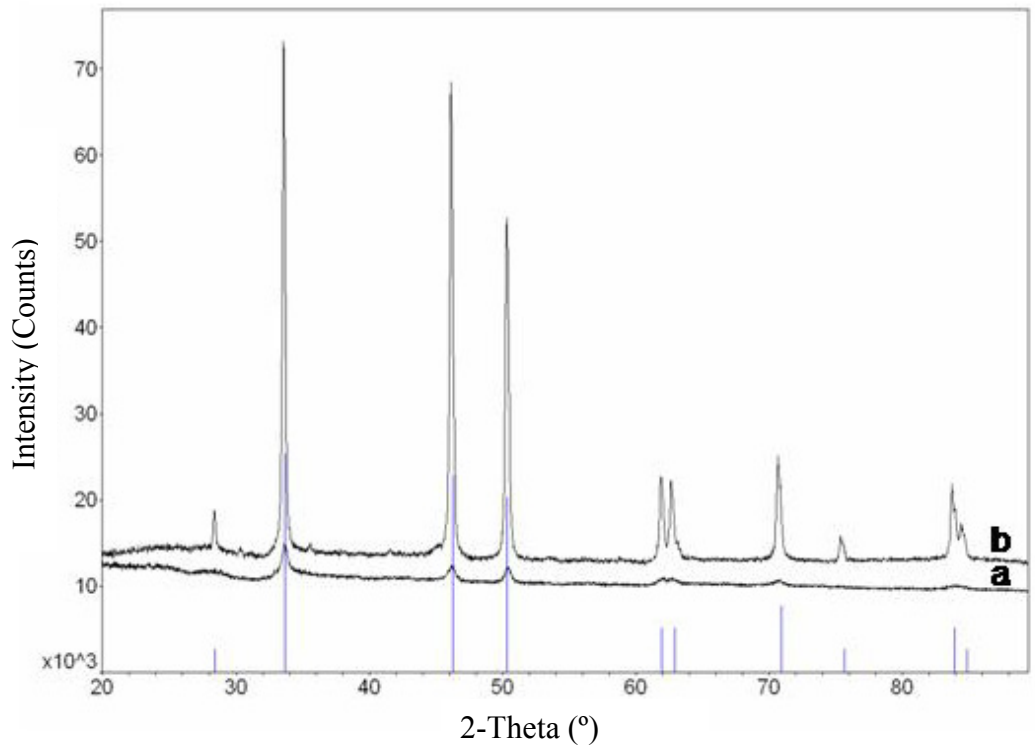

Figure 3. 2. NiAs XRD patterns after the sample had been annealed at 200 ºC/2h (a) and 400 ºC/5h (b) (JCPDS #31-0900). [99] Diffractometer settings were the same for both patterns.

The annealed $Ni_{11}As_8$ sample produces a diffraction pattern that matches reported diffraction patterns of both a high temperature synthesized $Ni_{11}As_8$ sample (JCPDS #18-0875) [123] and the mineral maucherite, $Ni_{11}As_8$, (JCPDS #08-0085: figure 3.1c) [121]. Cell parameters reported for both the synthesized and the mineral, $Ni_{11}As_8$ samples are virtually identical. A cell refinement of all of the diffraction peaks of the annealed $Ni_{11}As_8$ sample discussed here could be indexed to the same cell. The cell parameters reported for the mineral, maucherite, and the annealed $Ni_{11}As_8$ sample are presented in table 3.1 for comparison.

Table 3. 1. Refined cell parameters for all four binary phases.

Binary Cell Parameters	a (Å)	b (Å)	c (Å)
$NiAs_2$ JCPDS #11-0014[98]	4.759	5.797	3.539
$NiAs_2$ Refined Cell	4.75468	5.799	3.54379
NiAs JCPDS #31-0900[99]	3.622	**a**	5.013
NiAs Refined Cell	3.62224	**a**	5.04031
$Ni_{11}As_8$ JCPDS #08-0085[121]	6.85	**a**	21.75
$Ni_{11}As_8$ Refined Cell	6.87124	**a**	21.80598
Ni_5As_2 JCPDS #10-0271[122]	6.7	**a**	12.41
Ni_5As_2 Refined Cell	6.75476	**a**	12.45911

Like the previous as-prepared binary samples, Ni_5As_2, had to be annealed to attain sufficient crystallinity to obtain an XRD pattern. The pattern matches two reported diffraction patterns (JCPDS #10-0271 and #10-0260)[122] which have virtually identical cell parameters. Cell parameters of the annealed Ni_5As_2 sample discussed here obtained from cell refinement calculations are similar to those of both reported patterns. The cell parameters of one of the reported patterns and the annealed Ni_5As_2 sample are presented in table 3.1 for comparison.

3.2.3. X-ray Photoelectron Spectroscopy

The poor crystallinity of the as-prepared samples of Ni_5As_2, $Ni_{11}As_8$, NiAs and $NiAs_2$ prevents identification of their phases by XRD. Atomic binding energies determined by XPS are affected by their oxidation state and the presence of neighboring atoms of the same or different elements. XPS studies performed on both the as-prepared samples and the corresponding annealed samples, whose XRD patterns were used to identify their phases, can be compared. While the phase(s) present in each as-prepared sample can not be confirmed by comparing the XPS data, the presence of metallic Ni and As, which would be present if multiple phases were present in the as-prepared amorphous samples or if a phase transition occurred during annealing, can be determined. Little is known about the binding energies of the Ni_5As_2, $Ni_{11}As_8$ and $NiAs_2$ phase, but a detailed study of the mineral niccolite, NiAs, by Nesbitt and Reinke[116], determining the binding energies of the Ni $2p_{3/2}$ and As $3d_{5/2}$ lines (853.0 and 41.1, respectively) has been reported. Nesbitt and Reinke's[116] study also reported that air and water exposure to the mineral produced both arsenic and nickel oxides. The binding energies reported in this study will be used as a guide for fitting spectra of the as-prepared and annealed compounds (see table 3.2).

Depth profiling on all as-prepared and annealed samples was carried out by argon ion milling to remove the surface oxides and show that the Ni/As phase was present through out the particles not just at the surface. The binding energies of elements present at the surface of every sample were recorded. Then the samples were ion milled for 5 minutes and new data were recorded. This depth profiling was carried out multiply times for each sample. Both the annealed and the as-prepared

amorphous samples show strong surface oxide species on the surface of the samples for the Ni $2p_{3/2}$ and As $3d_{5/2}$ binding energy regions. As the sample surfaces were etched away with each ion milling, a decrease in the oxides species was observed in the O 1s, Ni 2p and As 3d binding energy regions while the bulk binary peaks became more intense in both the Ni 2p and As 3d regions. Average binding energies for the bulk binaries in both the annealed and as-prepared amorphous samples are reported in table 3.2.

3.2.3.1. Arsenic Binding Energies

Every As 3d XPS spectral contribution is composed of two peaks known as a spin orbit split doublet, As $3d_{5/2}$ and As $3d_{3/2}$, which represent the different possible angular momentums of electrons ejected from the As 3d orbital. The As $3d_{5/2}$ peak assignments were evaluated and parameters manually set for the best fit. According to theory the As $3d_{3/2}$ peaks were restrained to 0.69 eV higher binding energy than their corresponding As $3d_{5/2}$ peak and at two-thirds of its intensity. The same full width half maximum (FWHM) set for a As $3d_{5/2}$ peak was also used for the corresponding As $3d_{2/3}$ peak. As 3d binding energies discussed here refer only to the As $3d_{5/2}$ binding energies and will be used for component assignment throughout this document.

As 3d XPS spectral contributions to the binding energy data obtained for the annealed NiAs nanoparticles after multiple etchings are largely fit by a single peak in the 41.2 eV region, see figure 3.3 b. This binding energy is close to that of the As 3d peak seen for the NiAs mineral, niccolite, 41.1 eV. The remaining contributions

reside on the high binding side of the main peak and represent surface oxide species similar to those seen by Nesbitt et. al. on the air and water exposed mineral.

Table 3. 2. XPS binding energy averages[a] (eV).

Ni/As Phase	*Ni $2p_{3/2}$ Annealed*	*Ni $2p_{3/2}$ Amorphous*	*As $3d_{5/2}$ Annealed*	*As $3d_{5/2}$ Amorphous*
$NiAs_2$	853.05 ± 0.04	853.06 ± 0.06	41.30 ± 0.07	41.34 ± 0.03
NiAs	853.09 ± 0.04	852.96 ± 0.04	41.23 ± 0.11	41.25 ± 0.08
$Ni_{11}As_8$	852.86 ± 0.04	852.76 ± 0.04	41.31 ± 0.07	41.4 ± 0.01
Ni_5As_2	852.81 ± 0.04	852.90 ± 0.03	41.51 ± 0.04	41.52 ± 0.01
Ni^0	852.6 [124]			
As^0			41.8[125]	
NiAs[116]	853.0		41.1	

a. Photopeaks near the respective binding energy regions for every etching were averaged to obtain these values and standard deviations.

Assignment of the low binding energy peak to arsenic of bulk NiAs is further supported by the depth profiling results. After etching of the annealed NiAs sample, the sample shows an increase in the ratio of the low binding energy region, 41.2 eV, to the high binding energy contributions, surface oxides. Since the higher binding energy peaks make up less of the surface concentration as the sample is etched away, they can be classified as surface species that resulted from their exposure to air and water.

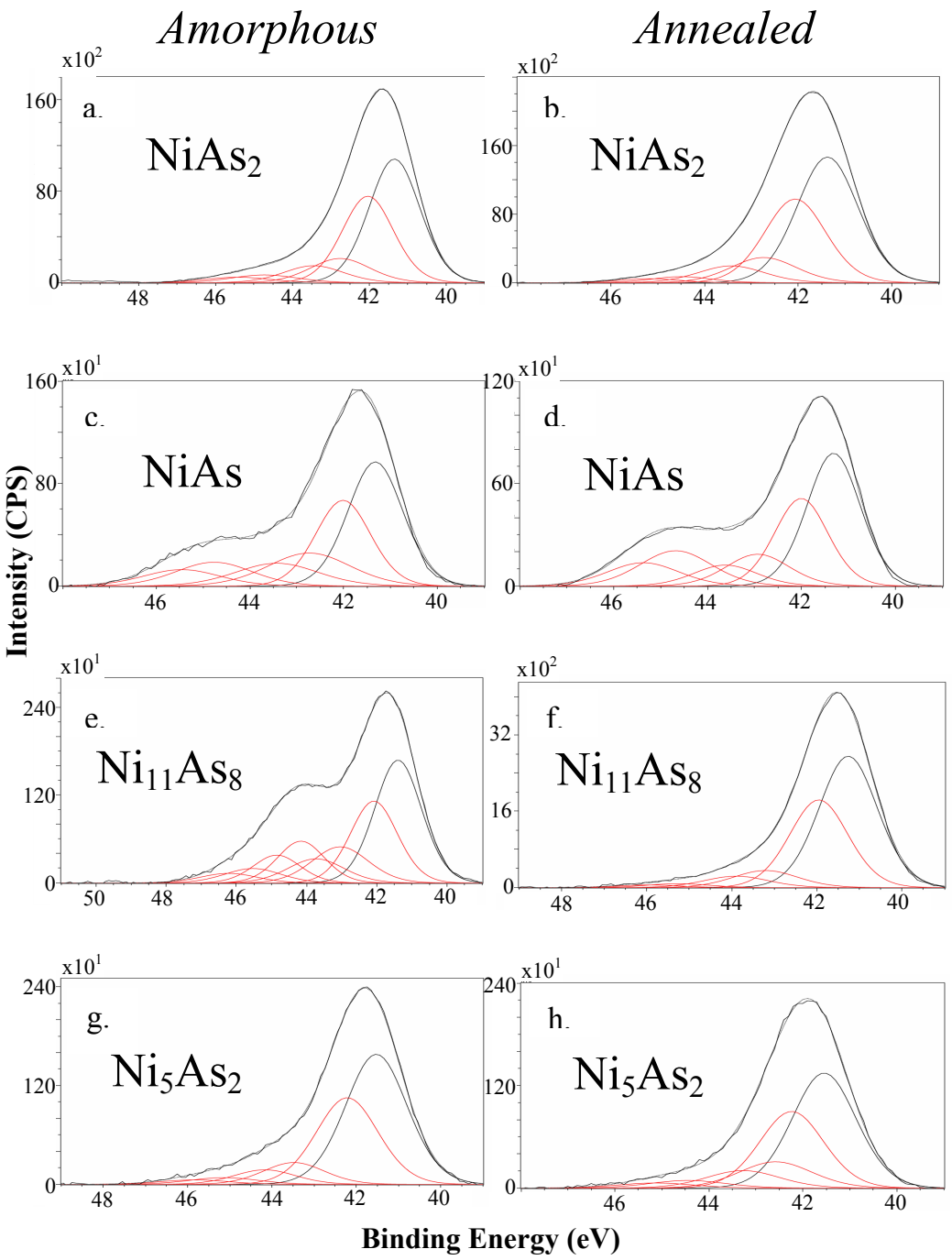

Figure 3. 3. The XPS spectra of the As 3d binding energy regions from the amorphous and annealed $NiAs_2$, NiAs, $Ni_{11}As_8$ and Ni_5As_2 sample. The peaks under the spectra represent the spectral components. The black As $3d_{5/2}$ component peak is from the bulk Ni/As phase component.

The higher binding energy surface oxide spectral contributions are never fully removed. This feature can be attributed to the nanoparticle size of the NiAs sample, see figure 3.4. The sample area detected by XPS encompasses multiple nanoparticles, and each nanoparticle is potentially coated with surface oxides. Therefore, when atomic layers are removed by argon ion milling in the depth profiling studies, not all of the surface oxides on the nanoparticle at the surface will be removed, see figure 3.3b.

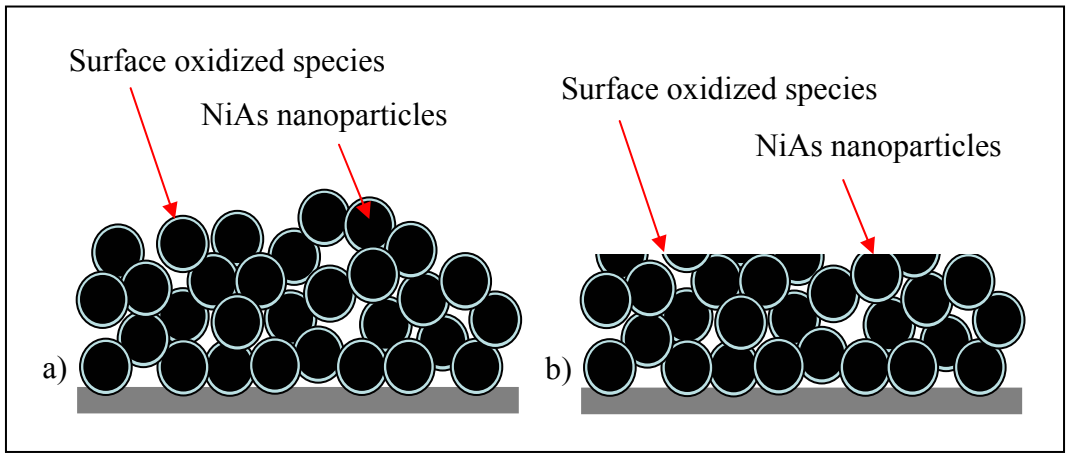

Figure 3. 4. a). Illustration of a group of nanoparticles (black spheres) coated with oxides (lighter rings around black spheres). b). Illustration of the same group of nanoparticles after ion milling in which the decrease in oxide coating at the surface is apparent.

Assignment of the spectral contributions to the As 3d binding energy region obtained for the annealed $NiAs_2$ sample are similar to those of the NiAs sample (figure 3.3 d). As was observed in both the as-prepared and annealed NiAs sample, surface oxide species make-up the majority of the spectral contributions before etching of the surface occurs for both the as-prepared and annealed $NiAs_2$. The

quantity of high binding energy (oxide species) compared to the low binding energy (unoxidized $NiAs_2$) contributions seen in the arsenic binding energies spectra of both $NiAs_2$ samples before any of the surfaces are etched away (figure 3.5, red lines) indicate high oxide coverage. Depth profiling studies (figure 3.5, black lines) show that the ratio of the low binding energy peak intensity of $NiAs_2$ to the high binding energy intensity of the oxide species increase as the surface is milled (etched) away indicating that the oxide species are surface species and not present as bulk components of the nanoparticles.

The As 3d XPS data for the more Ni-rich as-prepare and annealed samples, $Ni_{11}As_8$ and Ni_5As_2, also show peaks for the respective bulk phase which become more prominent as the surface is etched away (figure 3.4 f and g). The depth profiling studies also show the reduction of the oxides species on high binding energy sides of the bulk peaks as the surface of the sample is removed by ion milling. The binding energies of the bulk species of the annealed samples, $Ni_{11}As_8$ 41.31 ± 0.07 eV and Ni_5As_2 41.52 ± 0.04 eV, are at slightly higher binding energies than bulk NiAs, 41.23 ± 0.11 eV.

3.2.3.2. Nickel Binding Energies

The nickel contributions to the XPS spectra are composed of two spin-orbit split peaks, Ni $2p_{3/2}$ and Ni $2p_{1/2}$, but the energy difference between the peaks are not enforced by theory as is the case with As 3d photopeaks. Each Ni 2p photopeak has an associated satellite peak located at 6 to 8 eV higher binding energy and are believed to result from less probable transitions or transitions that occur in a multiply

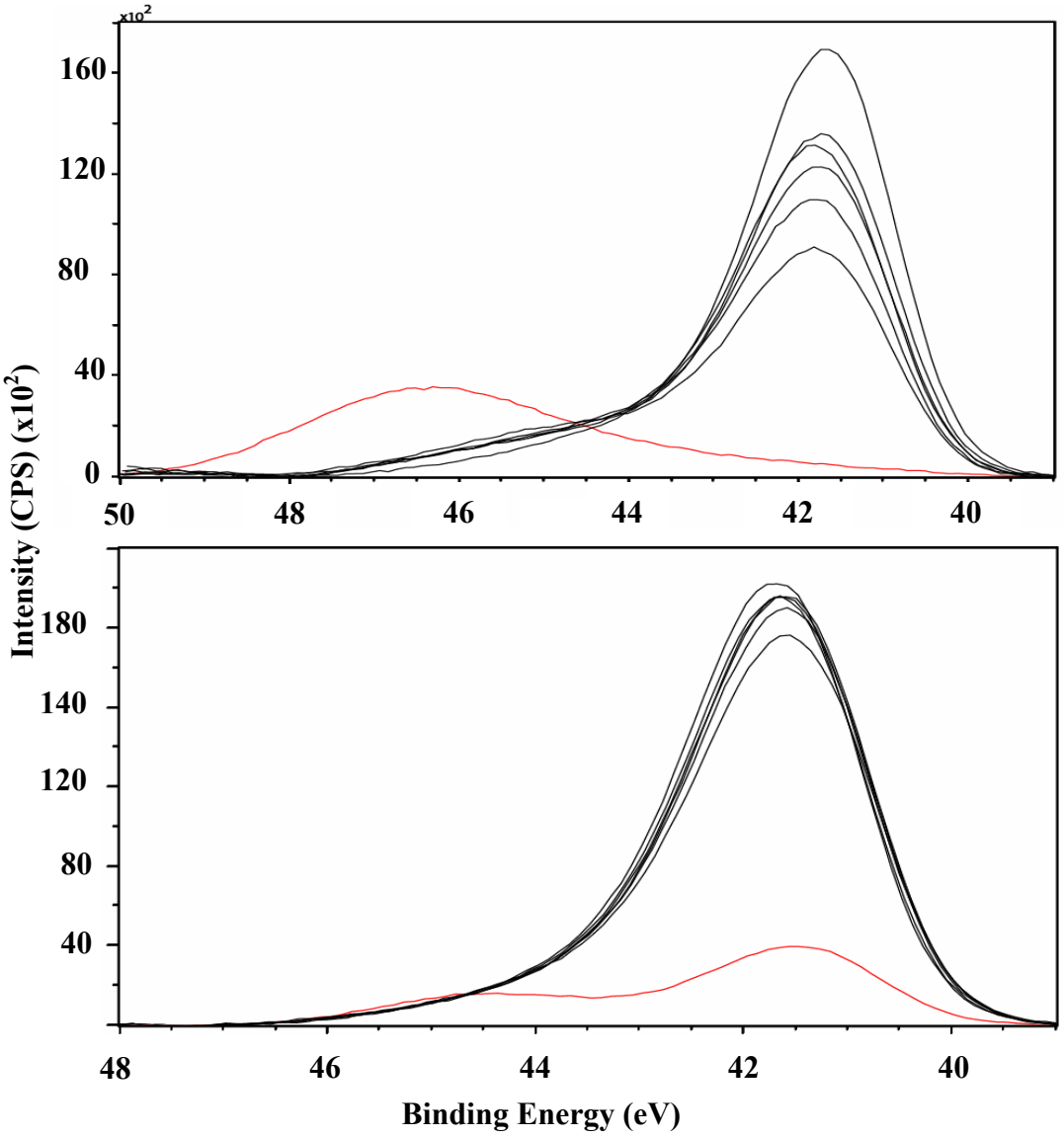

Figure 3. 5. Successive XPS spectra (black) recorded for $NiAs_2$ in the As 3d binding energy region (top is amorphous sample and bottom is annealed sample) after the surface of the sample was etched away. The red spectra are of XPS studies on the samples before any etching was performed.

ionized atom. The satellite peaks are consistently reported to have FWHMs larger than their matching photopeaks and much smaller intensities, but no restraints are

placed on either property. Throughout this document only the main Ni $2p_{3/2}$ photopeaks will be discussed.

The Ni 2p spectral contributions of all four annealed phase-specific samples (NiAs, $NiAs_2$, $Ni_{11}As_8$ and Ni_5As_2) show features and trends that are reminiscent of the As 3d data just described. The low binding energy peak represents nickel in the bulk Ni/As phases. Higher binding energy Ni $2p_{3/2}$ spectral contributions are from surface oxides species (figure 3.7b, d, f, and g). This assignment is supported by the increase in the bulk phases binding energy intensity ratio to the higher binding energy Ni $2p_{3/2}$ oxide contributions as the surface of the samples are successively etched (figure 3.8). The Ni $2p_{3/2}$ binding energy for both annealed NiAs and $NiAs_2$ are approximately 853.0 eV, which matches the binding energies reported for nickel in bulk niccolite, NiAs. The Ni $2p_{3/2}$ binding energies in the Ni-rich phases, $Ni_{11}As_8$ and Ni_5As_2, are lower at around 852.8 eV.

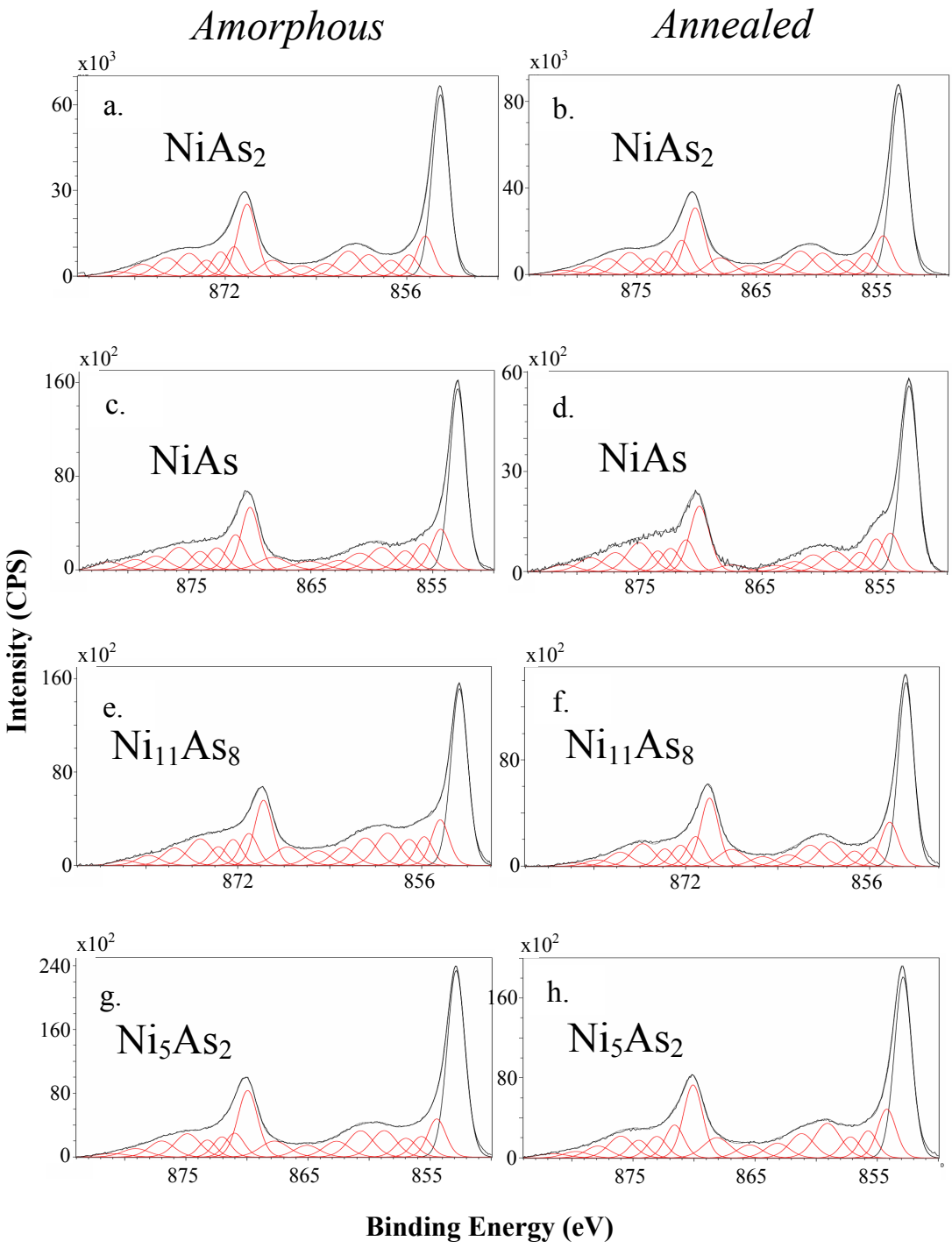

Figure 3. 6. The XPS spectra of the Ni 2p binding energy regions from the amorphous and annealed $NiAs_2$, NiAs, $Ni_{11}As_8$ and Ni_5As_2 sample. The peaks under the spectra represent the spectral components. The black Ni $2p_{3/2}$ component peak is from the bulk Ni/As phase component.

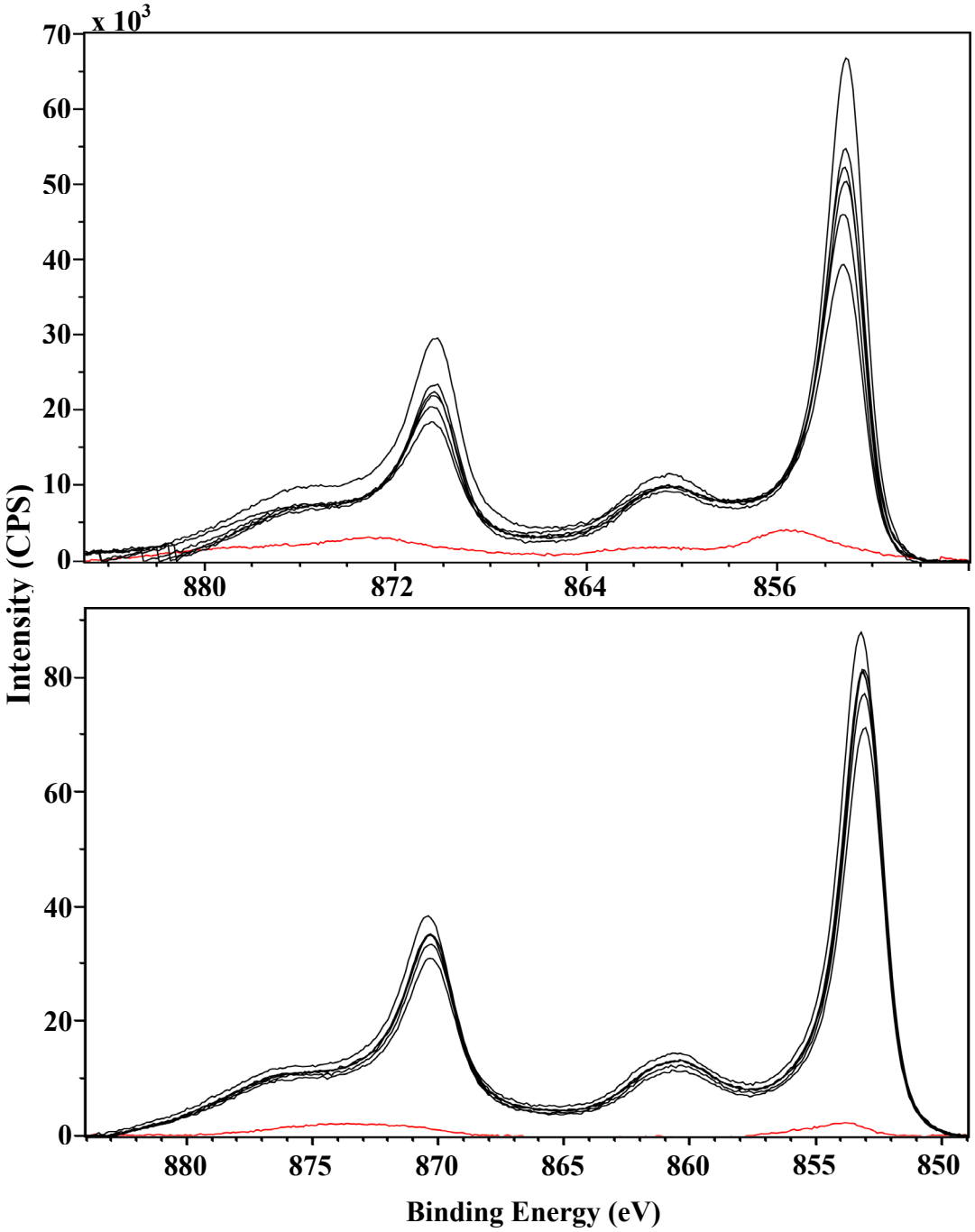

Figure 3. 7 Successive XPS spectra (black) recorded for $NiAs_2$ in the Ni 2p binding energy region (top is amorphous sample and bottom is annealed sample) after the surface of the sample was etched away. The red spectra are of XPS studies on the samples before any etching was performed.

3.2.4. Transmission Electron Microscopy

The TEM image of $NiAs_2$, seen in figure 3.8, is comprised of particles of 3 ± 1 nm average particle sizes over a small distribution range. Exact morphologies of particles in this size range are hard to determine.

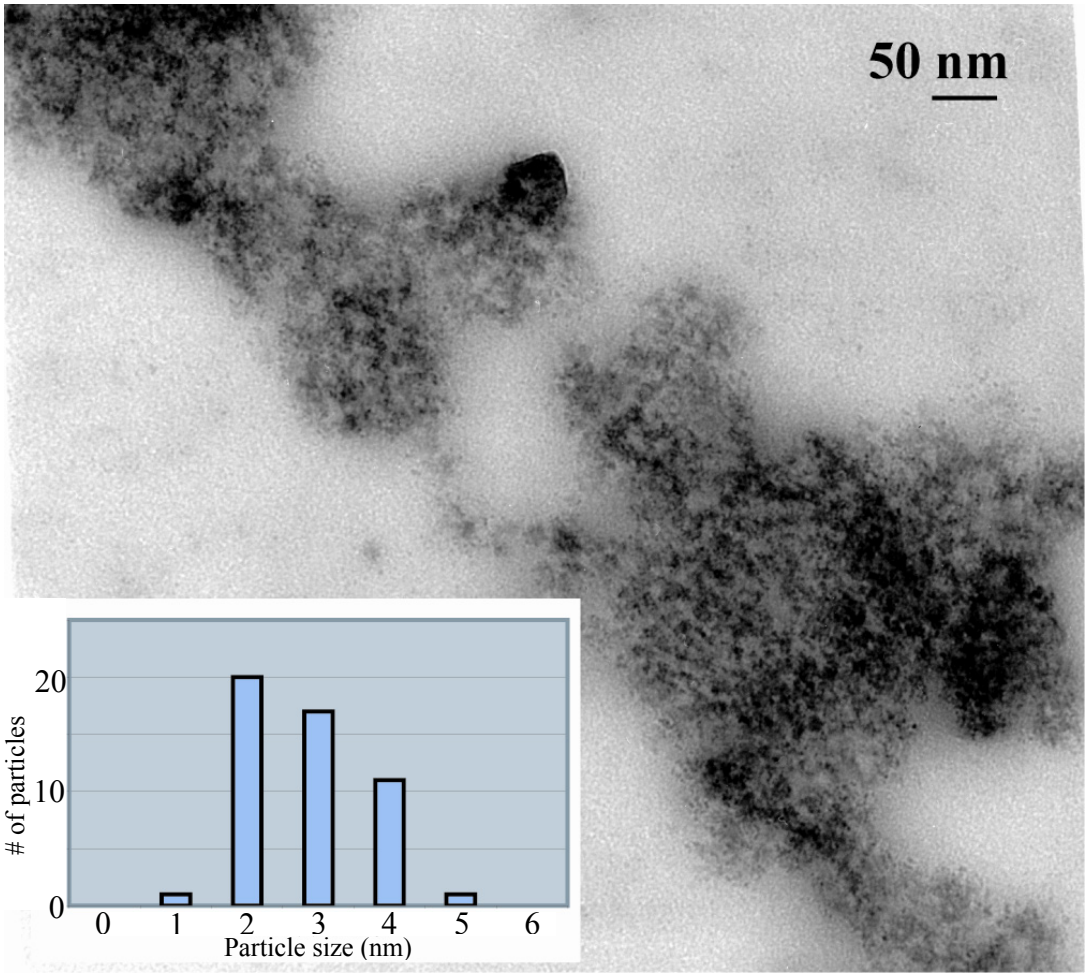

Figure 3. 8. TEM image of $NiAs_2$ sample dispersed with dmf on a copper grid. Inset shows the nanoparticles distribution range.

Nanoparticles of the NiAs phase were also imaged by TEM. The TEM image in figure 3.9 shows many spherical groupings of smaller particles. The resolution

quality of the image makes it difficult to determine the edge of particles that overlap. The distribution of 50 particles with distinct edges is presented in the inset of figure 3.9. The small distribution range gives an average particle size of 7 nm ± 1 nm. The 7 nm particles typically form 49 nm ±9 nm agglomerations. The difficulty in dispersing this phase is exemplified by the large grouping seen near the center of figure 3.10, 172.65 nm. However, this large grouping appears to be a gathering of smaller particles upon closer examination.

The as-prepared amorphous $Ni_{11}As_8$ phase synthesized by the method presented here also produces nanoparticles. TEM images of the $Ni_{11}As_8$ particles always shows large agglomerations of much smaller particles (Figure 3.10). Smaller particles that were distinct enough to accurately measure show an average size of 5 ± 1 nm. The small distribution range is presented in the inset of figure 3.10. The agglomerations observed average to 67 nm ± 36 nm but were seen as large as 129 nm in limited instances.

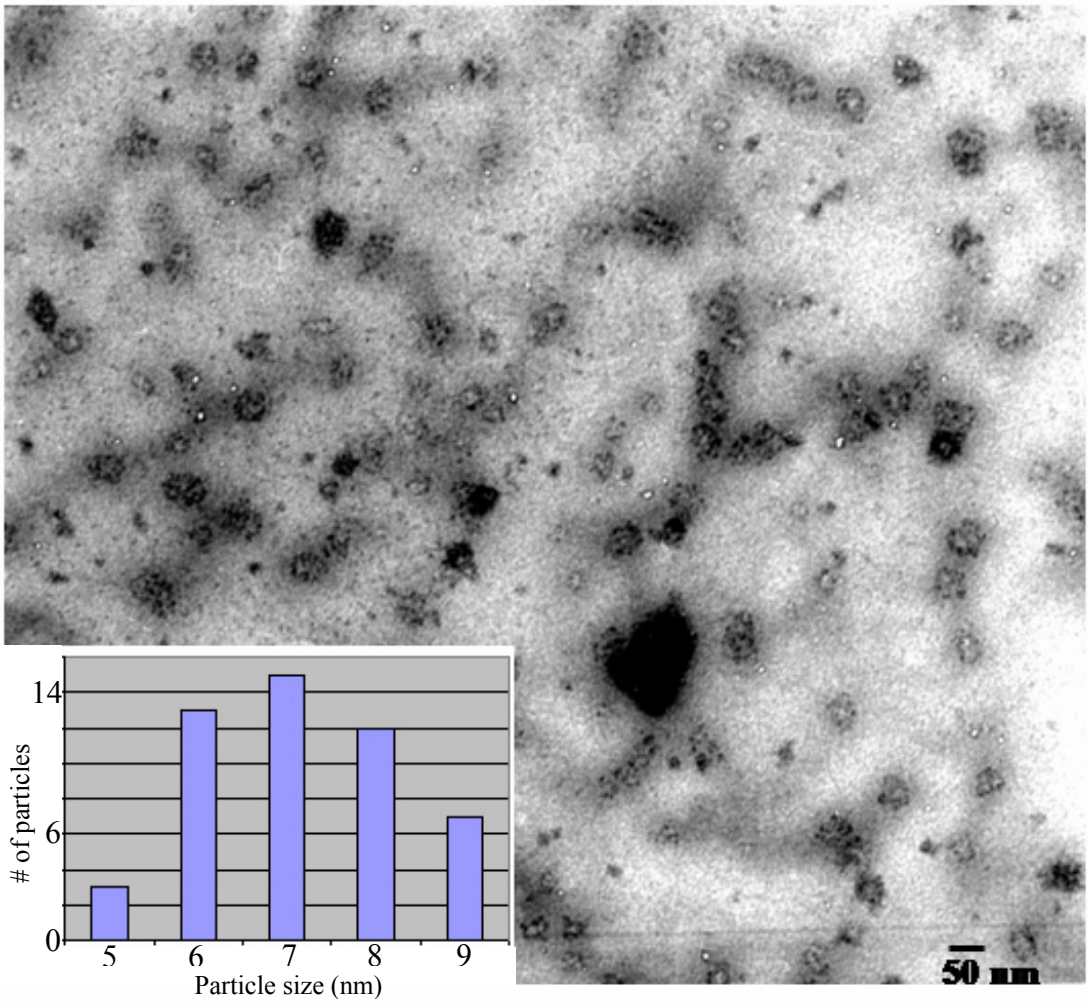

Figure 3. 9. TEM image of $NiAs_2$ sample dispersed with dmf on a copper grid. Inset shows the nanoparticles distribution range from 5-9 nm.

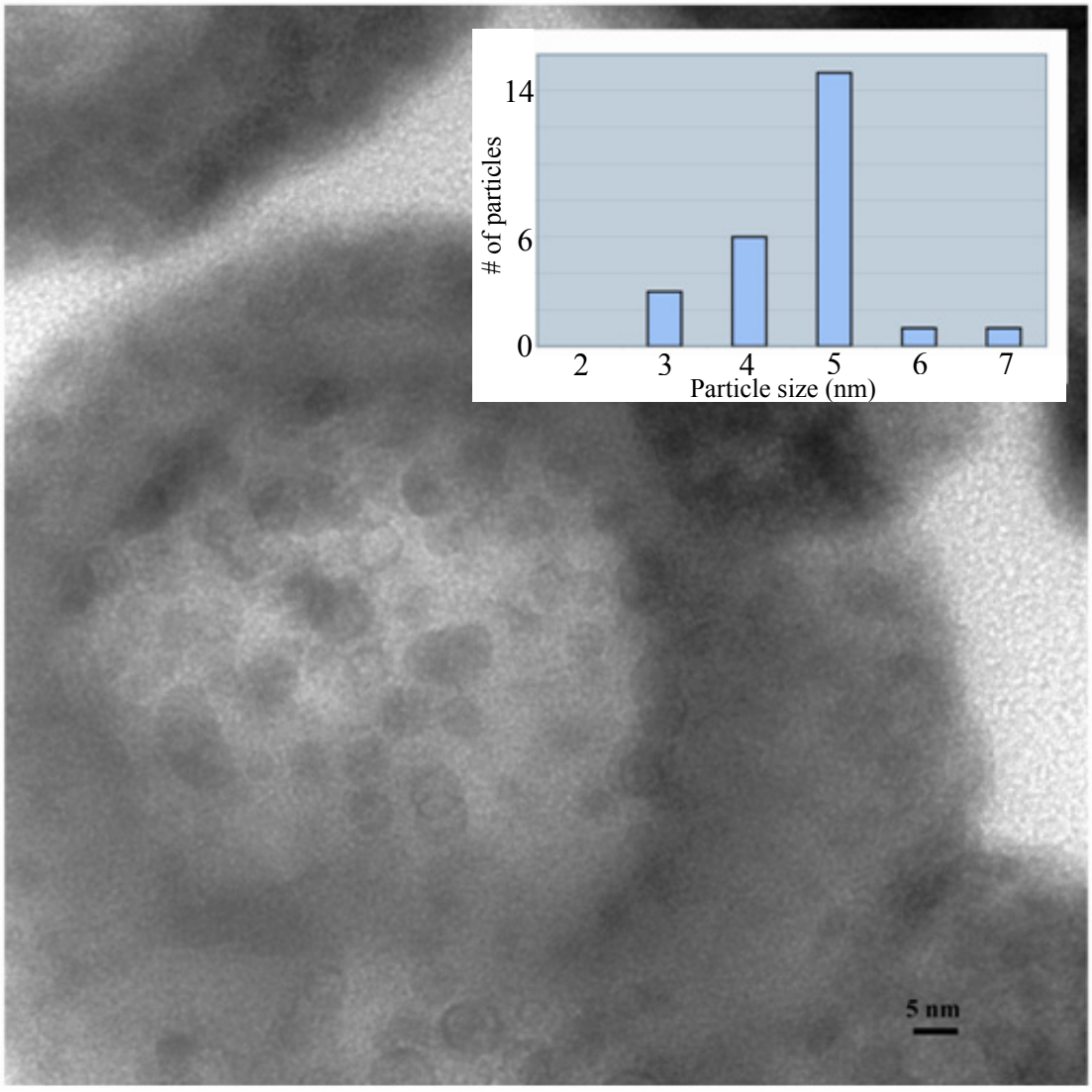

Figure 3. 10. TEM image of Ni11As8 sample dispersed with dmf on a copper grid. Inset shows nanoparticles distribution range.

TEM images of the Ni_5As_2 nanoparticles are more dispersed. Figure 3.11 shows particles with an average size of 9 nm ± 3 nm. The inset in figure 3.11 shows the larger nanoparticle distribution range of this phase. Most of the nanoparticles of this binary phase have two piece morphologies. They have smaller inner cores with thin outer rings offset from their core. Particle sizes were measured including the

outer rings. This core-shell morphology can be seen in the enlarged are of figure 3.11.

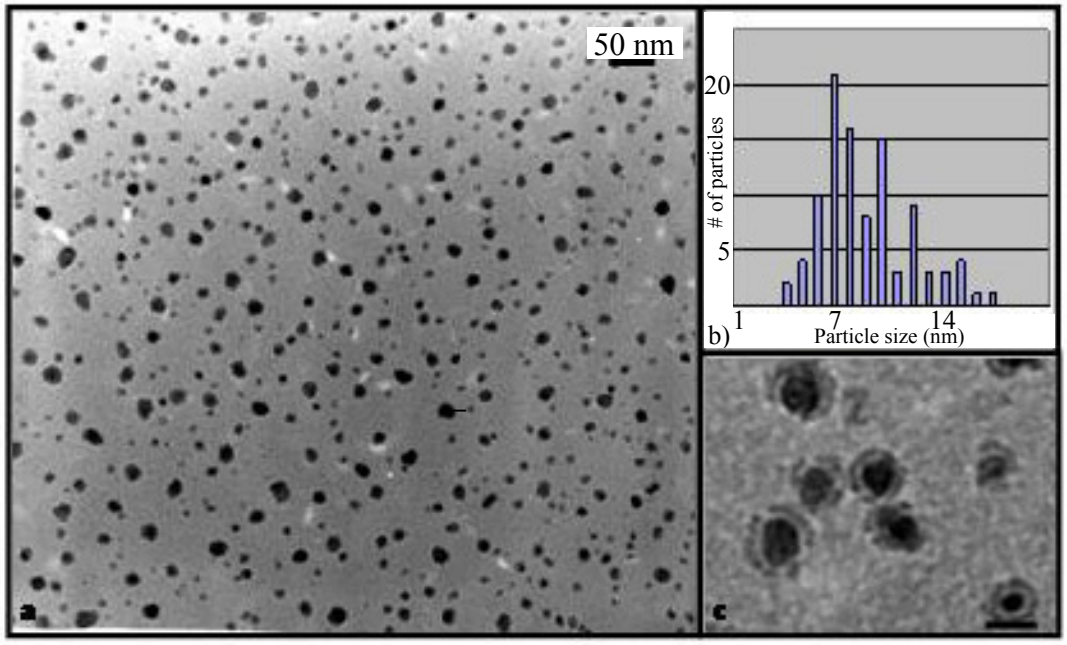

Figure 3. 11. a). TEM image of Ni_5As_2 sample dispersed with dmf on a copper grid. b). Nanoparticles distribution range. c). Enlarged view of particles showing the core-shell morphology (scale bar is 11 nm).

A TEM image of the amorphous as-prepared Ni_5As_2 sample shows lattice fringes on two particles (Figure 3.12). The lattice spacings measured from this image are 6.2 ± 0.1 Å and 12.5 ± 0.1 Å which are in agreement with the spacing of the 002 and 001 reflections, 6.2324 Å and 12.4701 Å, respectively, calculated during the cell refinement of the XRD pattern of the annealed Ni_5As_2. This indicates that the particles imaged in figure 3.12, which are part of the as-prepared sample, are crystalline Ni_5As_2 particles.

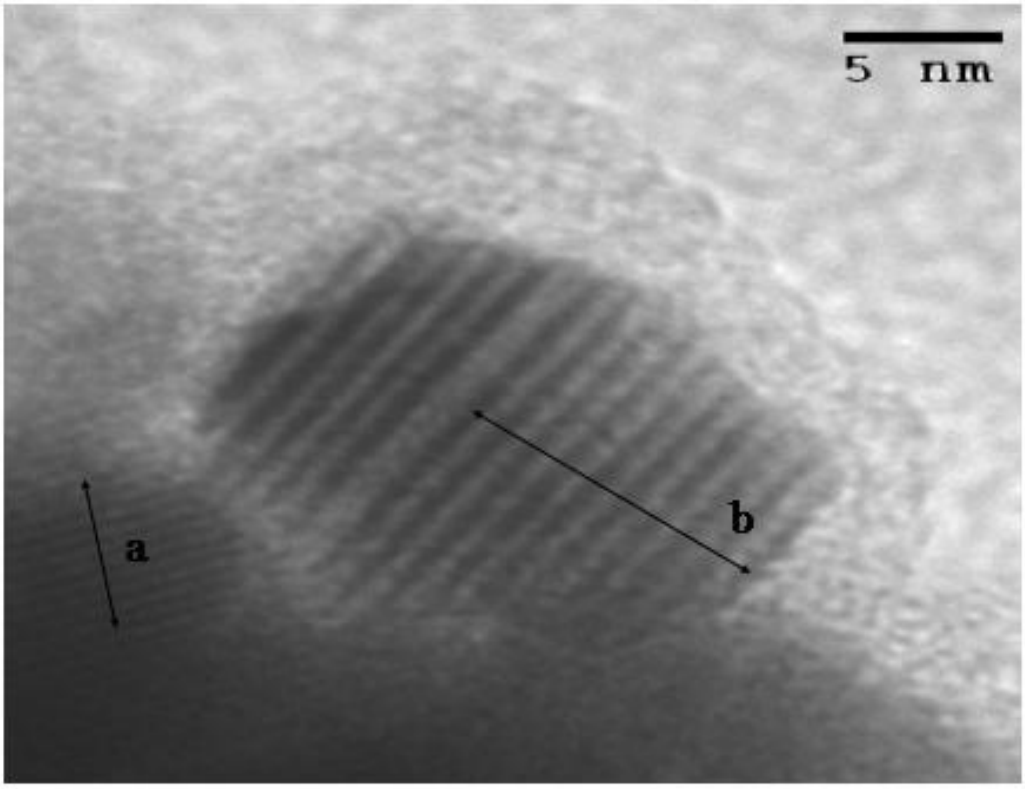

Figure 3. 12. TEM image of Ni_5As_2 nanoparticles with crystalline lattice fringes. The area labeled a shows lattice spacings of 6.2 ± 0.1 Å that represent the 002 hkl reflections. The area labeled b shows lattice spacings of 12.5 ± 0.1 Å that represent the 001 hkl reflections. Image obtained by Kevin McIlwrath at Hitachi.

3.3 Discussion

Use of the Zintl ion, As_7^{3-}, as a precursor provided access to an entire transition-metal / pnictogen binary phase diagram for the first time by a single method at low temperatures. $NiAs_2$, NiAs, $Ni_{11}As_8$, and Ni_5As_2 were each individually obtained by the generic synthetic method set forth in this chapter. Confirmation of the phases obtained in the as-prepared samples could not be

confirmed by a single method, but rather required the results of multiple characterization technique.

X-ray diffraction of the annealed sample indicated a single phase in each sample. The ratio of arsenic and nickel material used in the reactions corresponds to the phase confirmed by XRD. However, the absence of amorphous material in the sample, such as a second phase, metallic nickel or arsenic, can not be confirmed by XRD.

The absence of metallic nickel and arsenic and bulk oxides in the X-ray photoelectron spectra of the annealed samples of each sample ($NiAs_2$, NiAs, $Ni_{11}As_8$, and Ni_5As_2) suggest that the phase indicated by XRD is the only phase present in the sample. The similarity between the X-ray photoelectron spectra of the corresponding as-prepared and annealed sample suggest that they are of the same material. It is unlikely that a phase transition occurred in the samples during the annealing process because it would require metallic arsenic or nickel to be present as bulk component in either the as-prepared or annealed XPS spectra, since stoichiometric ratios of the elements were used in the reactions.

The XPS implies that the as-prepared samples are the same as their corresponding annealed samples. The identity of the crystalline component of each of the annealed samples was determined by XRD. The lack of bulk metallic arsenic or nickel in any of the XPS spectra implies that there are no amorphous phases in the annealed samples due to the reasons listed above. Therefore, it can be inferred that the as-prepared samples are single-phase nanoparticles of $NiAs_2$, NiAs, $Ni_{11}As_8$, and Ni_5As_2, respectively. This statement is further supported by the crystalline lattice

spacings imaged by TEM of the amorphous Ni_5As_2 sample (figure 3.3) that match reflections calculated in the cell refinement of the annealed Ni_5As_2 sample. These *hkl* reflections are further support the desired Ni/As phases are present in all the amorphous samples.

In addition to the first synthetic route that can access an entire transition-metal / pnictogen phase diagram, it is the first solution deposition synthesis of $NiAs_2$, $Ni_{11}As_8$, and Ni_5As_2. The as-prepared $NiAs_2$, $Ni_{11}As_8$, and Ni_5As_2 samples are the first examples of nanoparticles of these phases.

The only XPS data on a Ni/As binary phase previously reported was for the mineral NiAs.[116] The binding energies of both the As 3d and Ni $2p_{3/2}$ electrons were reported for this mined sample. Direct comparison of the bulk NiAs As $3d_{5/2}$ and Ni $2p_{3/2}$ binding energies of the reported mineral and of the NiAs sample reported in this document are the same within experimental error. XPS studies on the remaining phases synthesized and studied here have never been reported. The similarities and differences of the binding energies of these phases ($NiAs_2$, $Ni_{11}As_8$, and Ni_5As_2) compared to those of NiAs discussed and rationale for the differences are proposed.

The $NiAs_2$ sample has an average As $3d_{5/2}$ binding energy in the 41.3 eV region, which is slightly larger than that of the NiAs phase. However, it is the same binding energy reported for the NiAsS phase which has the same crystallographic structure as $NiAs_2$ but As-S dimers in place of the As-As dimers.[115,126] The binding energies reported for $Ni_{11}As_8$ and Ni_5As_2 are at slightly higher energies (table 3.2). This increase may be explained by the shorter nickel-nickel distances[119] in these phases compared to NiAs. With more electrons involved in nickel–nickel

interactions, arsenic atoms in $Ni_{11}As_8$ and Ni_5As_2 have smaller electron density clouds compared to arsenic atoms in NiAs. The decrease in electron density around the arsenic atoms may explain the increase in their As $3d_{5/2}$ binding energies compared to NiAs.

The lowering binding energies of the bulk Ni $2p_{3/2}$ contribution in both $Ni_{11}As_8$ and Ni_5As_2 may also be a result of the smaller nickel-nickel separations seen in these phases, which would foster higher electron density around the nickel atoms. The increased electron density makes it easier to remove an electron, effectively lowering the bulk Ni $2p_{3/2}$ binding energies.

The high temperature method for obtaining single-phase Ni/As samples was quite effective. However, the high temperatures used produce bulk materials. The miniaturization of today's technology makes this method, which does not allow nanoparticle formation, an undesirable synthetic method. The simple low temperature method set forth here is not only a milder synthetic route but requires little specialty instrumentation such as high temperature furnaces. Perhaps the most important thing this low-temperature method contributes is that the desired phases are present as nanoparticles. What sets this unique method for isolating phase-specific samples apart from other methods is the use of Zintl anions, organic-free, molecular main group sources. It is likely that it is this property that promotes the isolation of any phase-specific samples on the binary phase diagram. The range of known Zintl anions and availability of zero-valent transition-metals open up a wide range of binary phases that may be isolated as binary nanoparticles.

3.4 Experimental Section

3.4.1. General

Reactions were performed in a Vacuum Atmosphere Co. dry box with a nitrogen atmosphere. A Bruker D8 Advance θ-θ X-ray Powder Diffractometer (CuK_α radiation, Kevex detector) was used to obtain XRD patterns for phase identification. A step width of 0.02º between of 5º ≤ 2θ ≥ 90º was used. Analysis of the XRD patterns was done using the JADE® software package equipped with the JC-PDF database and auto indexing.[127] Cell refinements were done on each pattern using the JADE® software package refine to zero-offsets of 0.0442(0.01064)º or smaller. The cell refinements have ESDs of the fits between 0.0045º and 0.0235º. The cell parameters match those given for the respective JCPDS card ($NiAs_2$, #11-0014; NiAs, #31-0900; $Ni_{11}As_8$, #08-0085; Ni_5As_2, #10-0271).

XPS measurements were collected on a Kratos Axis 165 spectrometer by Dr. Bindu Varughese. Samples were prepared by dusting the particles on conductive carbon tape mounted on a sample stub. NiAs measurements used a monochromatic Al Kα radiation at a vacuum of 4e-10 Torr. $NiAs_2$, $Ni_{11}As_8$, and Ni_5As_2 measurement were all carried out using a non-monochromatic Mg Kα radiation at a vacuum of 4e-10 Torr. Hybrid mode was used for measurements employing both electrostatic and magnetic lenses, with a step size of 0.1 eV and a sweep time of 60 s. The As 3d and Ni 2p spectra regions were recorded in the FAT analyzer mode with a pass energy of 80 eV and an average of 10 scans. During the single region-scan acquisitions, the

energy resolution was approximately 1.5 eV, and a charge neutralizer was not used for these measurements.

The depth profiling studies done by argon ion milling were done at a pressure of 3.2e-7 Torr. Parameters used for etching were 15 mA and 4 KV. Successive etching measurements were performed on the same 120 μm spot. Each depth profile had binding energy calibration done with respect to C 1s at 285.0 eV.

Vision processing software was used for all data processing. The spectra were fit, after the linear background was subtracted, with 60% Gaussian / 40% Lorentzian peaks. The minimum number of peaks consistent with the best fit was used to deconvolute the spectral envelopes.

Samples for TEM imaging were prepared by dispersing the sample in ~ 1 mL of dmf. A couple drops of the mixture were further dispersed in and 0.5 mL of dmf and a drop was placed on copper grid. Excess solvent was wicked away by absorbent paper and the grid was allowed to dry. The TEM images in figures 3.6 and 3. 8 were collected on a Zeiss EM 10CA Transmission Electron Microscope at an accelerating voltage of 80 kV. TEM images in figures 3.3 and 3.7 were taken on a Hitachi Model H-7600 at acceleration voltages of 110 kV and 120 kV, respectively. Nine to ten lattice spacings of each particle seen in figure 3.12 were measured 10 times to determine the average distance of the lattice spacings.

3.4.2 Chemicals

A nominal melt of K_3As_7 was prepared by fusion of the elements in a sealed quartz tube under vacuum with a natural gas-oxygen torch. ***CAUTION!!*** $Ni(COD)_2$

was purchased from STREM Chemicals. Iodine metal was purchased from CERAC, and PVP was purchased from Aldrich. Anhydrous en and dmf were purchased from Fischer, were distilled from K_4Sn_9 and stored in a nitrogen atmosphere. Toluene was distilled from NaK and stored under a nitrogen atmosphere. Reagent grade Acetonitrile was used without further purification. Concentrated HCl was diluted to 0.01M with deionized water.

3.4.3 Phase-Specific Synthesis

3.4.3.1 Preparation of $NiAs_2$

K_3As_7 (30 mg, 0.047 mmol) was dissolved in en (~ 1 mL) in vial 1. In vial 2, $Ni(COD)_2$ (45 mg, 0.164 mmol) was dissolved in tol (~ 1 mL). Both vials were heated to 50-60 ºC and held for 5 minutes. The solution in vial 2 turns from a yellow to green. The solutions are then heated to 80-85 ºC until the solution in vial 2 becomes a darker green with precipitate. The heat was turned off; then, vial 2 is added drop-wise to vial 1 and the resulting solution is stirred 30s to 1 min before a dmf solution (~ 0.25 mL) of iodine (24.5 mg, 0.097 mmol) is added. The solution is stirred over night. The reaction was removed from the drybox and centrifuged to facilitate removal of the supernatant. The black precipitate was washed by acetonitrile, 0.01M HCl and again by acetonitrile. The black material was dried in air for about 1 hour. A 80% yield of $NiAs_2$ was isolated. Half of the material was annealed in an evacuated, sealed pyrex tube for 5 hours at 400 ºC.

3.4.3.2 Preparation of NiAs

K_3As_7 (15 mg, 0.023 mmol) was dissolved in en (~ 1 mL) in vial 1. In vial 2, $Ni(COD)_2$ (45 mg, 0.164 mmol) was dissolved in tol (~ 1 mL). Both vials were heated to 50-60 ºC and held for 5 minutes. The solution in vial 2 turns from a yellow to green. The solutions are then heated to 80-85 ºC until the solution in vial 2 becomes a darker green with precipitate. Then, vial 2 is added drop-wise to vial 1 and the resulting solution is stirred 30s to 1 min before a dmf solution (~ .25 mL) of iodine (10 mg, 0.039 mmol) is added. The solution is stirred over night. The reaction was removed from the drybox and centrifuged to facilitate removal of the supernatant. The black precipitate was washed by acetonitrile, 0.01M HCl and again by acetonitrile. The black material was dried in air for about 1 hour. A 77% yield of NiAs was isolated. Half of the material was annealed in an evacuated, sealed pyrex tube for 5 hours at 400 ºC.

3.4.3.3 Preparation of $Ni_{11}As_8$

K_3As_7 (15 mg, 0.023 mmol) and 29,000 MW PVP (10 mg, 0.345 μmol) were dissolved in en (~ 1 mL) in vial 1. In vial 2, $Ni(COD)_2$ (61.9 mg, 0.222 mmol) was dissolved in tol (~ 1 mL). Both vials were heated to 70 ºC and held for 5 minutes. The solution in vial 2 turns from a yellow to green with precipitate. Then, vial 1 was poured into vial 2 and the mixture is heated to 88 ºC over 3 minutes. The heat was turned off and the mixture was stirred for another 3 hours. The reaction was removed from the drybox and centrifuged to facilitate removal of the supernatant. The black precipitate was washed by acetonitrile (2x), 0.01M HCl and again by acetonitrile.

The black material was dried in air for about 1 hour. A 72% yield of $Ni_{11}As_8$ was isolated. Half of the material was annealed in an evacuated, sealed pyrex tube for 5 hours at 400 ºC.

3.4.3.4 Preparation of Ni_5As_2

K_3As_7 (15 mg, 0.023 mmol) and 29,000 MW PVP (10 mg, 0.345 μmol) were dissolved in en (~ 1 mL) in vial 1. In vial 2, $Ni(COD)_2$ (112.5 mg, 0.409 mmol) was dissolved in tol (~ 2 mL). Both vials were heated to 65 ºC and held over 10 minutes. Then, both vials are heated at 80-85 ºC for 5 minutes. The heat is turned off before the contents of vial 1 were added slowly to the green solution with precipitate in vial 2. The heat was turned off and the mixture stirred over night. The reaction was removed from the drybox and centrifuged to facilitate removal of the supernatant. The black precipitate was washed by acetonitrile, 0.01M HCl and again by acetonitrile. The black material was dried in air for about 1 hour. A 97% yield of Ni_5As_2 was isolated. Half of the material was annealed in an evacuated, sealed pyrex tube for 5 hours at 400 ºC.

Chapter 4

Synthesis and characterization of the charged molecular intermetallics, $[(Ni_2Sb_2)(Sb_7)_2]^{4-}$, $[Ni_5Sb_{16}]^{4-}$ and $[Pd_7As_{16}]^{4-}$: Crossing the "Zintl-Klemm Border"

4.1 Introduction

Recent studies of ligand stabilized, large metallic and binary molecular clusters have indicated that these cluster are essentially discrete pieces of bulk metallic or binary lattice stabilized by organometallic ligands.[128,129] The examples of the binary clusters are typically chalcogenide clusters and occasionally have unique molecular binary cores that do not structurally mimic any binary phase. Some studies suggest that whether the binary clusters will resemble solid-state phases or be molecular in nature is dependent on the stabilizing ligands.[130] These large clusters provide a unique medium for studying the line between solid-state and molecular structures.

While a variety of chalcogenide binary clusters have been reported that fall along this line, pnictogen binary cluster in this region have been less studied. Zintl ion complexes constitute the majority of this emerging class of transition-metal / pnictogen binary cluster anions.[44,50,79,95,131] In the absences of the organic ligands used to stabilize the first reported transition-metal / Zintl complexes, new Zintl structures have been isolated. The new structures include the crown-like E_8 rings

seen in the ME_8^{-n} series (M = Nb, Cr, Mo; E = As, Sb; n =2, 3), the As_{20} fullerane cage of $[As@Ni_{12}@As_{20}]^{3-}$, and the Pb_{12} icosahedra cage of $[Pt@Pb_{12}]^{2-}$. [44,50,79,131]

Homonuclear main group polyanions, also known as Zintl ions, have unique properties, which include but are not limited to their electron count / charge distribution. Their electron count / charge distribution is understood by the Zintl-Klemm formalism,[132,133] and in the case of the group 15 Zintl ions, the atoms have structural characteristics isoelectronic to carbon, where $CH \cong E$ (E = P, As, Sb).[134] This formalism is used to assign structure and formal charge, but the accuracy of these assignments is often questioned.[50,135] A more thorough explanation of the Zintl-Klemm formalism is presented in the bond analysis section of this chapter (section 4.3). Following the formalism, the E_8 rings of the $[ME_8]^{-n}$ (M = Nb, Cr, Mo; E = As, Sb; n = -2, -3) series are isoelectronic to cyclooctane, $CH_2 \cong E^-$, giving the rings a –8 formal charge. This assignment has been helpful in comparing the series and predicting their magnetic properties.[50] However, the –8 formal charges require high transition-metal oxidation states which do not reflect actual atomic charges.[44,50] Similarly, Sevov and Bobev reported the Zintl ion complex, $Rb_4Li_2Sn_8$, but were uncertain whether to describe it as an arachno-$[Sn_8]^{-6}$ or a closo-$[Li_2Sn_8]^{4-}$ deltahedral cluster.[135]

In relating the naked Zintl anions, the carbonyl and phosphine ligated transition-metal / Zintl anion complexes, and the more recent binary cluster anions, a formalism which would take into account all types of bond lengths would be essential. A formalism that accounts for bond length is especially needed for heavier main group elements, such as antimony, which are known to have a bond continuum

(no real cut-off between π and σ- bonds and between σ and non-bonding separations).[136] A bond valence formalism initially designed by O'Keeffe and Brese[137] for metal oxides was adapted for rare earth antimony Zintl phases by Jeitschko[136]. The bond valence formalism integrates the Zintl-Klemm concept with bond-length, bond-strength relationships; therefore, the formalism does not require a preconceived cut-off between π and σ-bonds or between σ and non-bonding separations. Optimization of this formalism for alkali 2,2,2-crypt salts of transition-metal / Zintl ion complexes is presented in this chapter. The optimization of the formalism and use with the unprecedented Sb_{16} and Sb_{17} cages are reported for the first time here in the novel binary cluster anions, $[Ni_2Sb_{16}]^{4-}$, **4.1**, and $[Ni_5Sb_{17}]^{4-}$, **4.2**, respectively. The structural relationship between these new clusters and $[Pd_2As_{14}]^{4-}$, **4.3**, and $[Pd_7As_{16}]^{4-}$, **4.4**, respectively, [95] will also be presented.

The clusters presented here were initially presumed to be Zintl clusters but through the studies documented here fail to fit into a Zintl-Klemm type description and can be considered to lie along the "Zintl-Klemm border". Characteristics of clusters that traverse this border are the same as those that differentiate solid-state intermetallic and molecular clusters. These properties include delocalized bonding, non-integral oxidation states and bond continua of element-element bonding. The bond valence formalism allows these properties to be addressed. The bond valence formalism can be use to both develop a charge distribution picture of the clusters and help to determine which side of the "Zintl-Klemm border" a cluster resides.

4.2 Results

4.2.1 Synthesis

Ethylenediamine (en) solutions of $Ni(COD)_2$ and K_3Sb_7, in a 0.5:8 (Ni:Sb) molar ratio, react in the presence of 2,2,2-crypt to give $[K(2,2,2\text{-crypt})]_4[Ni_{2+x}Sb_{16}]\cdot 2en$. The crystalline solid contains the $[(Ni_2Sb_2)(Sb_7)_2]^{4-}$ ion, **4.1**, that forms a solid solution with the $[(Ni_2Sb_2)Ni(Sb_7)_2]^{4-}$ and / or $[(Ni_2Sb_2)Ni_2(Sb_7)_2]^{4-}$ ions on the same crystallographic site. Mixtures of these anions in the crystal lattice give rise to a composite anion formula of $[(Ni_2Sb_2)Ni_x(Sb_7)_2]^{4-}$ with x values that range from 0.10 to 0.23 in the three different samples that were crystallographically characterized.

There are four possible Ni atom positions within every anion in the crystal lattice of this complex (figure 4.1a). The Ni1 and Ni1' positions are filled in every anion. One of the Ni2 and Ni2' positions may be filled ($[Ni_3Sb_{16}]^{4-}$) and / or both ($[Ni_4Sb_{16}]^{4-}$) in some of the anions while neither position is filled in other anions ($[Ni_2Sb_{16}]^{4-}$, **4.1**). The sum of the Ni2 and Ni2' occupancies is reflected in the value of x. Single crystal X-ray diffraction of three crystals from two separate reactions gives an x-range of ($0.10 \leq x \leq 0.23$) for the $[Ni_{2+x}Sb_{16}]^{4-}$ complexes.

Whern a higher Ni:Sb ratios (1:8) is used, $[K(2,2,2\text{-crypt})]_4[Ni_5Sb_{17}]\cdot$en co-crystallizes, in small quantity, with the $[Ni_{2+x}Sb_{16}]^{4-}$ salt. Dark crystals of the complexes $[Ni_{2+x}Sb_{16}]^{4-}$ and $[Ni_5Sb_{17}]^{4-}$ begin precipitating from the solution in low yields (10-11% based on $[Ni_{2+x}Sb_{16}]^{4-}$) within 24-48 hours. Complexes **4.1** and **4.2**

have been differentiated by semi-quantitative Energy Dispersive X-ray analysis (EDX) and single-crystal X-ray diffraction.

In a similar reaction, toluene solutions of $Pd(PCy_3)_2$ ($(PCy)_3$ = tricyclohexyl phosphine) react with en solutions of K_3As_7 in the presents of 2,2,2-crypt to give $[Pd_7As_{16}]^{4-}$, **4.4**, as the $[K(2,2,2\text{-crypt})]^{1+}$ salt in low yield. $[Pd_7As_{16}]^{4-}$ co-crystallizes with the more predominant $[Pd_2As_{14}]^{4-}$, **4.3**, cluster. Complex **4.4** has been characterized by semi-quantitative EDX analysis, electrospray mass spectrometry (ESI-MS) and single crystal x-ray diffraction.[95]

4.2.2 Solid State Structures

$[Ni_{2+x}Sb_{16}]^{4-}$ $[K(2,2,2\text{-crypt})]_4[Ni_{2+x}Sb_{16}]\cdot 2en$ crystallizes with triclinic crystal symmetry, space group P-1, and contains the anion, four cations and two en solvate molecules in the unit cell. Partially occupied Ni positions are located slightly below the centroid of the irregular rectangular face created by the Sb2, 3, 5 and 6 atoms of the Sb_7^{2-} cages (figure 4.1a). When these Ni atoms are present, they are in highly distorted trigonal prismatic environments with Ni-Sb bonds ranging from 2.559(18) to 2.657(17) Å. These bond distances determined crystallographically represent weighted averages of the various possible anions present in the crystal lattice ($[Ni_2Sb_{16}]^{4-}$, $[Ni_3Sb_{16}]^{4-}$, and $[Ni_4Sb_{16}]^{4-}$). Throughout the remainder of this paper, **4.1** will refer to the anion $[Ni_2Sb_{16}]^{4-}$, from $[Ni_{2+x}Sb_{16}]^{4-}$ when x = 0.10. The crystal data are summarized in tables 4.1 and selected bond distances and angles are given in table 4.3.

Two partially occupied Ni positions are located inside the Sb_7 cages. Single-crystal X-ray analysis of three crystals from two separate reaction mixtures each had different occupancy values. Assuming the limiting structure $[Ni_4Sb_{16}]^{4-}$, the occupancy of each of the symmetrically equivalent Ni2 positions range from 5-11.5%. According to Wade-Mingos electron counting rules, the number of electrons a transition-metal located within a cluster donates to the skeletal electron count is equal to [10 – (group #)].[138] Consequently, the nickel atoms that occupy the two Ni2 positions within the E_7 clusters are zero valent and donate zero electrons to the skeletal electron count. Therefore, their occupancy does not alter the charge or skeletal electron count, thereby allowing for a continual solid solution without affecting charge or general structure. While the general structure of the anions from the three separate determinations remains unchanged, the actual Sb-Sb bond distances of the Sb_7^{2-} cages appear to extend and contract in relation to the positions held by the Ni2 atoms. However, the distances are weighted averages of all the anions, $[Ni_2Sb_{16}]^{4-}$, $[Ni_3Sb_{16}]^{4-}$ and/or $[Ni_4Sb_{16}]^{4-}$, present in the crystal lattice and not the actual bond distances. Each Ni2 atom position is within bonding distances to both Ni1 atoms creating a Ni_4^{+2} rhombus, but due to the low occupancies of the Ni2 positions are presumably rarely present at the same time. The Ni1– Ni2 (i.e. Ni(I) – Ni(0)) bond distances (2.524(16) and 2.559(14) Å, **4.1**) are shorter than the Ni(I)-Ni(I) separation but between known Ni(0)-Ni(0) and Ni(I)-Ni(I) separations and are only slightly longer than metallic Ni-Ni distances (2.49Å).[139] The complex $[Ni_2(CO)_4(\mu\text{-}PPh_3)_2]^{-n}$ (n = 2,0) has been isolated as a non-bonding, neutral Ni_2^0 dimer (3.397(1) Å) and a bonding Ni_2^{+2} dimer (2.510(2) Å).[140 141] It is interesting to note that

Table 4. 1. Select crystallographic data for complexes $[K(2,2,2\text{-crypt})]_4$(**4.1**) • 2en and $[K(2,2,2\text{-crypt})]_4$(**4.2**) • en.

	$[K(2,2,2\text{-crypt})]_4$(**4.1**) • 2en	$[K(2,2,2\text{-crypt})]_4$(**4.2**) • en
formula	$C_{76}H_{160}K_4N_{12}O_{24}Ni_{2.10}Sb_{16}$	$C_{74}H_{152}K_4N_{10}O_{24}Ni_5Sb_{17}$
fw	3853.85	4085.76
T [K]	203(2)	173(2)
$\lambda_{MoK\alpha}$ [Å]	0.71073	0.71073
space group	P-1	P-1
a [Å]	14.3183(11)	15.510(3)
b [Å]	15.8901(12)	16.661(3)
c [Å]	16.4077(12)	25.943(5)
α [˚]	95.711(2)	86.253(4)
β [˚]	110.642(2)	81.860(4)
γ [˚]	111.677(2)	66.513(3)
V [$Å^3$]	3131.0(4)	6086.3(19)
Z	1	2
ρ_{calcd} [g cm^{3-}]	2.044	2.229
μ [mm^{1-}]	3.887	4.650
crystal size [mm]	0.20 x 0.07 x 0.03	0.20 x 0.15 x 0.04
reflections collected	42454	42595
independent	11006 [R(int) = 0.0405]	21436 [R(int) = 0.0334]
final R [I >2σ(I)]	R1 = 0.0339, wR2 = 0.0857[a]	R1 = 0.0443, wR2 = 0.1072[b]
R indices (all data)	R1 = 0.0587, wR2 = 0.0928[a]	R1 = 0.0768, wR2 = 0.1168[b]

[a]. The function minimized during the full-matrix least-squares refinement was $\Sigma w(Fo^2-Fc^2)$ where $w=1/[\sigma^2(Fo^2)+(0.050*P)^2+1.3423*P]$ and $P=\max(Fo^2,0)+2*Fc^2)/3$. [b]. The function minimized during the full-matrix least-squares refinement was $\Sigma w(Fo^2-Fc^2)$ where $w=1/[\sigma^2(Fo^2)+(0.0491*P)^2+22.2174*P]$ and $P=\max(Fo^2,0)+2*Fc^2)/3$.

Table 4. 2. Select crystallographic data for $[K(2,2,2\text{-crypt})]_8(\mathbf{4.4})_2 \bullet 3.5en$.

	$[K(2,2,2\text{-crypt})]_8(\mathbf{4.4})_2 \bullet 3.5en$
formula	$C_{151}H_{316}K_8N_{23}O_{48}Pd_{14}As_{16}$
fw	7422.10
T [K]	193(2)
$\lambda_{MoK\alpha}$ [Å]	0.71073
space group	P-1
a [Å]	17.2784(9)
b [Å]	27.2637(15)
c [Å]	28.9377(16)
α [˚]	113.4360(10)
β [˚]	99.2890(10)
γ [˚]	99.6560(10)
V [$Å^3$]	11931.4(11)
Z	2
ρ_{calcd} [g cm^{3-}]	2.066
μ [mm^{1-}]	5.639
crystal size [mm]	0.500 x 0.200 x 0.021
reflections collected	143867
independent	42004 [R(int) = 0.0691]
final R [$I > 2\sigma(I)$]	R1 = 0.0534, wR2 = 0.1294[a]
R indices (all data)	R1 = 0.1180, wR2 = 0.1485[a]

[a]. The function minimized during the full-matrix least-squares refinement was $\Sigma w(Fo^2-Fc^2)$ where $w=1/[\sigma^2(Fo^2)+(0.0685*P)^2+0.0*P]$ and $P=\max(Fo^2,0)+2*Fc^2)/3$.

Table 4. 3. Select bond distances (Å) and angles (º) for $[Ni_{2.10}Sb_{16}]^{4-}$.

Sb1-Sb4	2.7527(6)	Sb7-Sb1-Sb4	94.314(18)
Sb1-Sb7	2.7563(6)	Sb3-Sb2-Sb7	102.149(18)
Sb2-Sb3	2.7922(6)	Sb7-Sb2-Sb8	79.200(17)
Sb2-Sb7	2.8669(7)	Sb2-Sb3-Sb4	102.962(19)
Sb2-Sb8	3.0805(7)	Sb3-Sb4-Sb5	97.172(17)
Sb3-Sb4	2.8693(6)	Sb1-Sb4-Sb3	105.09(2)
Sb3-Sb8	3.0498(7)	Sb1-Sb4-Sb5	105.72(2)
Sb4-Sb5	2.8759(6)	Sb4-Sb5-Sb8’	80.893(16)
Sb5-Sb6	2.7614(6)	Sb4-Sb5-Sb6	101.803(19)
Sb5-Sb8’	3.0766(6)	Sb5-Sb6-Sb7	103.888(19)
Sb6-Sb7	2.8681(7)	Sb7-Sb6-Sb8	79.211(17)
Sb6-Sb8	3.0787(6)	Sb2-Sb7-Sb6	98.640(18)
Ni1-Ni1’	2.6751(16)	Sb4-Sb5-Sb8’	80.893(16)
Ni1-Ni2	2.559(14)	Sb4-Sb5-Sb6	101.803(19)
Ni1-Ni2’	2.524(16)	Sb5-Sb6-Sb7	103.888(19)
Ni1-Sb2	2.5945(9)	Sb7-Sb6-Sb8	79.211(17)
Ni1-Sb3	2.6258(9)	Ni1-Sb8-Ni1’	64.52(3)
Ni1’-Sb5	2.6200(8)	Ni2-Ni1-Ni2’	116.5(3)
Ni1’-Sb6	2.6101(9)	Sb8-Ni1-Sb8’	115.48(3)
Ni2-Sb2	2.648(17)	Sb2-Ni1-Sb5’	102.98(3)
Ni2-Sb3	2.568(17)	Sb2-Ni1-Sb3	64.67(2)
Ni2-Sb4	2.584(16)	Ni1-Ni2-Ni1’	63.5(3)
Ni2-Sb5	2.521(17)	Sb2-Ni2-Sb3	64.7(4)
Ni2-Sb6	2.559(18)	Sb5-Ni2-Sb3	115.7(7)
Ni2-Sb7	2.657(17)	Sb5-Ni2-Sb6	65.9(4)

the Ni(I)-Ni(0) distances of $[Ni_{2.10}Sb_{16}]^{4-}$ more closely resemble the separation seen for the Ni_2^{+2} dimer rather than an intermediate distance between the two types of Ni-Ni separations. The closer similarity to the Ni_2^{+2} dimer suggests that the short separation is presumably due to structural restrictions and occupancy of the Ni(0) atom and not the oxidation states of the metals.

The anion, **4.1**, (figure 4.1) resides on the crystallographically imposed inversion center and has virtual D_{2h} point symmetry. The anion can be viewed as two norbornadiene-like Sb_7^{2-} cages each coordinated in an η^2,η^2 fashion to a $[Ni_2(\mu\text{-}Sb)_2]$ ring (figure 4.1b). Similar four member rings of Ni(I) dimers bridged by two pnictogen ligands have been reported in the literature (i.e. $[Ni_2(CO)_4(\mu\text{-}Sb^tBu_2)_2]$, **4.5**, $[Ni_2(CO)_4(\mu\text{-}PPh_2)_2]$, $[(Me_3P)Ni(\mu\text{-}^tBu_2As)]_2$).[141-143]

The structural properties of the $[Ni_2(\mu\text{-}Sb)_2]$ ring in **4.1** closely resemble those of the ring in the stibinido-bridged Ni(I) dimer, $[Ni_2(CO)_4(Sb^tBu_2)_2]$, **4.5**.[144] Each Ni1 atom forms Ni-Sb bonds with both Sb8 atoms (2.4993(9)Å and 2.5123(9) Å) forming the ring. Large Sb-Ni-Sb angles are observed in both complexes (115.348(3)°, **4.1**; 111.54(4)°, **4.5**) along with acute Ni-Sb-Ni angles (64.52(3)°, **4.1**; 68.40(6) and 68.51(6)°, **4.5**). The Ni1 atoms bridging the two norbornadiene-like cages in **4.1** make Ni-Sb bonds to the Sb_7 cages that range from 2.5945(9) to 2.6258(9) Å.

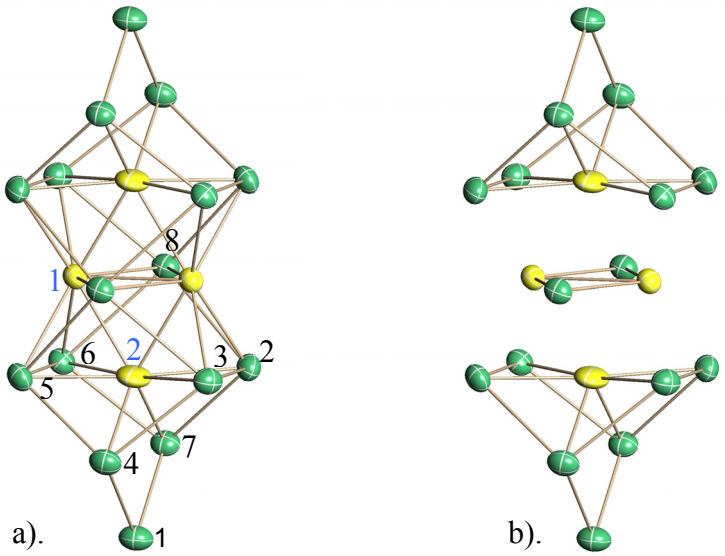

Figure 4. 1. a). ORTEP drawing of the $[(Sb_7)_2Ni_{0.10}(Ni_2Sb_2)]^{4-}$ complex. Black atoms labeled with underlined numbers represent Ni atoms, and the white atoms with regular numbering represent Sb atoms. b). An ORTEP drawing of the 2Sb7 and Ni_2Sb_2 subunits that make-up the $[(Sb_7)_2(Ni_2Sb_2)]^{4-}$ structure. Some bonds are omitted for clarity. All thermal ellipsoids are at 50% probability.

Considering the Sb_7 units as dienes, the Ni1 atoms are in tetrahedral environments. The Ni1-Ni1' distance (2.6751(16) Å) is within the bonding range of edge-shared tetrahedral Ni(I) dimers that contain bridging pnictogen ligands and a Ni-Ni bond (2.375(3) – 2.757(2) Å).[140,142,145] The covalent radius of the bridging pnictogen atom directly affects the Ni(I) - Ni(I) distance. Therefore, the larger radius of antimony atoms is consistent with a nickel-nickel separation at the higher end of the known range of Ni(I) dimers. While the Ni1-Ni1' separation of $[(Ni_2Sb_2)(E_7)_2]^{4-}$ is within bonding separations, electron counting indicates that each Ni1 atom has 18 valence electrons when the Sb_7 cages are viewed as two diene ligands and there are

two Ni=Sb double bonds within the [cyclo-Ni_2Sb_2] ring. Since both nickels have 18 valence electrons, a Ni1-Ni1' bond will not occur.

Antimony – antimony bond distances within the norbornadiene cages range from 2.7527(6) to 2.8759(6) Å and are similar to those observed in the [η^4-$Sb_7M(CO)_3]^{3-}$ series (M = Cr, Mo, W)[18]. The Sb8 atoms (see figure 4.1) link the two Sb_7^{2-} cages with long Sb-Sb contacts of 3.0498(7) to 3.0805(7) Å. For comparison, these contacts are ca. 0.3 Å shorter than the interlayer Sb-Sb interactions in α-Sb[115] but longer than a typical single bond distances (2.700(2) - 2.935(8) Å).[49,146,147] This difference suggests that the Sb8 atoms of **4.1** form partial bonds to the Sb_7 cages. The degree of partial bonding will be further discussed in the next section.

Complex **4.1** is similar to $[Pd_2As_{14}]^{4-}$, **4.3**[95], which can be viewed as a Pd_2^{+6} dimer with norbornane-like As_7^{5-} cages. Interestingly, the $M_2(E_7)_2$ cores of the two complexes differ only by a 90° rotation of the M_2 unit within the $(E_7)_2$ ligand sphere (fig 4.2). This rotation places the Pd(III) atoms of **4.3** in the Sb8 positions of **4.1** (figure 4.2), relative to the E_7 cages. The different M_2 arrangements leave the Ni ions in tetrahedral environments (considering the Sb-Sb units as olefin analogs) whereas the formally Pd(III) ions are in square planar arrays.

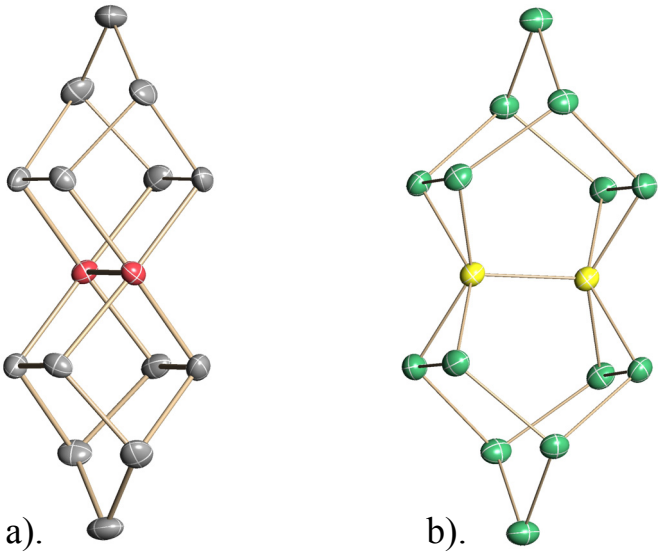

Figure 4. 2. a). ORTEP drawing of $[Pd_2(As_7)_2]^{4-}$, ion 4. b). An ORTEP drawing of the $[(Ni_2Sb_2)(Sb_7)_2]^{4-}$ structure, 1, with the Sb8 atoms removed for clarity. Red and yellow atoms represent the palladium and nickel atoms, respectively. The grey and green atoms represent arsenic and antimony atoms, respectively. For comparison, the relative orientations of the E_7 groups are the same in both drawings. All thermal ellipsoids are at 50% probability.

$[Ni_5Sb_{17}]^{4-}$ The $[K(2,2,2\text{-crypt})]_4[Ni_5Sb_{17}]\cdot en$ salt has triclinic crystal symmetry and space group P-1, but the inversion center is not crystallographic imposed upon the anion. The structure of $[Ni_5Sb_{17}]^{4-}$ has rotational disorder and was refined to possess two complete molecules. These two molecules occupy the same location with a final ratio of 0.8125:0.1875. The crystal data are summarized in table 4.1, and selected bond distances and angles are given in table 4.4. The $[Ni_5Sb_{17}]^{4-}$ anion, **4.2**, (figure 4.3a) has virtual C_{4v} point symmetry and can be viewed as an $[Sb_{13}]$ bowl (see figure 4.3b) with a $[Ni(cyclo\text{-}Ni_4Sb_4)]$ lid.

The apical Ni5 atom is in a distorted Sb_5 square pyramidal environment with an average Ni-Sb bond distance of 2.59 ± 0.03 Å. The four other Ni atoms are in

distorted 5+1 trigonal prismatic environments with five Ni-Sb bonds in the range 2.496(3) to 2.590(2) Å. The longer Ni-Sb contact is in the range 2.7825(16) to 2.8445(16) Å. The four Ni-Ni separations from Ni5 to Ni1-4 are indicative of metal-metal bonding and range from 2.540(2) to 2.590(2) Å. Common molecular Ni-Ni separations with metal-metal bonding are 2.327(10) – 2.985(2) Å.[144,148] However, the Ni5 atom which is already coordinated to five antimony atoms does not favor metal-metal bonding.

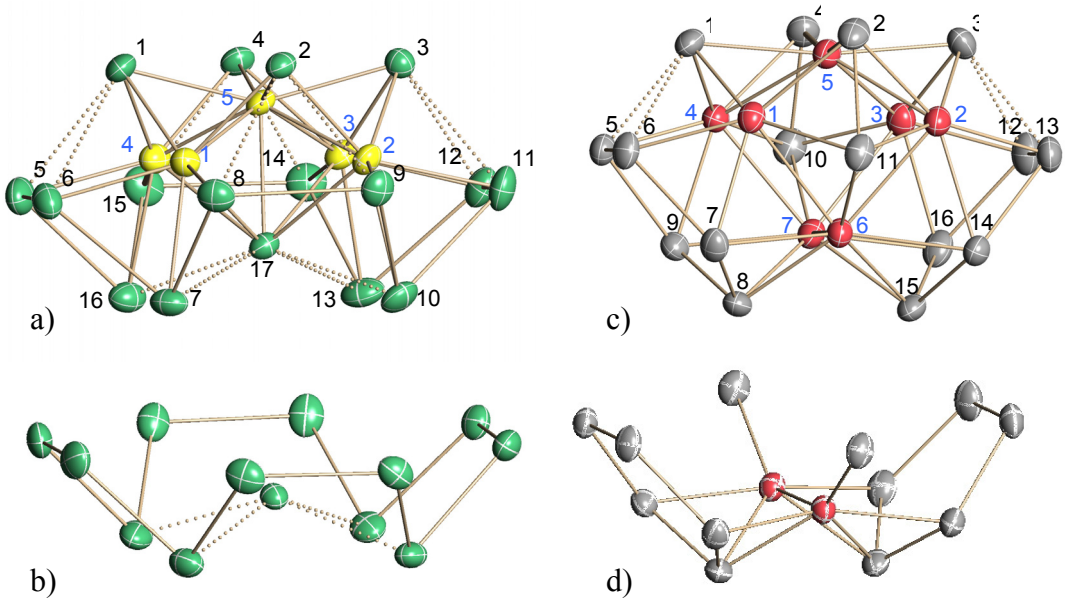

Figure 4. 3. a) ORTEP drawing of $[Ni_5Sb_{17}]^{4-}$. b) An ORTEP drawing of the Sb_{13} bowl of the $[Ni_5Sb_{17}]^{4-}$ structure. c) ORTEP drawing of $[Pd_7As_{16}]^{4-}$. d) An ORTEP drawing of the Pd_2As_{12} bowl of $[Pd_7As_{16}]^{4-}$. Red and yellow atoms represent the palladium and nickel atoms, respectively. The grey and green atoms represent arsenic and antimony atoms, respectively. Dotted lines indicate partial or "secondary" bonds. All thermal ellipsoids are at 50% probability.

Table 4. 4. Select bond distances (Å) and angles (°) for $[Ni_5Sb_{17}]^{-4}$.

Sb1-Sb5	3.135(3)	Ni4-Sb5	2.540(2)
Sb1-Sb6	3.152(2)	Ni4-Sb15	2.525(3)
Sb2-Sb8	3.150(5)	Ni4-Sb16	2.549(2)
Sb2-Sb9	3.095(2)	Ni4-Sb17	2.8206(15)
Sb3-Sb11	3.097(4)	Ni5-Sb1	2.590(2)
Sb3-Sb12	3.152(3)	Ni5-Sb2	2.613(3)
Sb4-Sb14	3.125(2)	Ni5-Sb3	2.592(2)
Sb4-Sb15	3.107(4)	Ni5-Sb4	2.604(3)
Sb5-Sb6	2.881(3)	Ni5-Sb17	2.5430(15)
Sb5-Sb16	2.823(3)	Ni5-Ni1	2.552(2)
Sb6-Sb7	2.833(2)	Ni5-Ni2	2.551(2)
Sb7-Sb8	2.816(4)	Ni5-Ni3	2.590(2)
Sb7-Sb17	3.1396(16)	Ni5-Ni4	2.540(2)
Sb8-Sb9	2.901(4)	Ni3-Sb3	2.5142(17)
Sb9-Sb10	2.856(2)	Ni3-Sb4	2.524(2)
Sb10-Sb11	2.842(5)	Ni3-Sb12	2.552(2)
Sb10-Sb17	3.1667(17)	Ni3-Sb13	2.553(3)
Sb11-Sb12	2.919(4)	Ni3-Sb14	2.5472(19)
Sb12-Sb13	2.851(4)	Ni3-Sb17	2.8445(16)
Sb13-Sb14	2.847(3)	Ni4-Sb1	2.503(2)
Sb13-Sb17	3.176(2)	Ni4-Sb4	2.510(2)
Sb14-Sb15	2.928(4)		
Sb15-Sb16	2.828(4)	Sb2-Ni1-Sb8	77.48(9)
Sb16-Sb17	3.1577(18)	Sb2-Ni1-Sb6	145.73(8)
Ni1-Sb1	2.5057(19)	Sb7-Ni1-Sb8	67.20(10)
Ni1-Sb2	2.496(3)	Ni5-Ni1-Sb7	127.54(6)
Ni1-Sb6	2.547(2)	Ni1-Ni5-Sb17	67.24(5)
Ni1-Sb7	2.5509(19)	Ni1-Ni5-Ni2	79.53(7)
Ni1-Sb8	2.537(5)	Ni1-Ni5-Ni3	134.55(7)

Ni1-Sb17	2.8213(15)	Sb5-Sb1-Sb6	54.55(5)
Ni2-Sb2	2.522(2)	Sb6-Sb7-Sb8	83.22(10)
Ni2-Sb3	2.5107(17)	Sb7-Sb8-Sb9	102.92(15)
Ni2-Sb9	2.541(2)	Sb1-Ni5-Sb17	105.40(8)
Ni2-Sb10	2.542(2)	Sb1-Ni5-Sb4	86.45(8)
Ni2-Sb11	2.527(4)	Sb1-Ni1-Sb2	89.41(6)
Ni2-Sb17	2.7825(16)	Sb1-Ni1-Sb6	77.20(6)

Complex **4.2** has twelve antimony – antimony bond distances (2.816(4) to 2.928(4) Å) which are in the range for the Sb-Sb bond lengths reported for $[(CO)_3Ni_3Sb_7]^{3-}$ and $[^tBu_3(cyclo\text{-}Sb_4)]_2$ (2.810(8) to 2.977(8) Å and 2.8411(6) to 2.8665(6) Å, respectively).[149,150] These contacts are longer than those in the metal-free Zintl ions (i.e. Sb_7^{3-}, Sb_{11}^{3-}) [35,151] and are more akin to typical organostibindes, such as $R_2Sb\text{-}SbR_2$ (2.826(4) to 2.866(1) Å)[152]. The twelve longer bond distances between the Sb1-4, 17 atoms and Sb5-16 atoms range from 3.095(2) to 3.176(2) Å. These longer separations suggest fractional Sb-Sb bonding similar to those exhibited by the Sb8 atoms of **4.1.**

$[Pd_7As_{16}]^{4-}$ The $[K(2,2,2\text{-crypt})]_8[Pd_7As_{16}]_2 \cdot 3.5en$ salt has triclinic crystal symmetry, space group P-1, with one solvate molecule sitting on the inversion center of the asymmetric unit cell. The unit cell contains two independent but virtually identical $[Pd_7As_{16}]^{4-}$ ions, **4.4**. These anions have virtual C_{2v} point symmetry and can be viewed as a distorted capped trigonal prismatic Pd_7 core surrounded by $2As_5$, $2As_2$, and 2As units (figure 4.3c). The crystal data are summarized in table 4.2 and selected bond distances and angles are given in table 4.5.

There are twelve typical[87,153,154] As-As σ-bonds in the $2As_5$ and $2As_2$ units of $[Pd_7As_{16}]^{4-}$ with bond distances in the range 2.410(1) to 2.495(1) Å. $[Pd_7As_{16}]^{4-}$ also has four longer As-As distances between the 2As and $2As_5$ units in the range 2.752(1) to 2.833(1) Å. The latter are reminiscent of the As-As contacts in the As_{20} dodecahedral cage of $[As@Ni_{12}@As_{20}]^{3-}$.

The seven palladium atoms are in three different bonding environments. The Pd7 atom caps the face of the Pd_6 trigonal prism and bonds to four arsenic atoms in a square planar environment. The four palladium atoms, Pd3-6, are virtually equivalent and make up the face of the trigonal prism. These atoms are each in a 5-coordinate geometry, $Pd(\eta^2\text{-}As_2)(\eta^1\text{-}As)(\eta^2\text{-}As_5)$. The remaining two palladium atoms, Pd1-2, are virtually equivalent and in a different 5-coordinate geometry, $Pd(\eta^1\text{-}As_2)(\eta^2\text{-}As_5)_2$. While this is the most effective way to describe $[Pd_7As_{16}]^{4-}$, it is also interesting to note that a unit isoelectronic to the [Ni(cyclo-Ni_4Sb_4)] lid in **4.2** resides in the $[Pd_7As_{16}]^{4-}$ cluster. These metal centered 8-member rings resemble the ME_8^{n-} complexes.[44,50]

In the ME_8^{n-} series of compounds, all atoms in the E_8 ring are equidistant from the centered transition-metal inside the ring. The E_8 ring expands and contracts in an accordion-like fashion depending on the size of the centered transition-metal. It is interesting to compare these aspects of the ME_8^{n-} series to the [M(cyco-M_4E_4)] units found in clusters **4.2** and **4.4** (figure 4.4). The Ni5 atom in the [M(cyclo-M_4E_4)] unit

Table 4. 5. Select bond distances (Å) and angles (°) for $[Pd_7As_{16}]^{4-}$.

As1-As5	2.8145(14)	Pd1-Pd6	2.8213(10)
As1-As6	2.8326(15)	Pd2-Pd5	2.8434(9)
As2-As11	2.4210(15)	Pd2-Pd6	2.8242(10)
As3-As12	2.7940(14)	Pd3-Pd5	2.8292(10)
As3-As13	2.7521(13)	Pd3-Pd7	2.8516(10)
As4-As10	2.4298(15)	Pd4-Pd5	2.8394(9)
As5-As6	2.4407(14)	Pd4-Pd7	2.7999(9)
As5-As9	2.4747(14)	Pd6-Pd7	2.8768(9)
As6-As7	2.4883(15)		
As7-As8	2.4185(14)	As5-As1-As6	51.21(3)
As8-As9	2.4235(13)	As6-As5-As9	106.99(5)
As12-As13	2.4392(13)	As5-As6-As7	108.40(5)
As12-As16	2.4815(14)	As6-As7-As8	107.05(5)
As13-As14	2.4948(13)	As7-As8-As9	109.30(5)
As14-As15	2.4114(13)	As8-As9-As5	108.22(5)
As15-As16	2.4099(13)	As11-As2-Pd5	106.81(5)
Pd1-As1	2.5013(12)	Pd1-As11-Pd2	90.86(4)
Pd1-As2	2.4985(12)	As2-As11-Pd6	102.47(4)
Pd1-As6	2.4433(11)	As2-Pd1-As1	90.93(4)
Pd1-As7	2.5416(13)	As6-Pd1-As2	153.20(5)
Pd1-As11	2.5082(11)	As6-Pd1-As7	59.85(4)
Pd5-As1	2.5984(11)	As11-Pd1-As2	57.83(4)
Pd5-As2	2.5107(11)	As4-Pd5-As2	161.70(5)
Pd5-As3	2.6343(10)	As2-Pd5-As1	88.45(4)
Pd5-As4	2.5485(11)	As7-Pd6-As11	85.03(4)
Pd6-As7	2.6043(11)	Pd1-Pd5-Pd4	62.57(3)
Pd6-As8	2.5857(11)	Pd2-Pd5-Pd1	76.89(2)
Pd6-As11	2.6176(12)	Pd1-Pd6-Pd2	78.28(3)
Pd1-Pd5	2.8876(10)	Pd1-Pd6-Pd7	97.55(3)

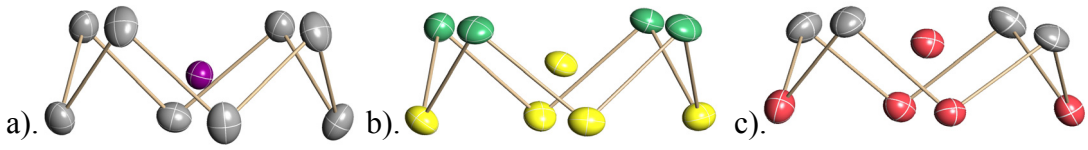

Figure 4. 4. Purple, red and yellow atoms represent the chromium, palladium and nickel atoms, respectively. The grey and green atoms represent arsenic and antimony atoms, respectively. Bonds from the centered atoms to the eight-member rings have been omitted for clarity. a). An ORTEP drawing of a ME_8^{n-} ion, $[CrAs_8]^{2-}$. b). The Ni(cyclo-Ni_4Sb_4) lid of $[Ni_5Sb_{17}]^{4-}$. c). The Pd(cyclo-Pd_4As_4) lid of $[Pd_7As_{16}]^{4-}$. All thermal ellipsoids are at 50% probability.

of $[Ni_5Sb_{17}]^{4-}$ sits slightly closer to the other Ni ions (avg. 2.56 ± 0.02 Å) than the Sb atoms (avg. 2.59 ± 0.03 Å). In the [cyclo-Ni_4Sb_4] ring, the Ni-Sb-Ni bond angles are 83.1 ± 1.4°$_{avg}$ and the Sb-M-Sb bond angles are 89.9 ± 0.5°$_{avg}$. However, in comparison, the Pd5 atom, in the [M(cyclo-M_4Sb_4)] unit of $[Pd_7As_{16}]^{4-}$, is shifted further from the center of the ring away from the Pd1-4 atoms. This places the Pd5 atom closer to the As1-4 atoms (avg. 2.57 ± 0.05 Å) than the Pd1-4 atoms (avg. 2.85 ± 0.03 Å). Expansion of the bond angles (93.5 ± 3.2°$_{avg}$ and 92.8 ± 1.8°$_{avg}$, Pd-As-Pd and As-Pd-As, respectively) in the [cyclo-Pd_4As_4] ring in comparison to the [cyclo-Ni_4Sb_4] ring of **4.2**, accommodates the larger transition-metal, Pd. As a result of the differences in bond distances, the Pd5 atom sits more to the top of the 8-member ring near the arsenic atoms. The Pd5-Pd1-4 distances fall in the longer end of similar Pd-Pd bonding separations (2.597(4) to 2.960(4) Å).[155-157]

4.2.3 Mass Spectrometry

$[Pd_7As_{16}]^{4-}$ The electrospray ionization mass spectra were recorded in the negative ion mode from dmf solutions of the complex **4.4**. One sample solution has a mass envelope at 1982.1, $[KPd_7As_{16}]^{4-}$, (figure 4.5c-d). The ESI mass spectra of a second sample which had the co-crystallized complexes **4.3** and **4.4** had a peak at 1947 m/z with a mass envelope that matches the ion anion, $[H_3Pd_7As_{16}]^{1-}$.

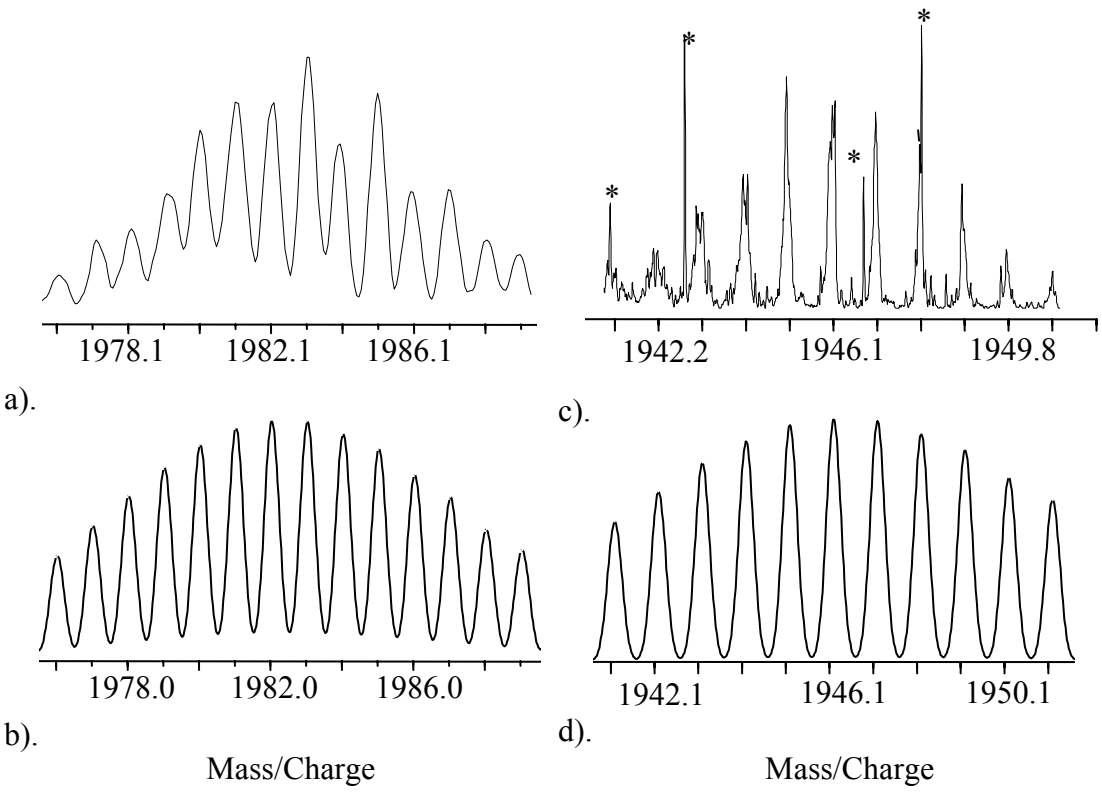

Figure 4. 5. Electrospray ionization mass spectra of the complex **4.4** in dmf solutions as the ions $[KPd_7P_{16}]^{1-}$ (a) and $[H_3Pd_7As_{16}]^{1-}$ (c), respectively. Simulated isotopic patterns of both anions are displayed in (b) and (d), respectively.

4.2.4 Structural Relationship

When both of the Ni2 positions in **4.2** are fully occupied, the molecular formula of **4.1** becomes $[Ni_4Sb_{16}]^{4-}$ and is very similar to $[Ni_5Sb_{17}]^{4-}$, **4.**2. The only differences between the anions are that $[Ni_5Sb_{17}]^{4-}$ has an additional Ni and Sb atom. Interestly, a structural relationship between $[Ni_4Sb_{16}]^{4-}$ and $[Ni_5Sb_{17}]^{4-}$ can be seen, see scheme 1. This relationship can be viewed by first breaking the following bonds: Sb8-Sb6, Sb6-Sb5, Sb3-Sb2, Sb8'-Sb5, and their dimer equivalent bonds and forming new Sb6-Sb2, Sb3-Sb5, Sb6'-Sb2', Sb3'-Sb5' bonds. The structure of each Sb_7 unit now has two parallel Sb_3 rings bridged by an Sb1 atom and Sb8 atoms bridge the two Sb_7 units. Structural rearrangement of this structure results in the main framework of $[Ni_5Sb_{17}]^{4-}$. Rotation at the Sb1, 1', 8 and 8' atoms forces the positions of the three-member rings to change. If this rearrangement of the antimony units occurs, it would be expected that some Ni-Sb and all Ni-Ni bonds would break placing the Ni atoms in new bonding environments. This would disperse the nickel atoms more throughout the structure creating an empty cavity in the center of the cluster. The Ni5 and Sb17 fill the hole stabilizing the new cluster anion, $[Ni_5Sb_{17}]^{4-}$.

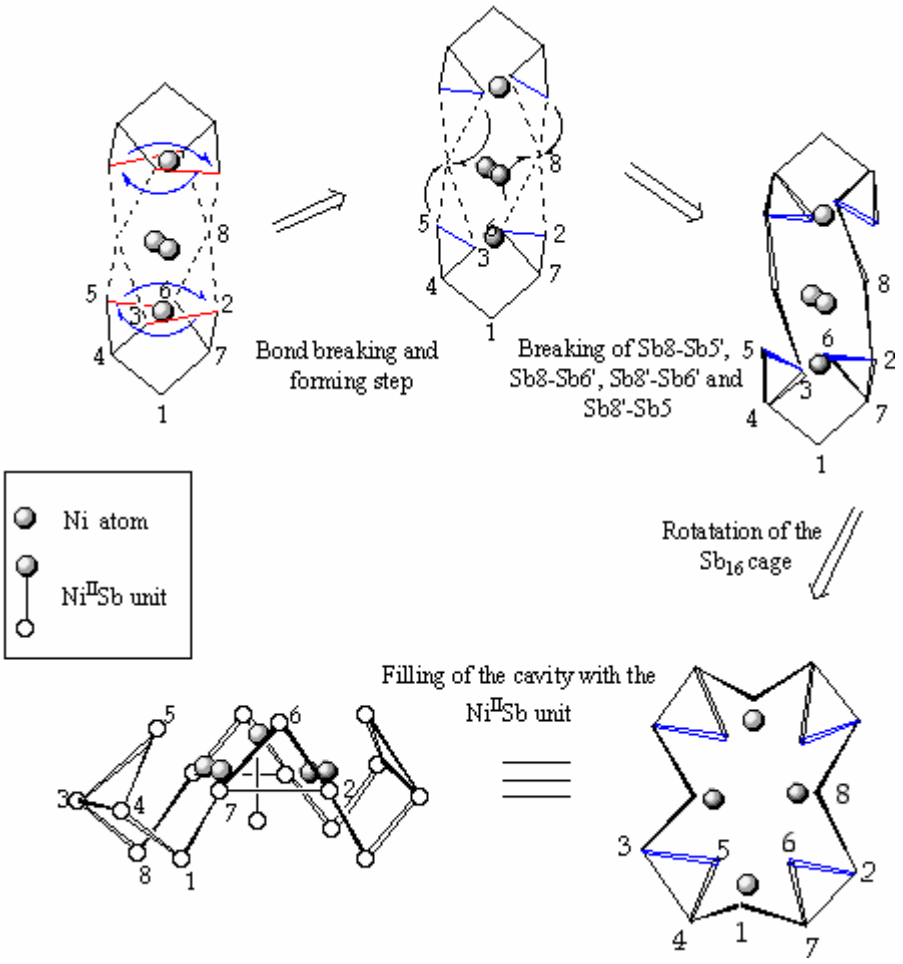

Scheme 4. 1

4.3 Bonding Analysis and Discussion

The Zintl-Klemm formalism is typically employed to aid in the description of free Zintl anions, as well as when they are coupled to transition-metal fragments. The original Zintl concept was based on the 8-N rule and enhanced by Klemm's psuedoelement model. The resulting formalism strives to compare the main group atoms of the anionic units to known isoelectronic neutral elements. Therefore

assigning charge distribution to the free Zintl anions E_7^{3-} (E = P, As, and Sb) which are isoelectronic to the neutral nortricyclic C_7H_{10} cluster is straightforward (CH ≅ E and $CH_2 \cong E^-$).

Naked main group polyanions are seen throughout the literature to follow the Zintl-Klemm formalism. This formalism has also been effective in explaining charge distribution and bond order in Zintl anion / transition-metal complexes. However, the anions discussed here have novel and complicated structures, and applying the Zintl-Klemm formalism to the complexes reported here to explain their charge distribution is not straightforward. Assignment of charge in these anions, $[Ni_2Sb_{16}]^{4-}$, $[Ni_5Sb_{17}]^{4-}$, and $[Pd_7As_{16}]^{4-}$, following the Zintl-Klemm formalism was difficult due to the continuum of Sb-Sb bond distances and to a smaller extent for As-As bonds. The most stable forms of metallic pnictogen elements (As, Sb, Bi) have three nearest neighbors that form a puckered sheet of covalently bonded atoms and three further neighbors which are part of the adjacent sheet. Comparing interactions between adjacent layers and covalent bond distances within a sheet of the elemental metals, a large separation between the two cannot be seen for the heavier elements.[115] The decrease in distance between the 3 intra-layer and 3 inter-layer creates the continuum of E-E bond distances making a true single bond cut-off value unclear.

According to the Zintl-Klemm formalism, each antimony atom desires three two-centered two-electron bonds to satisfy the octet rule. If the antimony atom forms fewer than three bonds or more than three, the formal charge associated with the atom decreases or increases, respectively, from a formal charge of zero. Antimony-antimony single bonds have been reported in the literature to be as long as 2.977Å[149],

but α-Sb has inter-layer interactions of 3.355Å.[115] The previously discussed formalism does not take in to account the bond distances within this range which are two long to make two-centered two-electron bonds but still retain some bonding character, from secondary or partial bonds.[158,159] It also becomes difficult to assign cut-off values between single and double bonds with a large continuous range of Sb-Sb separations. Both **4.1** and **4.2** have Sb-Sb bond distances that are in this partial bonding range, while **4.4** has a four As-As distances that have questionable degrees of bonding. The Zintl-Klemm formalism requires definitive single bond ranges making it difficult to apply to these heavier main group complexes.

The bond valence formalism presents a model for calculating the formal charges of each main group atom based on the covalent homonuclear bonds of the polyanion. To use this formalism with transition-metal main-group clusters, one must assume complete charge transfer from transition-metal to polyanion (an ionic limit). Therefore, the oxidation states of the transition-metal fragments are assigned through charge balance with the net formal charge of the polyanion. In reality, the ionic nature of the transition-metal - main group polyanion interaction becomes more covalent as the electronegativity of the homonuclear main group atoms decreases. Therefore, oxidation states assigned to transition-metals of lighter pnictogen cluster are more closely related to the actual charge than those assigned to transition-metals in heavier pnictogen clusters. This straddling of both ionic and covalent formalisms is an inherent limitation of this model. However, the bond valence formalism is a useful first-order analysis of bond order and formal charge of the main group atoms in

transition-metal / Zintl ion complexes. Unlike the Zintl-Klemm formalism, this model can be used for all pnictogen homonuclear clusters.

DFT calculations differ from the Zintl-Klemm and bond valence formalisms by taking into account transition-metal bonds to the polyanions. Since the **4.1** and **4.2** clusters have heavier pnictogen atoms, complete charge transfer from the transition-metals to the pnictogen atoms is unlikely to occur due to the similar electronegativities between the antimony and nickel. Therefore, bond orders and formal charges calculated by the more tedious DFT calculations are presented for comparison. When covalent interactions are taken into account, as in DFT calculations, delocalization of charge can be considered when calculating charge distribution. Since bond valence analyses assume no charge transfer from the transition-metals to the pnictogen atoms and DFT analyses do, quantitative comparison of charges assigned by the bond valence and DFT analyses should not be the same, but trends in distribution can be related. Comparison of bond orders calculated from only E-E bonds should not alter significantly between the bond valence formalism and DFT calculations. The results of DFT and bond valence analyses of the Zintl anion / transition-metal complexes, **4.1**, **4.2**, and **4.4**, are presented for comparison in tables 4.6-4.8.

[Bond Valence Formalism] Calculating the total formal charge on the anion, assessed by the bond valence formalism, was accomplished in steps. First, the total bond order of every antimony atom in the cluster must be individually calculated, using eq. 4.1:

$$vij = \exp[(R\text{-}dij)/0.37] \qquad 4.1$$

where *vij* is the bond order of the antimony-antimony bond in question, R (Å) is the bond valence parameter, *dij* is the bond distance (Å) and b = 0.37 Å.[137] Then, the sum of all the *vij* values for an individual atom gives the total bond order for that atom. The Zintl-Klemm concept requires that a naked antimony atom has a 3- formal charge, according to the 8-N rule. Generally, bond strengths are directly related to the bond distances and are represented by the total bond order calculated using eq. 4.1. Therefore, the sum of the total bond order of an atom and -3 gives the formal charge associated with the atom according to this formalism. The sum of the formal charges of all the antimony atoms, which were calculated through this process, equals the total formal charge on the polyanion. [137] The sum of the total formal charge on the polyanion and the oxidation states of the transition-metal atoms equals the total charge on the entire anion.

This formalism is only being used to consider the effect the Sb-Sb interactions have on each antimony atom's bond order and formal charge and does not take into account the Ni-Sb interactions. The initial R-value used by O'Keeffe and Brese for Sb-Sb was 2.82 Å.[137] Jeitschko observed that the type of cation an antimony polyanion has effects the Sb- Sb bond length requiring an optimized R-value for rare earth Zintl antimonide phases (2.80 Å).[136] The anions discussed in this paper are alkali crypt salts requiring a different optimized R-value. The R-value best fit for transition-metal / polyantimonides of alkali crypt salts was determined to be 2.83 Å. An average of Sb-Sb interactions seen in alkali crypt salts was calculated from naked

Zintl antiminides and other transition-metal Zintl antimonide complexes. However, due to the wide Sb-Sb bond continuum an appropriate cut-off of Sb-Sb interactions to include was difficult. Therefore, a variety of R-values between the value proposed by O'Keeffe and Brese and the average that was calculated for alkali crypt salts were used to calculate charge distribution on a few complexes. The R-value, 2.83 Å, made the most chemical sense for these antimonide clusters. A similar process was used to determine the R-value to use for transition-metal / Zintl arsenides anions of alkali crypt salts, R = 2.42 Å.

$[Pd_2(As_7)_2]^{4-}$ and $[(CO)_3CrSb_7]^{3-}$ To illustrate the short comings of the Zintl-Klemm formalism and the usefulness of a bond valence analysis, the charge distribution of the related clusters $[Pd_2(As_7)_2]^{4-}$, **4.3**, and $[(CO)_3CrSb_7]^{3-}$, **4.6**[18], were studied. Both clusters have E_7 cages that structurally resemble the hydrocarbon clusters norbornadiene, C_7H_8, and norbornane, C_7H_{12}. If the E_7 cages of **4.3** and **4.6** are isoelectronic to norbornadiene, they will have 1- total charges. On the other hand, if the cages are isoelectronic to norbornane, instead they will have 5- total charges. Both possible Zintl-Klemm descriptios are shown for $[(CO)_3CrSb_7]^{3-}$ in scheme 4.2 but bond continua make it difficult to distinguish which description is appropriate.

Bond valence analyses of the two clusters give net charges of -4.78 and -1.78 for the As_7 and Sb_7 cages, respectively. These analyses are suggestive of norbornane-like As_7^{5-} cages in $[Pd_2(As_7)_2]^{4-}$ and a norbornadiene-like Sb_7^{1-} cage in $[(CO)_3CrSb_7]^{3-}$ when forcing these clusters into the allowed Zintl-Klemm description depicted in scheme 4.2. Assignment of the Sb_7^{1-} Zintl-Klemm description to $[(CO)_3CrSb_7]^{3-}$ is

further supported by spectroscopy studies done by Charles et. al. While the DFT analysis on **4.6** gives a -2.1 net charge on the Sb_7 similar to the bond valence results,

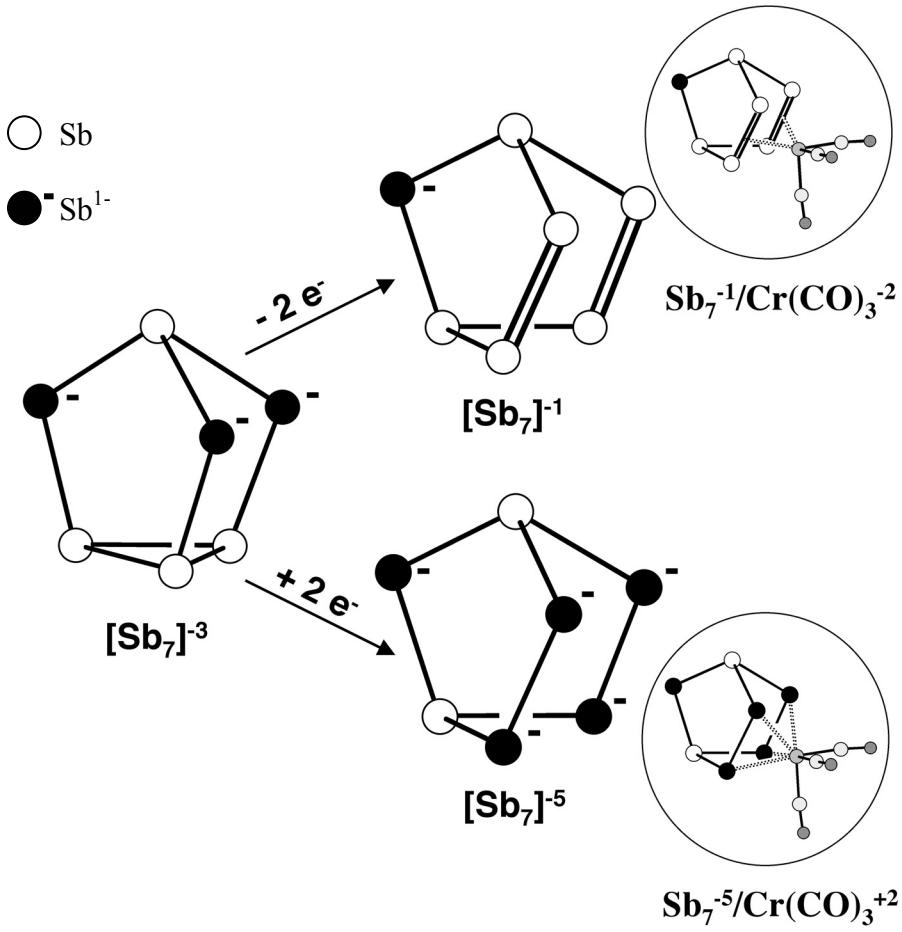

Scheme 4. 2

the DFT net charge calculated for **4.4** is lower (-2.5) than its bond valence counterpart. This discrepancy suggests a stronger covalent character between the As_7 cages and the Pd_2 dimer in **4.3** than is present in **4.6** between the Sb_7 cage and the $Cr(CO)_3$ fragment. The DFT analysis favors the As_7^{1-} Zintl-Klemm description for $[Pd_2(As_7)_2]^{4-}$; however, if this description is applied, the Pd atoms must each be -1

oxidation states. The As_7^{5-} Zintl-Klemm description to $[Pd_2(As_7)_2]^{4-}$ puts the Pd atoms in +3 oxidation states, which is a more favorable oxidation state for palladium.

$[Ni_{2+x}Sb_{16}]^{4-}$ Previously reported transition-metal / Zintl ion complexes contained main group units that had isoelectronic analogies, so that charge distribution could be assigned according to the Zintl-Klemm formalism. Zintl ion dimers, in the literature, are comprised of known polyatomic units joined by a

Table 4. 6. Results of DFT and bond valence calculations on $[Ni_2Sb_{16}]^{4-}$.

	Bond Order			Formal Charge		
Atom	**BVF**	**DFT**	**Δ**	**BVF**	**DFT**	**Δ**
Sb8	2.079	2.02	0.06	-0.921	-0.1631	-0.757
Sb1	2.449	2.24	0.21	-0.551	-0.7109	0.161
Sb2	2.521	2.50	0.02	-0.479	-0.2696	-0.210
Sb3	2.564	2.45	0.11	-0.436	-0.2682	-0.169
Sb5	2.591	2.50	0.09	-0.409	-0.2691	-0.142
Sb6	2.615	2.45	0.17	-0.385	-0.2689	-0.115
Sb7	3.004	2.76	0.24	0.004	-0.1839	0.189
Sb4	3.013	2.76	0.25	0.013	-0.1839	0.196

bond or by a bridging metal.[153,160] $[Ni_2Sb_{16}]^{4-}$ is the first Zintl ion dimer to connect the polyatomic units with extra homonuclear atoms creating a Sb_{16} polyanion that is unprecedented for all main group homonuclear clusters. While the Sb_{16} unit has no isoelectronic analog, breaking up the anion into two Sb_7 units bridged by a [cyclo-(Ni_2Sb_2)] unit, creates pieces with known isoelectronic or isostructural analogs, as was discussed in the solid state section of this chapter.

The formal charge on the Sb_7 units and the Sb8 atoms of **4.1** according to the bond valence analysis are -2.243 and -0.921, respectively, which more closely resembles a $2[Sb_7]^{1-}$ / $[Ni_2Sb_2]^{2-}$ Zintl-Klemm description similar to the $[Sb_7]^{1-}$ / $[(CO)_3Cr]^{2-}$ description assigned to $[(CO)_3CrSb_7]^{3-}$. The advantage of the bond valence formalism over the Zintl-Klemm formalism is that it can address issues that arise from bond continua. The longer Sb-Sb bonds made by the Sb8 atoms linking the Sb_7 cages suggested partial bonding. The bond valence analysis supports this by placing a total bond order of 2.079 on each Sb8 atom, which have four long Sb-Sb contacts. This value corresponds almost exactly with the 2.02 bond order determined by the DFT analysis. A bond order of ~2 indicates that according to both types of empirical calculations, partial bonding occurs between the Sb8 atoms of the [cyclo-(Ni_2Sb_2)] unit and the Sb_7 cages of **4.1**. The distribution of the total negative charge over $[Ni_2Sb_{16}]^{4-}$, according to bond valence and DFT analyses are given in table 4.6.

While viewing $[(Ni_2Sb_2)(Sb_7)_2]^{4-}$ as three units, two Sb_7 cages and the [cyclo-(Ni_2Sb_2)] ring, avoids the isoelectronic analog problem encountered by the Sb_{16} description. The σ- or π- character of the E2-E3 and E5-E6 bonds in **4.1** dictate whether the E_7 cages resemble norbornadiene or norbornane. A norbornadiene-like pnictogen cage has a –1 formal charge due to π-bonding, while norbornane-like pnictogen cages have only σ-bonds giving them a –5 formal charge. The Zintl-Klemm formalism can be used to derive these limiting charge assignments but cannot determine where a structure falls between the limits as was the case for the E_7 cages in $[Pd_2(As_7)_2]^{4-}$ and $[(CO)_3CrSb_7]^{3-}$. When the bond valence parameter, R, is viewed as a typical E-E (E = As, Sb) single bond, the different formal charges on the E_7 units

can be understood qualitatively.[161] The E2-E3 and E5-E6 bonds of $[Pd_2As_{14}]^{4-}$ are with in ca. 0.01 Å of the optimized R-value for alkali 2,2,2-crypt arsenides; therefore, they are almost ideal σ-bonds in norbornane-like As_7^{5-} cages which was supported by its bond valence analysis . The analogous bonds in $[(Ni_2Sb_2)(Sb_7)_2]^{4-}$ are ca. 0.04 Å and 0.07 Å shorter than the optimized R-value for alkali (2,2,2-crypt) stabinides. This larger deviation from the optimized R-value suggests that these bonds have some π-character giving the Sb_7 cages more norbornadiene-like structures than norbornane-like structures. These bonds (2.7922(6) and 2.7614(6)Å, respectively) are near the upper end of reported Sb=Sb bonds (2.663(3) – 2.774(1)Å),[35,162-166] which in not surprising since its common for double bonds to lengthen when coordinated to transition-metals. DFT and bond valence analysis on the Sb_7 cages of $[Ni_2Sb_{16}]^{4-}$ give similar results (-2.15 and -2.24, respectively) favoring the Sb_7^{1-} Zintl-Klemm description.

The net formal charges calculated by both the bond valence formalism and DFT methods for the Sb_7 units of **4.1** are in good agreement being 2.00 ± 0.24. However, the bond valence formalism assigns a significantly more negative formal charge to the two Sb8 atoms than the DFT calculations (-0.92 and -0.10, respectively). Therefore, the method also gave different charges to the Ni1 atoms (+1.2 and +0.3). This is presumably an artifact of the more covalent interactions allowed by the DFT analysis between the Sb8 and Ni1 atoms. The covalent character would delocalize the high negative charge assigned to the Sb8 atoms by the bond valence formalism, explaining the difference in formal charges assigned by the two methods.

It is also interesting to add that when the Sb_7 cages are viewed as 4-electron donor ligands, the [cyclo-$(Ni_2Sb_2)L_4]^{2-}$ subunit has 36 valence electrons even though the metric parameters of [cyclo-$(Ni_2Sb_2)]^{2-}$ are similar to $Ni_2(\mu\text{-}SbMe_2)_2(CO)_4$, **4.5**, a 34-electron complex Ni(I) dimer with Ni-Ni bonding. The two extra electrons of the [cyclo-$(Ni_2Sb_2)L_4]^{2-}$ result in 18 electron Ni atoms and no Ni-Ni bond. DFT analyses support this difference assigning a higher Ni-Ni bond order in $Ni_2(\mu\text{-}Sb\text{-}t\text{-}Bu)_2(CO)_4$, **4.5**, than $[(Ni_2Sb_2)(Sb_7)_2]^{4-}$ despite the similar Ni-Ni bond distances.

There are two different electronic descriptions for the 36-electron Ni dimer. In one description, there are two d_8-Ni(II) and two Sb^{3-} atoms and formal ligand to metal π-bonding from each bridging Sb8 atom. Alternatively, there are two Ni(0) and two Sb^{1-} atoms and formal metal to ligand π-bonding. The similar electronegativities of Ni (1.8) and Sb (1.9) make both descriptions viable.

$[Pd_7As_{16}]^{4-}$. If the Zintl-Klemm formalism is used to assign charge distribution to $[Pd_7As_{16}]^{4-}$, **4.4**, it would view the arsenic units as $2As_5^{-1}$, $2As_2^{2-}$, and $2As^{3-}$ putting the capping palladium atom as Pd(II) with the remaining palladiums as Pd(I).[95] The bond valence analysis distributes the negative charge over the arsenic atoms as $2As_5^{5-}$, $2As_2^{4-}$, and $2As^{2-}$. The total formal charges assigned to the seven palladium atoms must be +18 to give the anion its crystallographic –4 charge. The square planar environment of Pd7, capping the trigonal prism, suggests it has a +2 formal charge. The remaining six palladium atoms are in two different bonding environments, making up a mixed valence Pd_6^{+14} core.

The different formal charges on the palladium atoms are dependent on which charge distribution description is used. The Zintl-Klemm charge assignments to the

arsenic units are valid having neutral isoelectronic analogs, but they do not accurately represent the units of this complex. For example, the As-As bond distances of the As_2 and As_5 units are typical of As-As single bonds not the double bonds (~2.3 Å)[167-169] needed for the Zintl-Klemm description in which the units have –2 and –1 formal charges, respectively. Therefore, when As-As distances for single and double bonds are related to the As-As bond distances in the complex, the high formal charges the bond valence formalism assigns to the units, As_2^{4-} and As_5^{5-}, makes sense. It is also important to note that cyclopentane has the appropriate formula C_5H_{10} to compare to As_5^{5-} but it never has a planar arrangement like the As_5^{5-} rings in $[Pd_7As_{16}]^{4-}$. The lower formal charges assigned to the As^{2-} units are a result of their partial bonding to As_5^{5-} units. The separations between the As and As_5 units (2.7521(13) – 2.8326(15) Å) are larger than typical bonding arsenic separations but shorter than non-bonding distance.

Table 4. 7. Results of DFT and bond valence calculations on $[Pd_7As_{16}]^{-4}$.

	Bond Order			Formal Charge		
Atom	**BVF**	**DFT**	**Δ**	**BVF**	**DFT**	**Δ**
As1	0.679	1.64	-0.96	-2.321	-0.6073	-1.714
As3	0.830	1.64	-0.81	-2.170	-0.6080	-1.562
As2	1.000	1.69	-0.69	-2.000	-0.7359	-1.264
As4	1.025	1.69	-0.67	-1.975	-0.7328	-1.242
As10	1.029	1.75	-0.72	-1.971	-0.6400	-1.331
As11	1.127	1.75	-0.62	-1.873	-0.6361	-1.237
As16	1.877	2.38	-0.50	-1.123	-0.4980	-0.625
As7	1.887	2.39	-0.50	-1.113	-0.4980	-0.615
As14	1.923	2.39	-0.47	-1.077	-0.4972	-0.580
As9	1.930	2.39	-0.46	-1.070	-0.4974	-0.573
As8	2.085	2.37	-0.29	-0.915	-0.3950	-0.520
As6	2.105	2.48	-0.38	-0.895	-0.4394	-0.456
As15	2.139	2.37	-0.23	-0.861	-0.3958	-0.465
As12	2.165	2.47	-0.31	-0.835	-0.4376	-0.397
As5	2.170	2.48	-0.31	-0.830	-0.4385	-0.392
As13	2.185	2.48	-0.30	-0.815	-0.4384	-0.377

The DFT analysis gives bond orders and charge distributions per As atom that follow the same general trend as seen for the bond valence assignments. However, the actual values are significantly lower than the differences observed for $[(Ni_2Sb_2)(Sb_7)_2]^{4-}$. The largest discrepancies were seen for arsenic atoms within bonding distance to a large number of nickel atoms, suggesting that $[Pd_7As_{16}]^{4-}$ has more covalent character between the arsenic framework and the palladium atoms than

is typical of binary anions isolated from a Zintl ion precursor. Both the bond valence and DFT analyses indicate less charge transfer than is typically seen in traditional coordination complexes.

$[Ni_5Sb_{17}]^{4-}$ While the Zintl-Klemm formalism at first glance appeared to work for the arsenic units in **4.4**, upon further analysis it was inadequate. The Zintl-Klemm formalism is not even a remotely applicable method for distributing charge in $[Ni_5Sb_{17}]^{4-}$. The Sb_{17} polyatomic cluster in this anion has no known isoelectronic analog which is necessary to apply the Zintl-Klemm formalism. The long antimony-antimony bonds, between Sb1-4 and 17 and the rest of the Sb_{17} cage, suggest partial bonding. Bond orders derived from the bond valence formalism and DFT calculations both support partial bonding between these atoms giving the Sb17 atom a bond order of 1.63 and 1.02, respectively. The environment of Sb17 is similar to that seen for the Sb8 atoms of **1**. Therefore, it is not surprising to find the largest DFT vs. bond valence formalism discrepancy between the formal charge assignments for this atom, table 4.8. Attempts to apply the Zintl-Klemm formalism to Sb_{13} by ignoring these partial bonds is not possible.

Table 4. 8. Results of DFT and bond valence calculations on $[Ni_5Sb_{17}]^{4-}$.

	Bond Order			Formal Charge		
Atom	**BVF**	**DFT**	**Δ**	**BVF**	**DFT**	**Δ**
Sb1	1.148	1.54	-0.39	-1.852	-0.1726	-1.679
Sb3	1.181	1.50	-0.32	-1.819	-0.1873	-1.632
Sb4	1.187	1.49	-0.30	-1.813	-0.1888	-1.624
Sb2	1.201	1.52	-0.32	-1.799	-0.1750	-1.624
Sb17	1.630	1.02	0.61	-1.370	0.6441	-2.014
Sb12	2.152	2.26	-0.11	-0.848	-0.2569	-0.591
Sb14	2.154	2.26	-0.11	-0.846	-0.2536	-0.592
Sb9	2.232	2.25	-0.02	-0.768	-0.2502	-0.518
Sb15	2.232	2.27	-0.04	-0.768	-0.2517	-0.516
Sb11	2.239	2.26	-0.02	-0.761	-0.2547	-0.506
Sb8	2.276	2.26	0.02	-0.724	-0.2496	-0.474
Sb13	2.282	1.93	0.35	-0.718	-0.3725	-0.346
Sb10	2.294	1.93	0.36	-0.706	-0.3695	-0.337
Sb6	2.295	2.25	0.05	-0.705	-0.2524	-0.453
Sb5	2.334	2.25	0.08	-0.666	-0.2544	-0.412
Sb16	2.437	1.93	0.51	-0.563	-0.3703	-0.193
Sb7	2.460	1.93	0.53	-0.540	-0.3657	-0.174

The total formal charge calculated by the bond valence analysis for the Sb_{17} cluster (figure 4.3a) is –19.68. Knowing the formal charge of the entire anion (-4) and that contributed by the antimony cluster possible formal charges on the nickel atoms can be assigned. The total formal charge of all five nickel ions should equal +15.68. The square pyramidal environment of Ni5 suggests that it is in a +2

oxidation state. The remaining +13.68 formal charge must be distributed equivalently between symmetry equivalent Ni1-4. The +3.42 formal charge assigned in this manner to each of the four remaining nickels is approximately +3 suggesting that these four remaining nickel atoms are Ni(III) ions.

Unlike **4.1** and **4.4**, bond orders and charge distributions calculated by bond valence and DFT analyses do not show similar trends throughout **4.2**. DFT analysis gives a total net charge of -3.58 on the Sb_{17} cluster of $[Ni_5Sb_{17}]^{4-}$. This scenario suggests no charge transfer from the Ni atoms to the Sb_{17} cage.

4.4 Conclusion

$[(Ni_2Sb_2)(Sb_7)_2]^{4-}$, $[Ni_5Sb_{17}]^{4-}$ and $[Pd_7As_{16}]^{4-}$ join the growing class of ligand-free binary anions and contain a variety of novel pnictogen polyatomic anion units. While a Zintl-Klemm type description was achieved for $[(Ni_2Sb_2)(Sb_7)_2]^{4-}$ with the aid of the bond valence formalism, it proved more difficult to force $[Ni_5Sb_{17}]^{4-}$ and $[Pd_7As_{16}]^{4-}$ into a Zintl-Klemm description. A Zintl-Klemm description assumes complete electron transfer from the transition-metals to the more electronegative main group atoms. Covalency documented by the DFT analyses on **4.2** and **4.4** exemplify why it is difficult to use the Zintl-Klemm formalism to force an ionic description on to these clusters. However, the assumed ionic nature embedded in the bond valence formalism allows it to extract Zintl ion pieces within a large cluster as was seen for **4.1** more successfully than the covalent DFT analysis. Its ability to aid the Zintl-Klemm formalism and its simplicity make the bond valence formalism a useful tool for analyzing Zintl clusters.

The anionic clusters presented here have larger metal centers but are not discrete pieces of bulk metallic lattices, and their arrangement with the arsenic and antimony atoms do not resemble pieces of binary phases. This observation suggests that all of the clusters presented are more molecular in nature and have not crossed the Zintl-Klemm border. However, the results of the bond valence and DFT analyses indicate delocalized bonding, partial bonding, and non-integral oxidation states, which are more common in solid-state intermetallics than molecular clusters. The contradiction on which side of the "Zintl-Klemm border" these clusters reside suggests that $[(Ni_2Sb_2)(Sb_7)_2]^{4-}$, $[Ni_5Sb_{17}]^{4-}$ and $[Pd_7As_{16}]^{4-}$ are an interesting group of clusters that reside on the border having both intermetallic and molecular character.

4.5 Experimental Section

4.4.1 General Data

All reactions were carried out in a nitrogen atmosphere dry box (Vacuum Atmosphere Co). Electrospray Mass spectra were obtained by direct injection of dmf solutions into a Finnigan mass spectrometer. Samples were detected in the negative ion mode after being ionized by an ESI probe. An AMRAY 1820K scanning electron microscope with a potential of 20 kV was used for energy dispersive X-ray (EDX) studies.

4.4.3 DFT Calclulations

The program package PRIRODA[170,171] was used for all DFT[172] calculations, specifically functional PBE. [173] Relativistic Stevens-Bausch-Krauss (SBK) effective core potentials (ECP) [174-176] optimized for DFT-calculations were used in PBE calculations. The basis set was 311-split for main group elements with an additional p-function for hydrogen and two polarization d-functions for elements of higher periods. Coordinates used for bond order and charge calculations were first optimized by the PRIRODA program without constraints on symmetry. A multiplicity of 1 was used for **4.1** and **4.3**, while **4.2** required a multiplicity of 4 for convergence to occur.

Cartesian coordinates for the $[(Sb_7)_2Ni_{0.1}(Ni_2Sb_2)]^{4-}$ cluster, determined by X-ray diffraction, were first optimized by the PRIRODA program. The partially occupied Ni2 atoms were eliminated from the optimized coordinates and the program was used again to optimize the resulting coordinates. After this optimization, the resulting coordinates were used to calculate bond order and charge. DFT symmetry optimization calculations on all other clusters used the crystallographic cartesian coordinates of the respective cluster. The optimized coordinates were then used for the DFT calculations of bond orders and charges of the respective clusters.

4.4.2 Chemicals

Melts of nominal composition of K_3E_7 (E = As, Sb) were prepared by fusion (at high temperature) of stoichiometric ratios of the elements. ***CAUTION!*** The

elements were weighed out in a nitrogen atmosphere dry box then sealed in evacuated, silica tubes before firing. $Pd(PCy_3)_2$ and $Ni(COD)_2$ were purchased from STREM Chemicals. 4,7,13,16,21,24-hexaoxa-1,10-diazobicyclo[8.8.8] hexacosane (2,2,2-crypt was purchased from Aldrich. Anhydrous ethylenediamine (en) and dimethylformamide (dmf) were purchased from Fischer, vacuum distilled from K_4Sn_9 and stored under dinitrogen. Toluene was distilled from Na under dinitrogen and stored under dinitrogen.

4.4.3 Synthesis

4.4.3.1 Preparation of $[K(2,2,2\text{-crypt})]_4[Ni_{2+x}Sb_{16}]\cdot 2en$ and $[K(2,2,2\text{-crypt})]_4[Ni_5Sb_{17}]\cdot en$

K_3Sb_7 (50 mg, 0.052 mmol), $Ni(COD)_2$ (28 mg, 0.102 mmol) and 2,2,2-crypt (58 mg, 0.154 mmol) were dissolved in en (~ 2.5 mL) and stirred for 7h. After stirring, the solution was filtered through tightly packed glass wool. The filtered solution was heated at ~50 ºC for 8 min. and filtered through heated glassware. Solution was allowed to cool on the shelf for 24-48h at which time small black crystals of $[K(2,2,2\text{-crypt})]_4[Ni_{2+x}Sb_{16}]\cdot 2en$ and $[K(2,2,2\text{-crypt})]_4[Ni_5Sb_{17}]\cdot en$ begin to precipitate.

4.4.3.2 Preparation of $[K(2,2,2\text{-crypt})]_8[Pd_7As_{16}]_2\cdot 3.5en$

In vial 1, K_3As_7 (50.0 mg, 0.0779 mmol) and 2,2,2-crypt (57.3 mg, 0.156 mmol) were dissolved in en (~ 2 mL) and stirred for 5 min., yielding a dark red

solution. In vial 2, $Pd(PCy_3)_2$ (52.0 mg, 0.0779 mmol) was dissolved in tol (~ 1 mL) yielding a pale yellow solution. The solution from vial 2 was added drop wise to vial 1, and the mixture was stirred for 5h yielding a dark reddish-brown solution. The solution was then filtered through tightly packed glass wool. The filtered solution was refluxed for 15 min. and filtered again. After 1-4 days, black plate like crystals of $[K(crypt)]_8\mathbf{4}_2$•3.5en precipitated. For $[K(2,2,2\text{-crypt})]_8[Pd_7As_{16}]_2$·3.5en., EDX As:Pd:K = 2.37 :1.00: 4.00; MS (ESI) m/z 1985 $[KAs_{16}Pd_7]^-$.

4.4.4 Crystallographic Studies

The crystal structures of $[K(2,2,2\text{-crypt})]_4[Ni_{2.10}Sb_{16}]$· 2en, $[K(2,2,2\text{-crypt})]_4[Ni_5Sb_{17}]$· en, and $[K(2,2,2\text{-crypt})]_8[Pd_7As_{16}]$· 3.5en were solved by Dr. Jim Fettinger. Some of the crystallographic parameters are summarized in tables 4.1 and 4.2. Select bond distances and angles of the anions are given in tables 4.3 – 4.5.

Chapter 5

Molecular Clusters as Nanoparticle Precursors: Synthesis and Characterization of $[Pd_2E_{14}]^{4-}$ (E = P, As)

5.1 Introduction

The use of inorganic clusters as binary and metallic nanoparticle precursors has received increased interest.[13,177] The clusters contain metal-metal or binary bonds and can be considered as templates for metal-metal or binary bonds in the desired nanoparticles. Chalcogenide clusters (i.e. $[Cd_{10}Se_4(SPh)_{16}]^{4-}$) have been heavily studied as precursors to nanoparticles, such as CdSe which can be used as quantum-dot semiconductors.[14] Reported chalcogenide molecular clusters are stabilized by organic and organometallic ligands and often require thermal degradation steps to remove the ligands and produce the nanoparticles.[130,178] Use of molecular clusters free of carbon based ligands is limited by the availability of the carbon-free transition-metal molecular complexes. Anions of this type for chalcogenide (MoS_2) and halogen ($MoCl_6$) transition-metals are known.[115] The ME_8^{n-} (M = Nb, Cr, Mo; E = As, Sb; n = 2, 3) series of Zintl ion clusters and $[Ti(P_5)_2]^{2-}$, however, are the only carbon-free transition-metal clusters known for pnictogen elements.[44,50-52,94] Attempts to isolate carbon free binary anions by removing ligands from known transition-metal Zintl ion clusters that contain carbonyl or phosphine ligands have

been difficult and unsuccessful.[49,179] Direct synthesis of carbon-free binary anions from more weakly coordinated transition-metal precursors is necessary.

Micelles and reverse micelles, among other methods, have been implemented for the dispersity of nanoparticles produced from inorganic cluster precursors.[5,13,180-182] Implementing methods that contain micelles or polymeric materials (i.e. Polyvinyl pyrolidine) are used to control particle size formation by surrounding or encapsulation particles limiting interaction between particles and inhibiting further particle growth. Micelles and polymeric materials typically have long carbon chains that protrude from the encapsulated particles preventing the advancement of other particles and ideally resulting in nanoparticle dispersion. However, all surfactants used for this purpose require water to form the micelles. Often inorganic molecular cluster that contain group 14 and 15 elements are air and/or moisture sensitive. This sensitivity of the clusters makes the use of aqueous micelles and reverse micelles unsuitable. Studies using various non-aqueous reverse micelles have been reported for dyes[183] and organic molecules[184-186], but using them to encapsulate inorganic cluster anions has not been reported.

Herein, the isolation and characterization of two new isomorphic ligand-free binary anions with a novel cluster structure, $[Pd_2(E_7)_2]^{4-}$ (E = P, As), are reported. The use of the arsenic cluster analogue as a precursor to Pd/As binary phase nanoparticles is presented. Cationic non-aqueous reverse micelles are used to control the nanoparticle dispersity.

5.2 Results

5.2.1. Synthesis

En solutions of K_3E_7 (E = P, As) containing two equivalents of 2,2,2-crypt react with toluene solutions of $Pd(PCy_3)_2$ (PCy_3 = tricyclohexyl phosphine) to give air sensitive black crystals of the respective $[K(2,2,2\text{-crypt})]_4[Pd_2E_{14}]\cdot 5en$ complexes (when E = P, **5.1**, and As, **5.2**) . Complex **5.1** is produced in a ca. 10% crystalline yield, and **5.2** is produced in a ca. 20% crystalline yield. Complex **5.1** was characterized by ^{31}P NMR, Electrospray Ionization Mass Spectrometry (ESI-MS), Energy Dispersive X-ray (EDX), and single crystal X-ray diffraction. Complex **5.2** was characterized by ESI-MS, EDX, and single crystal X-ray diffraction.

A solvent activation process is responsible for the 2 electron oxidation needed to produce complex **5.2** (see eq. 5.1). The hydrogen trapping experiment that confirmed this oxidation process utilizes the head gases produced in eq. 5.1 to hydrogenate *trans*-stilbene to bibenzyl in the presence of a Pd catalyst (see eq. 5.2).

$$2\ Pd(PCy_3)_2 + 2\ As_7^{3-} + 2\ en \rightarrow Pd_2As_{14}^{4-} + 4\ PCy_3 + 2\ NH_2(CH_2)_2NH^{-1} + H_2 \qquad 5.1$$

$$PhCH{=}CHPh + H_2 \xrightarrow{[Pd]/C} PhCH_2CH_2Ph \qquad 5.2$$

Solvent activation during anion formation has been observed before for transition-metal/ Zintl ion complexes, $[E_7PtH(PPh_3)]^{2-}$ (E = P, As) and $[Sn_9Pt_2(PPh_3)]^{2-}$.[96,179] While a similar hydrogen trapping experiment was not carried out for the phosphorous analog, **5.1**, it is expected that its formation follows a similar pathway.

5.2.2. Solid State Structure

The $[K(2,2,2\text{-crypt})]_4[Pd_2(\mu, \eta^2, \eta^2 - E_7)_2]$, (E = P, As), salts are isomorphic crystallizing in the space group C2/c. The unit cells of both contain four cations and five ethylenediamine molecules per anion. The solvate molecules are not within bonding distances to any of the anions in the unit cell and are all in varying degrees of disorder. However, the anions are all well behaved crystallographically. The $[Pd_2(E_7)_2]^{4-}$ anions , E = P, **5.1**, and As, **5.2**, have crystallographically imposed C_i symmetry but virtual D_{2h} point symmetry. The crystal data for both monoclinic structures are presented in Table 5.1. Selective bond distances and angles for both complexes are presented in tables 5.2 and 5.3.

Table 5. 1. Select crystallographic data for $[K(2,2,2\text{-crypt})]_4[5.1] \bullet 5$ and $[K(2,2,2\text{-crypt})]_4[5.2] \bullet 5en$.

	$[K(2,2,2\text{-crypt})]_4$[**5.1**] • 5en	$[K(2,2,2\text{-crypt})]_4$[**5.2**] • 5en
formula	$C_{82}H_{184}K_4N_{18}O_{24}Pd_2P_{14}$	$C_{82}H_{184}K_4N_{18}O_{24}Pd_2As_{14}$
fw	2609.25	3224.55
T [K]	193(2)	193(2)
$\lambda_{MoK\alpha}$ [Å]	0.71073	0.71073
space group	C2/c	C2/c
a [Å]	15.6223(13)	15.9232(10)
b [Å]	23.4400(19)	23.7330(14)
c [Å]	33.876(3)	34.141(2)
β [˚]	90.436(2)	90.8170(10)
V [Å^3]	124046(18)	12892.8(14)
Z	4	4
ρ_{calcd} [g cm^{3-}]	1.397	1.661
μ [mm^{-1}]	0.672	4.039
crystal size [mm]	0.324 x 0.124 x 0.045	0.573 x 0.396 x 0.277
reflections collected	25899	100115
independent	8105 [R(int) = 0.0822]	14810 [R(int) = 0.0620]
final R [I >2σ(I)]	R1 = 0.1169, wR2 = 0.1411[a]	R1 = 0.0431, wR2 = 0.1051[b]
R indices (all data)	R1 = 0.1169, wR2 = 0.1618[a]	R1 = 0.0753, wR2 = 0.1147[b]

[a]. The function minimized during the full-matrix least-squares refinement was $\Sigma w(Fo^2\text{-}Fc^2)$ where $w=1/[\sigma^2(Fo^2)+(0.0909*P)^2+0.230*P]$ and $P=\max(Fo^2,0)+2*Fc^2)/3$. [b]. The function minimized during the full-matrix least-squares refinement was $\Sigma w(Fo^2\text{-}Fc^2)$ where $w=1/[\sigma^2(Fo^2)+(0.0502*P)^2+34.5632*P]$ and $P=\max(Fo^2,0)+2*Fc^2)/3$.

Table 5. 2. Select bond distances (Å) for $[Pd_2(E_7)_2]^{4-}$ (E = P, As).

	distances	
	$[Pd_2(P_7)_2]^{4-}$	**$[Pd_2(As_7)_2]^{4-}$**
Pd1 – Pd1'	2.6879(10)	2.7144(6)
Pd1 – E4	2.386(2)	2.4779(5)
Pd1 – E7	2.3916(19)	2.4831(5)
Pd1' – E5	2.3980(19)	2.4718(5)
Pd1' – E6	2.3878(19)	2.4752(5)
E1 – E2	2.143(3)	2.3661(8)
E1 – E3	2.146(3)	2.3616(7)
E2 – E5	2.214(3)	2.4418(7)
E2 – E6	2.191(3)	2.4458(6)
E3 – E4	2.207(3)	2.4343(6)
E3 – E7	2.203(3)	2.4455(7)
E5 – E4	2.199(3)	2.4070(6)
E6 – E7	2.195(2)	2.4235(7)

The $[Pd_2(E_7)_2]^{4-}$ anions **5.1** and **5.2** contain two norbornane-like E_7^{5-} clusters that each bind in an η^2 fashion to both palladiums of the Pd_2^{6+} unit (figure 5.1). This electron counting scheme follows the Zintl-Klemm formalism and gives the required overall -4 charge seen in the unit cell.[26,166,167] The Zintl-Klemm formalism, as was discussed in chapter 4, was designed for explaining charge distribution in Zintl ion clusters. The formalism follows the 8-N rule and compares atomic coordination of the main group atoms in Zintl clusters to isoelectronic elements of other known clusters (i.e. $E^- \cong CH_2 \cong S$). Therefore, there are three possible E_7 Zintl-Klemm descriptions I) nortricyclic-like E_7^{3-}, II) norbornadiene-like E_7^{1-} and III) norbornane-

like E_7^{5-}, see scheme 5.1. These three descriptions were previously discussed in chapter 4 and depicted in scheme 4.2.

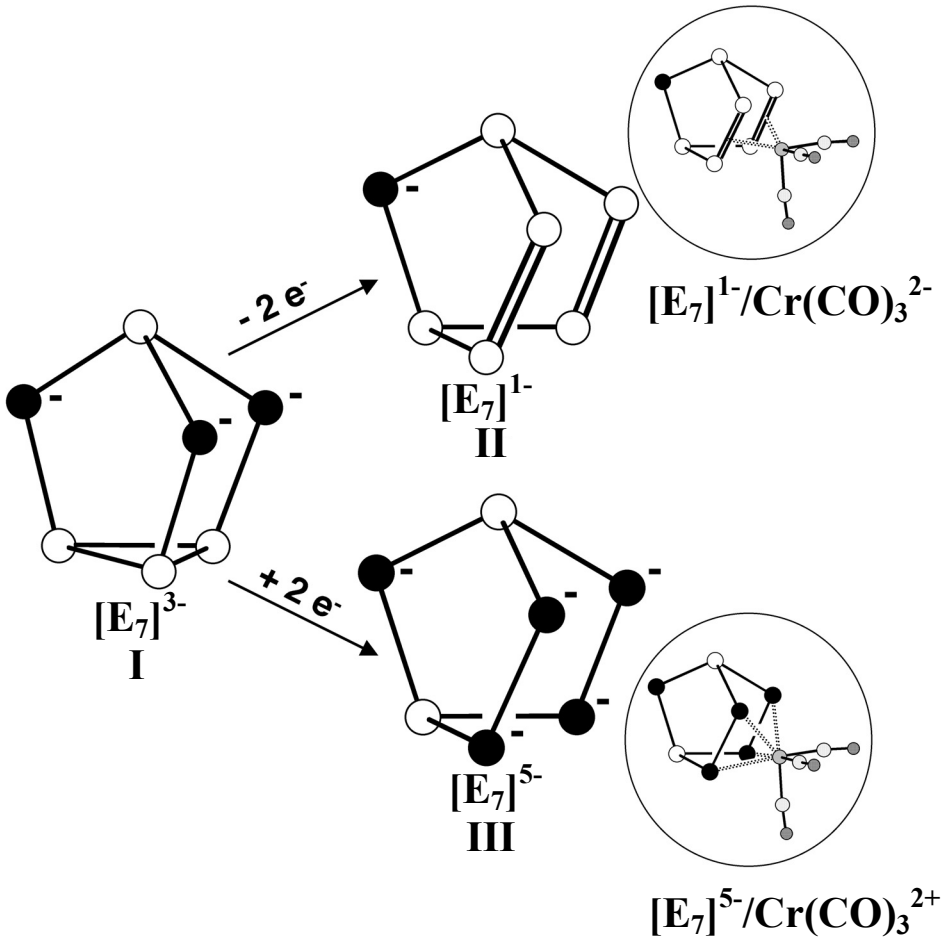

Scheme 5.1

The bond distances between E4-E5 and E6-E7 (see figure 5.1) of the ions, $[Pd_2(E_7)_2]^{4-}$ (E = P, As), are typical of P-P and As-As σ-bonds, respectively. Therefore, the five atoms, E1, E4-E7, each carry a single negative charge like those of the E_7^{5-} cage represented in scheme 5.1. Thus, the cluster has a combined 10- charge contributed from the $2E_7^{5-}$ cages. To obtain the crystallographically determined overall 4- charge of the anionic cluster each Pd atom must have a 3+ charge.

Table 5. 3. Select bond angles (º) for $[Pd_2(E_7)_2]^{4-}$ (E = P, As).

	distances	
	$[Pd_2(P_7)_2]^{4-}$	**$[Pd_2(As_7)_2]^{4-}$**
Pd1-Pd1'-E6	85.48(5)	85.436(15)
Pd1'-Pd1-E4	83.80(5)	88.237(14)
E5-Pd1'-E6	73.97(6)	77.166(17)
E4-Pd1'-E7	83.80(5)	77.222(16)
E7-Pd1-E5	167.12(7)	172.439(18)
E4-Pd1-E6	169.27(7)	173.667(18)
E2-E5-Pd1'	98.68(9)	99.30(2)
E3-E7-Pd1	98.44(9)	99.54(2)
E2-E6-E7	104.06(10)	103.66(2)
E3-E4-E5	103.48(11)	104.47(2)
E5-E2-E6	81.64(9)	78.282(19)
E4-E3-E7	81.59(9)	78.754(19)
E5-E2-E1	107.76(11)	108.10(2)
E6-E2-E1	107.45(11)	107.38(2)
E4-E3-E1	107.48(11)	107.33(2)
E7-E3-E1	108.05(11)	107.57(3)
E2-E1-E3	97.11(10)	98.29(2)

Both of the palladium metal centers are in distorted square planar coordination and are linked to each other through an axial Pd-Pd bond. The singly occupied d_{z^2} orbitals of both Pd atoms are used to form the axial Pd-Pd bonds, 2.6879(10)Å and

2.7144(6)Å for **5.1** and **5.2**, respectively. The $[Pd_2(E_7)_2]^{4-}$ clusters rare examples of Pd^{3+} dinuclear anions. The average Pd-E (E = P, As) bond distances of **5.1** and **5.2** are 2.391(2)Å and 2.477(5)Å, respectively. The Pt atoms of the $[(PPh_3)HPtE_7]^{2-}$ (E = P, As) complexes are in square planar arrangements similar to the Pd atoms in the $[Pd_2(E_7)_2]^{4-}$ anions but the E_7 units are different structural arrangements, nortricyclic and norbornane, respectively.[45,179] The M-E_7 bonds of the two structure types compare well when differences in the Pd/Pt covalent radii are considered. The norbornane-like E-E (E = P, As) bonds range from 2.143(3) to 2.207(3)Å for **5.1** and 2.3616(7) to 2.4455(7)Å for **5.2**. The E-E bonds for both complexes fall within the reported E-E ranges seen in the $[\eta^4\text{-}E_7M(CO)_3]^{3-}$ (E = P, As, respectively; M = Cr, Mo, W) structures which also have E_7 "norbornane"-like structures .[18]

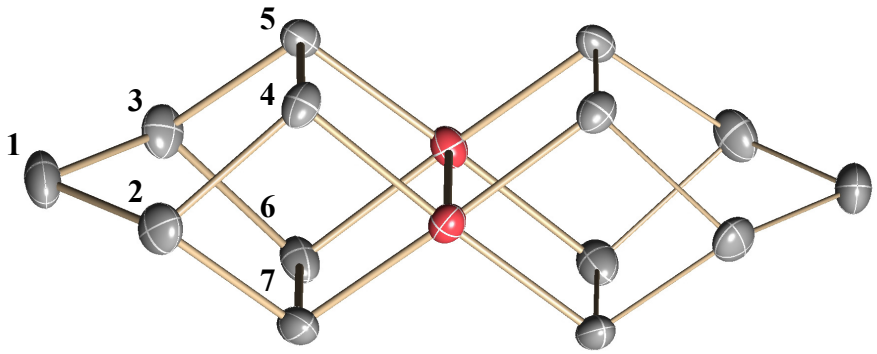

Figure 5. 1. An ORTEP drawing of $[Pd_2(As_7)_2]^{4-}$; red spheres represent palladium. All thermal ellipsoids are at 50% probability.

5.2.3. ^{31}P NMR

$[Pd_2P_{14}]^{4-}$. The phosphorous complex, **5.1**, is static on the NMR time scale. Anion **5.1** has crystallographically imposed C_i symmetry but has virtual D_{2h}

symmetry that gives it an AA'A''A'''MM'X spin system. The ^{31}P NMR spectrum of $[Pd_2(P_7)_2]^{4-}$ crystals dissolved in dmso-d_6 shows a triplet (δ = 63.10 ppm; $^1J_{P\text{-}P}$ = 367 Hz, P1), a second order multiplet (δ = 23.56 ppm; P2, P3), and a second order quartet (δ = -60.30 ppm; P4, P5, P6, P7), see figure 5.2. The static nature of the E_7 atoms in solution was also observed for $[P_7Ni(CO)]^{3-}$ giving the same spin system.[18,45]

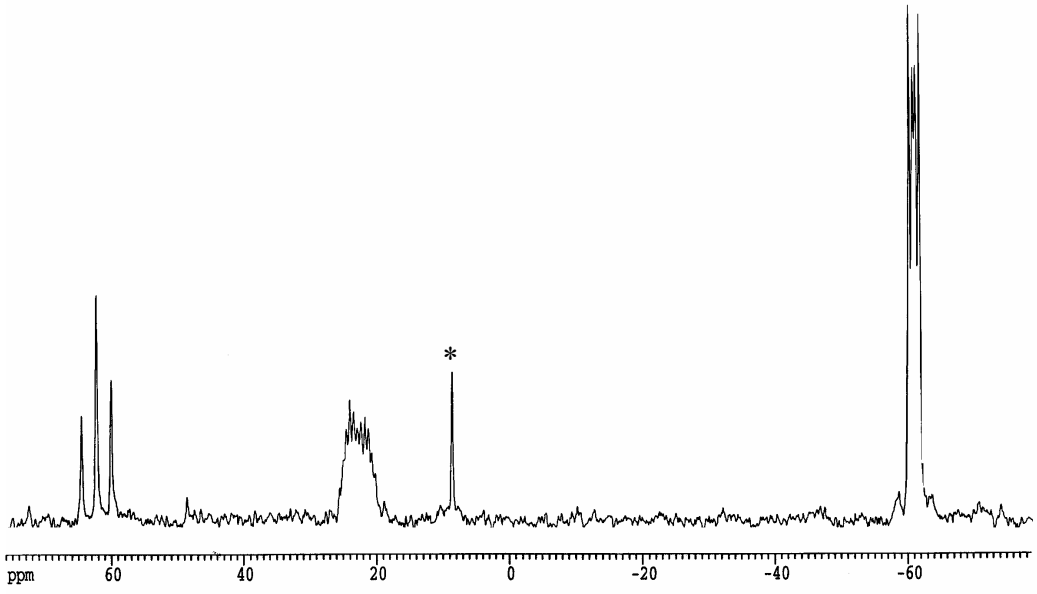

Figure 5. 2. ^{31}P NMR spectrum of 5.1 in a dmso-d_6 solution (* denotes crystalline PCy_3 impurity).

5.2.4. ESI-MS

$[Pd_2(P_7)_2]^{4-}$. The ESI mass spectrum was recorded in the negative ion mode from a dmf solution of complex **5.1**. The base peak observed at 1063.3 m/z matches the simulated mass envelope of the $[K(2,2,2\text{-crypt})]^{1+}$ adduct of the doubly protonated

anion $[H_2Pd_2P_{14}]^{2-}$ (figure 5.3a-b). While it is common to observe protonated or oxidized Zintl anions and even alkali adduct species in the gas phase, this is the first example in Zintl chemistry of a $[K(2,2,2\text{-crypt})]^{+1}$ adduct observed in the gas phase.

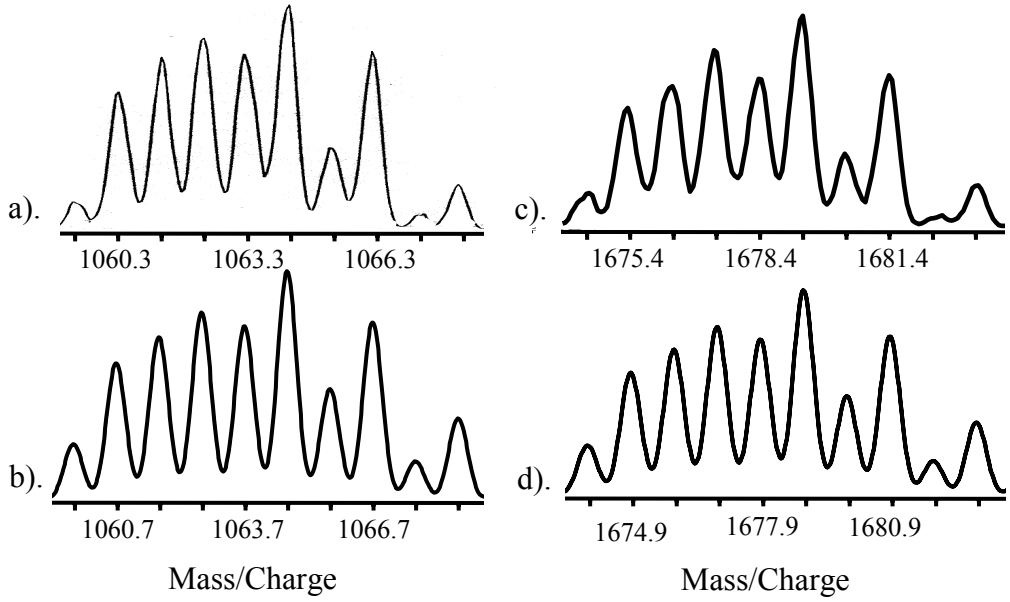

Figure 5. 3. Electrospray ionization mass spectra of the complexes **5.1**(a) and **5.2**(c) in dmf solutions as the ions $[K(2,2,2\text{-crypt})][H_2Pd_2P_{14}]^{1-}$ and $[K(2,2,2\text{-crypt})][HPd_2As_{14}]^{1-}$, respectively. Simulated isotopic patterns of both are pictured below (b) and (d), respectively.

The mass envelope at 649.5 m/z match that of the triply protonated anion, $[H_3Pd_2P_{14}]^{-1}$.

$[Pd_2(As_7)_2]^{4-}$. The ESI mass spectrum was recorded in the negative ion mode from a dmf solution of complex **5.2**. The mass envelope of an abundant peak at 1678.4 m/z matches the simulated pattern of the $[K(2,2,2\text{-crypt})]^{+}$ adduct of the singly protonated anion, $[HPd_2As_{14}]^{2-}$, (figure 5.3) similar to the phosphorus analog, but the base peak at 631.8 m/z resembles $[H_2PdAs7]^{-1}$. Other mass envelopes in the ESI mass spectra were at 1262.7 and 887.4 m/z indicating the presence of $[HPd_2As_{14}]^{-1}$ and $[Pd_2As_9]^{-1}$, respectively. The structure of the E_9 cluster is not presently known

but has since been seen observed in the gas phase of other transition-metal Zintl clusters.[51]

5.2.5. Reverse Micelle oxidation

The $[Pd_2(As_7)_2]^{4-}$ anion is free of organic and organometallic ligands and is an ideal precursor to binary Pd/As phases. Air oxidation of the crystals in the solid state produces a black powder that is amorphous by powder X-ray diffraction. The amorphous material was heated at 400 ºC for 2 hours in a sealed evacuated tube to crystallize the sample. A powder X-ray diffraction profile of the annealed material indicates the $PdAs_2$ phase as the major phase present in the sample (figure 5.4). Trace quantities of other Pd/As phases, Pd_2As and Pd_5As, and elemental As are also indicated by the diffraction pattern of the annealed material.

The high temperature solid state method to isolate bulk Pd/As phases from elemental arsenic and palladium is well-known. Isolation methods for nanomaterials of Pd/As phases are not established. Reverse micelles offer and environment were a limited number of $[Pd_2(As_7)_2]^{4-}$ clusters can be segregated. By limiting the number of clusters in proximity to each other when they are oxidized the resulting Pd/As phase with be of materials in the nano-size range. The moisture sensitivity of the anionic clusters requires the use of non-aqueous, polar solvent reverse micelles and solubility of the crystalline complexes dictates the polar solvent. Non-aqueous iso-octane/1-butanol/CTAC/dmf reverse micelles were prepared to control the size of the $PdAs_2$ particles. The crystals of the $[Pd_2(As_7)_2]^{4-}$ complex were dissolved in a small

quantity of dmf before introducing them to the reverse micelles. A drop of the $[Pd_2(As_7)_2]^{4-}$ reverse micelle solution was placed on a freshly cleaved single crystal

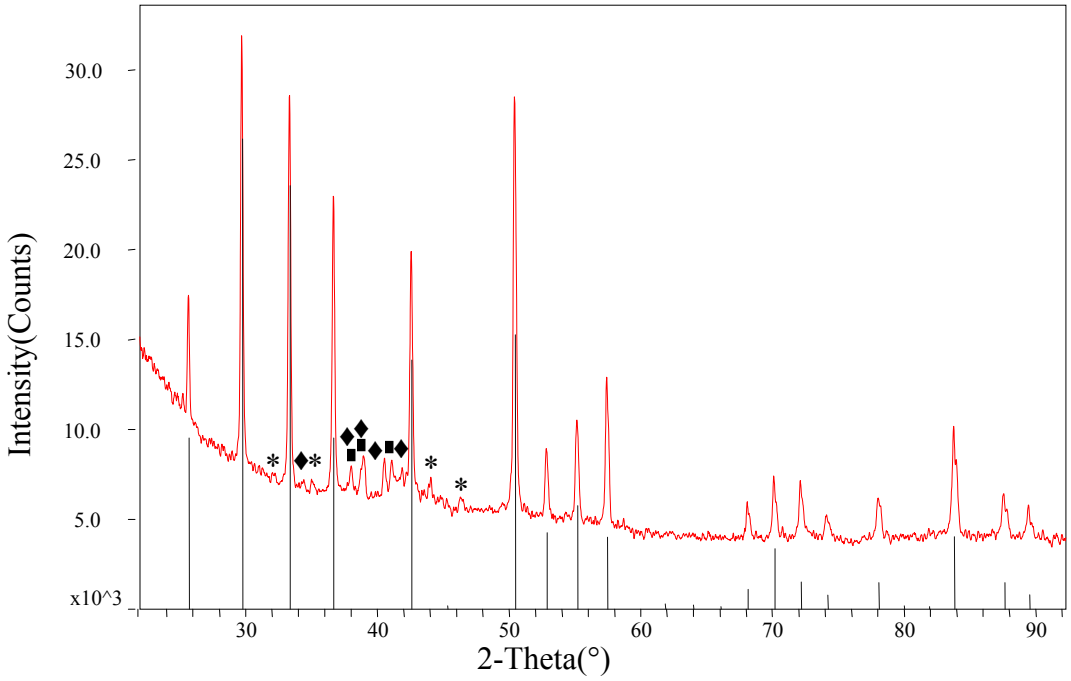

Figure 5. 4. X-ray diffraction pattern of material produced from air oxidation of the $[Pd_2(As_7)_2]^{4-}$ complex after annealing at 400°C for 2 hours. The black line diagram represents the $PdAs_2$ phase (JCPDS #73-1649). [127] The trace impurity peaks denoted by asterisks are from elemental arsenic, the diamonds are from Pd_5As_2, and the squares are from Pd_2As.

mica surface. The crystal surface was then exposed to air to oxidize the $[Pd_2(As_7)_2]^{4-}$ anions. The surface was imaged by SEM and indicated monodispersed 20 nm particles (figure 5.5). Air oxidation of $[Pd_2(As_7)_2]^{4-}$ anions in reverse micelles results in an amorphous material by XRD. The diffraction pattern obtained after the oxidized material was annealed at 400 ºC for 2 hours in evacuated sealed tube indicates the presence of $PdAs_2$ and Pd_2As phases (figure 5.6).

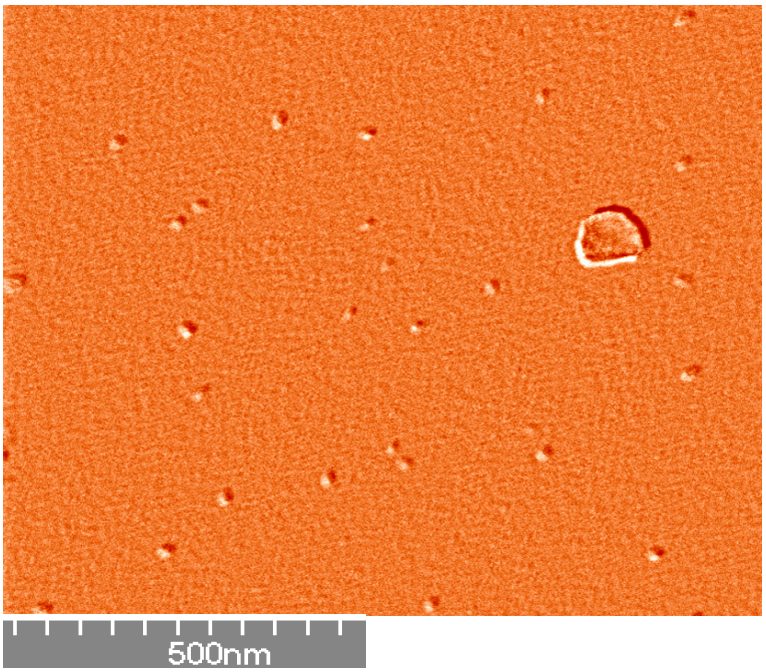

Figure 5. 5. SEM image of Pd/As nanoparticles isolated by air oxidizing $[Pd_2(As_7)_2]^{4-}$ non-aqueous reverse micelles on a freshly cleaved single crystal mica surface.

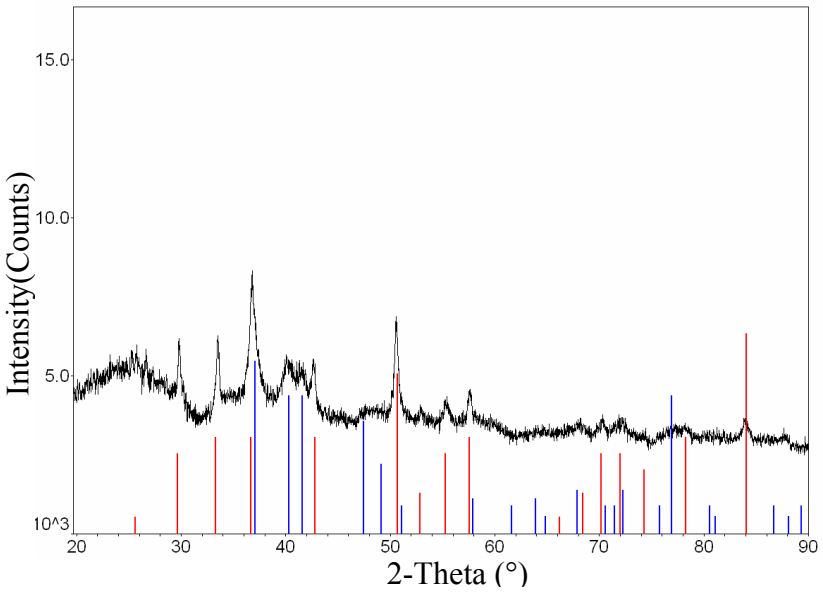

Figure 5. 6. X-ray diffraction pattern of the sample produced from oxidizing the reverse micelle solution of the $[Pd_2(As_7)_2]^{4-}$ after it was annealed at 400 ºC for 2 hours. The red and blue lines represent the $PdAs_2$ and Pd_2As phases according to the JCPDS #03-1194 and #17-0226, respectively. [188,189]

5.3 Discussion

The $Pd_2(E_7)_2$ structure type is very unique. Multiple E_7 units have been observed in variety of arsenic and phosphorous anions. E_7 units, whether nortricyclic or norbornane-like, are commonly linked in large phosphorous polyatomic anions (i.e. $H_2P_{14}^{2-}$ and P_{21}^{3-}).[190-192] The P_7 units in the polyatomic $H_2P_{14}^{2-}$ structure are linked directly through two 2c-2e bonds from a nortricyclic-like E_7 cage to a norbornane-like E_7 cage. If the two protons are displaced from the norbornane-like cage of $H_2P_{14}^{2-}$, the norbornane-like cage would be free to make two more 2c-2e bonds to a third nortricyclane-like E_7 cage, as is seen by the P_{21}^{3-} cage. Fewer polyatomic arsenic anion clusters are known, As_7^{3-}, As_{11}^{3-} and As_{22}^{4-}.[33,41,193] While one of the P_7 cages undergoes structural rearrangement before oxidatively coupling to the second P_7 cage to form $H_2P_{14}^{2-}$, the two As_{11}^{3-} cages that are oxidatively coupled to form As_{11}^{4-} both maintain their original As_{11} structural arrangement. However, the only known dimeric structure of two nortricyclic As_7 units is the $[SnAs_{14}]^{4-}$ cluster which has two nortricyclic-like cages linked asymmetrically by a Sn ion.[153]

Typically, when P_7 or As_7 cages are coupled to transition-metal fragments, only a single E_7 unit is involved in the cluster either in a nortricyclic or norbornane arrangement.[16,45] However, the P_{14} cluster in $[\{Ni(PBu_3)_2\}_4P_{14}]$ can be viewed as a dimer linked by two $[\{Ni(PBu_3)_2\}P_7]$ units at the P(1) site (see figure 5.1) and bridged by two additional $[Ni(PBu_3)]$ fragments. [194] The $[Pd_2(E_7)_2]^{4-}$ clusters are unique from this other transition-metal / Zintl ion dimer and the polyatomic Zintl dimers because they are linked by a metal dimer unit instead of being formed by 2c-2e, E-E bonds of

the E_7 cages. The norbornane E_7 units found in the $[Pd_2(E_7)_2]^{4-}$ structure are each bonded η^2,η^2 to the Pd_2 unit that bridges them decreasing the possibility of creating chain structures. While **5.1** and **5.2** are the first carbon-free transition-metal Zintl ion dimers isolated, polymeric chains for both group 14 and 15 Zintl ion transition-metal anions have been reported.[44,50,195] The bonding configuration of **5.1** and **5.2** limits the chances of forming linear polymers, which would have to occur through a single 2c-2e bond at the E1 atom, see figure 5.1.

The $[Pd_2(E_7)_2]^{4-}$ dimeric clusters not only offer a unique structural arrangement but also a Zintl-Klemm charge distribution that has not been previously observed in transition-metal / E_7 complexes. The formal 5- charges on the E_7 cages indicate σ-bonds throughout the clusters with 1- charges residing on atoms E1,E4-E7, see figure 5.1. The $[(CO)NiP_7]^{3-}$ cluster has a similar E_7 cage structure as those in the $[Pd_2(E_7)_2]^{4-}$ clusters, but has shorter E4-E5 and E6-E7 bonds. [149] The shorter bonds are within known P-P double bonds. [196-198] Therefore, while the **5.1** and **5.2** clusters favor a E_7^{5-} norbornane-like description of their E_7 cages, the E_7 cage of $[(CO)NiP_7]^{3-}$ favors a E_7^{1-} norbornadiene-like description. The E_7^{1-} cage has a carbonylated metal fragment as opposed to the dimer formation seen in the dimers discussed in this chapter. The longer bonds seen in the $[Pd_2(E_7)_2]^{4-}$ anions may result from the Pd_2 orientation which stretches along the same axis as the E4-E5 and E6-E7 bonds.

Transition-metal fragments free of organic or organometallic ligands create the necessary environment for these dimers to crystallize. In doing so, the resulting clusters can be considered "charged" binary intermetallics in which the clusters resemble binary phases with extra electrons. While many organometallic clusters

have metallic or bimetallic cores that are discrete pieces of their corresponding phases,[128,130] the $[Pd_2(E_7)_2]^{4-}$ clusters do not. Free of organic or organometallic ligands these novel dimer clusters present a direct pathway to binary phases which only requires a room temperature oxidation step to remove the extra electrons. This eliminates the need for thermal degradation to remove the ligands that stabilize the previously used binary clusters.[130]

Both physical and chemical communities have been interested in using molecular clusters as precursors to metallic or binary phase nanomaterials for over a decade.[199-201] Many have successful used binary molecular clusters, such as $[Cd_{10}Se_4(SPh)_{16}]^{4-}$, as precursors to nanoparticles of transition-metal chalcogenides. [13] Attempts to extend this idea of using binary molecular cluster as binary phase precursors to transition-metal pnictides can not be as easily found. Nanoparticles of FeP and FeP_2 can be isolated from reduction of precipitated $Fe_2(P_4O_{12})$ nanoparticles with hydrogen but must be done at high temperatures (700 ºC and 1100 ºC, respectively). [8]

The lack of transition-metal/pnictide molecular clusters to use is likely the source of this lack of investigation. The extra electrons of the $[Pd_2(As_7)_2]^{4-}$ dimer are easily removed by air oxidation to produce primarily the $PdAs_2$ phase. As the emerging class of "charged" binary intermetallics, that are made accessible by group 15 Zintl ions, continues to grow, a large variety of nanoparticles of transition-metal pnictide phases may be available for catalytic and optical applications.

5.4 Experimental

5.4.1. General

All reactions were carried out in a nitrogen atmosphere dry box (Vacuum Atmosphere Co). Electrospray Mass spectra were obtained by direct injection of dmf solutions into a Finnigan mass spectrometer. Samples were detected in the negative ion mode after being ionized by an ESI probe. An AMRAY 1820K scanning electron microscope with a potential of 20 kV was used for energy dispersive X-ray (EDX) studies. The ^{31}P NMR spectrum was recorded on a Bruker DRX Advance 400 (161.976 MHz) spectrometer. A Bruker D8 Advance θ-θ X-ray Powder Diffractometer (CuK_α radiation, Kevex detector) was used to obtain XRD patterns for phase identification. A step width of 0.02º between $5º \leq 2\theta \geq 90º$ was used. Analysis of the XRD patterns was done using the JADE® software package equipped with the JC-PDF database and auto indexing. [127] SEM images were captured on a Hitachi S4700-FE by Tim Maugel.

5.4.2. Chemicals

Melts of nominal composition of K_3E_7 (E = P, As) were prepared by fusion (at high temperature) of stoichiometric ratios of the elements. ***CAUTION***! The elements were weighed out in a nitrogen atmosphere dry box then sealed in evacuated, silica tubes before firing. $Pd(PCy_3)_2$ was purchased from STREM Chemicals. 4,7,13,16,21,24-hexaoxa-1,10-diazobicyclo[8.8.8] hexacosane (2,2,2-crypt) and cetyltrimethylammonium chloride (CTAC) were purchased from Aldrich.

Single crystal mica disks were purchased from SPI Supplies. Anhydrous ethylenediamine (en) and dimethylformamide (dmf) were purchased from Fischer, distilled from K_4Sn_9 and stored under nitrogen atmosphere. Toluene was distilled from Na under nitrogen and stored under nitrogen. Isooctane was purchased from Fischer and purged with nitrogen and stored over NaK under nitrogen. 1-butanol was purchased from Fischer purged with nitrogen and dried over sieves. It was then stored over fresh sieves under nitrogen. Acetonitrile was purchased from EMD and used without further purification.

5.4.3. Synthesis

5.4.3.1. Preparation of $[K(2,2,2\text{-crypt})]_4[Pd_2P_{14}]\bullet 5en$

In vial 1, K_3P_7 (30.0 mg, 0.089 mmol) and 2,2,2-crypt (68.0 mg, 0.180 mmol) were dissolved in en (~ 2 mL) and stirred for 5 min. In vial 2, $Pd(PCy_3)_2$ (60.0 mg, 0.095 mmol) was dissolved in tol (~ 1 mL) yielding a pale yellow solution. The solution from vial 2 was added drop wise to vial 1, and the mixture was stirred for 5h yielding a dark brown solution. The solution was then filtered through tightly packed glass wool. The filtered solution was refluxed for 15 min. and filtered through hot glassware. After 7 days, black parallelepiped crystals of $[K(crypt)]_4$**1**•5en precipitated. Yield: ~10 mg (~10 %). EDX P:Pd:K = 6.30: 1.00: 2.34; MS (ESI) m/z 1263 $[K(2,2,2\text{-crypt})H_2Pd_2P_{14}]^{-1}$; $^{31}P\{^1H\}$ NMR (dmso-d_6) δ (ppm) 63.1 (P1) ($^1J_{p\text{-}p}$ = 367 Hz), 23.56 (P2, P3) and -60.30 (P4, P5, P6, P7).

5.4.3.2. Preparation of $[K(2,2,2\text{-crypt})]_4[Pd_2As_{14}]\bullet 5en$

In vial 1, K_3As_7 (50.0 mg, 0.0779 mmol) and 2,2,2-crypt (57.3 mg, 0.156 mmol) were dissolved in en (~ 2 mL) and stirred for 5 min., yielding a dark red solution. In vial 2, $Pd(PCy_3)_2$ (52.0 mg, 0.0779 mmol) was dissolved in tol (~ 1 mL) yielding a pale yellow solution. The solution from vial 2 was added drop wise to vial 1, and the mixture was stirred for 5h yielding a dark reddish-brown solution. The solution was then filtered through tightly packed glass wool. The filtered solution was refluxed for 15 min. and filtered through hot glassware. After 1-4 days, black parallelepiped crystals of $[K(crypt)]_4$**2**•5en precipitated. Yield: ~25 mg (~20 %) of mixed crystals. EDX As:Pd:K = 7.10: 1.00: 1.96; MS (ESI) m/z 1678 $[K(2,2,2\text{-crypt})HPd_2As_{14}]^{-1}$.

5.4.3.3. Preparation of Reverse Micelle Solution

CTAC, 25% in H_2O, was dried under vacuum. The dried CTAC was dissolved in isooctane containing 10 vol% 1-butanol and dmf ([dmf]/[CTAC] = 6.53) was added to create the reverse micelles. The surfactant concentration in solution was 0.10 mol / L and was dried over fresh sieves for 6 hours. $[K(2,2,2\text{-crypt})]_4[Pd_2(As_7)_2]$ • 5 en was dissolved in dmf (0.01 μM). Surfactant solution was added to dmf solution of $[K(2,2,2\text{-crypt})]_4[Pd_2(As_7)_2]$ • 5 en (6×10^{-4} mol $[Pd_2(As_7)_2]^{4-}$/ L of reverse micelle solution) producing a clear light brown solution.

5.4.4. Crystallographic Data

The crystal structures of $[K(2,2,2\text{-crypt})]_4[Pd_2(P_7)_2]$•5en and $[K(2,2,2\text{-crypt})]_4[Pd_2As_{14}]$•5en were solved by Dr. Jim Fettinger. Some of the crystallographic parameters are summarized in table 5.1 and select bond distances and angles of the anions are given in table 5.2 and 5.3.

Chapter 6

Conclusion

As has hopefully been evident by the studies presented throughout this document many important contributions have been given to the chemical community. These contributions can be separated as 1) intellectual chemical contributions and 2) method development and application. These two areas are discussed in the subsequent sections.

6.1 Intellectual Chemical Contributions

The complexes presented in here have many unique structural arrangements. Many of the polyatomic main group cluster units of these binary anionic clusters are presumably new Zintl ions previously unseen in either the organic or inorganic fields. However, upon closer inspection as was done in chapter 4, some of these clusters while isolated from Zintl ion precursors do not fit the Zintl paradigm set forth by the Zintl-Klemm rules. [132,133] The clusters $[(Ni_2Sb_2)(Sb_7)_2]^{4-}$, $[Pd_7As_{16}]^{4-}$ and $[Ni_5Sb_{17}]^{4-}$ all contain characteristics of intermetallics, namely partial bonding and bond delocalization. On the other hand, while a Zintl-Klemm description could be extracted for $[(Ni_2Sb_2)(Sb_7)_2]^{4-}$, having Sb_7^{1-} units, a description for the other two could not be achieved. A discrete metallic core or pieces of the binary phases could

not be extracted either. It was suggested that these clusters were examples of a new type of molecular complex that straddle the intermetallic – molecular border, also known as the "Zintl-Klemm border".[202] The lack of organometallic or organic ligands originally set these binary clusters apart from other transition-metal / main group cluster both large and small. It may be this characteristic that allows these anions to straddle the "border".

If other members of the growing class of ligand-free binary cluster are viewed, it can be seen that the absence of organometallic ligands alone does not dictate where along the "Zintl-Klemm border" they reside. Chapter 4 briefly discussed the extraction of a Zintl-Klemm description for $[Pd_2(As_7)_2]^{4-}$, a cluster further discussed in Chapter 5. The phosphorous analog of the cluster shares the same description. These clusters while free of the undesirable ligands show no intermetallic characteristics and safely reside on the molecular side of the border. The cluster, $[As@Ni_{12}@As_{20}]^{3-}$, presented in chapter 4 contains the As_{20} polyatomic cluster. This neutral cage is isoelectronic to $C_{20}H_{20}$, where As ≅ CH, following the Zintl-Klemm rules. Not only does this describe the As_{20} cage but also is helpful in the total charge distribution picture of the entire onion skin cluster. Like the $[Pd_2(E_7)_2]^{4-}$ clusters, $[As@Ni_{12}@As_{20}]^{3-}$ resides on the molecular side of the border.

While the clusters reported in chapter 3 are the only clusters in this document to reside on the border having both intermetallic and molecular characteristics, there are other ligand-free binary clusters to consider. The other transition-metal / pnictogen clusters, the ME_8^{n-} series,[44,50,51] appear to have some that reside on the

border and some that favor a molecular description. The E_8^{8-} rings are isoelectronic to both S_8 and C_8H_{16} fitting nicely into a Zintl-Klemm description which put the metal atoms in +6 and +5 oxidation states. However, if bond valence analyses are done on the clusters, the arsenic clusters fit this previously stated Zintl-Klemm description but the antimony clusters do not. Partial bonding is observed for the antimony rings due to Sb-Sb distances that are longer than typical separations. Reported theoretical calculations done on the ME_8^{n-} also suggest that the Zintl-Klemm description imparts more ionic character on the cluster than actually exists.[203] Yet, regardless of the partial bonding and uncertain charge distribution, these metal centered eight-member rings do not resemble intermetallic structures. Therefore, it can be suggested that the arsenic cluster reside on the molecular side of the border and the antimony clusters reside on the border but with stronger molecular characteristics.

The other known ligand-free charged binary clusters are not pnictogen but tetrel clusters. The $[Pt@Pb_{12}]^{2-}$ cluster nicely follows the Wade-Mingos electron counting rules which dictates a closo-deltahedral structure.[131] It is isoelectronic to $B_{12}H_{12}$ with typical Pb-Pb distances fitting easily into a Zintl-Klemm description with only molecular characteristics. $[Pt_2Sn_{18}]^{4-}$, on the other hand, has no isoelectronic analog and the best Zintl-Klemm description is of two connected highly distorted deltahedral Sn_9^{2-} cages. [100] The Sn-Sn bond distances are typical of known Sn_9 clusters but do not fit into a Zintl-Klemm description suggesting that like the MSb_8^{2-} clusters it resides on the border but with stronger molecular characteristics.

Molecular compounds that fall on the intermetallic side of the Zintl-Klemm border are mostly extremely large chalcogenide clusters. Some of the chalcogenide clusters, $[Cu_{70}Se_{35}(PEt_3)_{22}]$ and $[Cu_{146}Se_{73}(PPh_3)_{30}]$, are essentially chunks of binary phases, Cu_2Se, and have properties more characteristic of intermetallics than molecular compounds.[130]

The unique ligand-free charged binary clusters discussed here represent a new class of molecular complexes that straddle the line between molecular and intermetallic properties. Better understanding of these clusters that reside on the border or close to it may offer a unique way of studying the properties of nano-architecture.

The concept of straddling the Zintl border was first exploited by solid-state chemist who used Zintl phases that fell along the border to isolate materials with novel properties that fell between intermetallics and semi-conducting Zintl phase. [202] Standard Zintl phases follow an ionic description like their Zintl ion counterparts which assume complete electron transfer from the electropositive elements to the electronegative ones. Therefore, the properties that are considered by most to indicate that a Zintl phase is straddling the border are similar to those seen for the molecular cluster presented here that straddle the line, such as delocalized bonding, mixed valent cations, and non-classical bonding (long bonds). A variety of different phases are reported to reside on the Zintl border. [204,205] The combination of intermetallic and Zintl phase properties that are seen in phases that reside on the border is exemplified by the phase, $Ca_5In_9Sn_6$. [206] This phase has two distinctly

different layer packings, *hcp* and *ccp*. The *hcp* layers contain indium trimers with normal In-In bond distances (3.045(3) Å). The *ccp* layers, on the other hand, have longer In-In distances (3.665(5) Å). The $Ca_5In_9Sn_6$ phase is therefore thought to have an intermetallic component (*ccp* layers) and a Zintl or "molecular" phase (*hcp* layers).

6.2 Method Development and Application

It is no secret that nickel, palladium and platinum are among the most catalytically active transition-metals in heterogeneous systems. In recent years, a second transition-metal has been added to enhance the performance of known catalysts for heterogeneous systems by either improving their selectivity, activity, or longevity. [9,11] Addition of a main group element to a group 10 catalyst has also proven beneficial to CO oxidation and hydrocarbon reforming heterogeneous catalytic systems, namely Pt/Sn systems. [10,11] Structural and mechanistic similarities between Pt/Sn catalyst systems and Pt/Sn Zintl complexes have been noted. [100]

In addition to the components in these catalysts, particle size has become of increasing importance breaking into the nano- mine field. The small particles provide increased surface to size ratios. It has also been documented that changing the particle size can alter the catalytic potential of the materials completely, as was observed for 1.4 nm gold particles. [64,65] Aside from catalytic applications, particles in the nano-regime can also display unique optical and electronic properties different from their bulk counterparts.

While bulk main group / transition-metal intermetallic materials are generally prepared by high temperature, solid state reactions of stoichiometric ratios of the elements, a variety of methods have been proposed for the binary nano-intermetallics. One of particular interest is the use of transition-metal main group organometallic clusters as precursors. [64] Often the cluster undergoes thermal degradation resulting in the corresponding binary intermetallic. The preformed bonds between the two elements present in the cluster are believed to facilitate the formation. However, these clusters are generally of transition-metal / chalcogenide clusters whose binary phase diagrams only contain one or two binary phases. Most clusters do not have the appropriate stoichiometry of the binary elements necessitating a second source of typically the main group atom for the reaction to proceed; however, not all methods require stoichiometric ratios of the elements. The clusters used as binary intermetallic precursors often contain organometallic ligands or halides that require an extra step to ensure their removal. When halides (i.e. Cl) are present in a cluster, failure to remove all traces may result in poisoning of the catalytic system.

The growing class of ligand-free binary clusters, of which the clusters reported in this thesis are all members, are ideal precursors for binary intermetallics. Containing only transition-metals and main group atoms these cluster are more straightforward binary precursors than those previously used. Chalcogenide clusters are commonly used as binary precursors. All of the binary molecular clusters presented in this document are pnictogen complexes. However, unlike the transition-metal / chalcogenide binary phase diagrams, the transition-metal / pnictogen binary phase diagrams each contain a variety of different stoichiometric phases rather than

only single phases. This opens the door to a larger number of potentially catalytic, optically or electronically beneficial new nanoparticles. The variety of possible phases for a single binary system means an extra source typically of the main-group element must be added to give the appropriate binary atomic ratio and to adjust for all of the different phases.

The clusters reported in this thesis as well as the other ligand-free binary clusters are accessible by employing Zintl anions as precursors. When an extra source of the main group element is needed, Zintl ions can again be used. Zintl anions offer a unique polyatomic source of a main group element free of undesirable ligands. A simple, mild method for converting transition-metal / Zintl complexes into binary phase requires only air oxidation to produce the binary phases. Other reported methods for obtaining single phase binary nanoparticles also use alkali / pnictogen salts, but are in a 3:1 ratio and only produce the most thermodynamically stable binary phase. [66]

Even though these Zintl clusters have a variety of different transition-metal:main-group atomic ratios there is little control over this ratio. The non-interacting counter cations of most Zintl complexes isolated are $[K(2,2,2\text{-crypt})]^{1+}$ and are not involved in the formation of binary intermetallics produced by oxidation of the anionic clusters. While it is interesting and informative that these ligand-free binary clusters are excellent precursors for controllable binary intermetallics, the high cost associated with 2,2,2-crypt and the low yields of the complexes limit the potential applications of this method.

The method of bypassing the isolation of ligand-free binary clusters but still employing the same transition-metal and Zintl anion precursors, laid out in Chapter 2 of this document, expands the possibility of using Zintl anions as binary intermetallic precursors. The catalytic, electronic, and optical properties of many transition-metal / main group binary intermetallics in the nano-regime have not been investigated. The lack of preparative methods for these materials in this small size range is the culprit. While the binary nanoparticles of Ni/As phases studied in Chapter 2 may or may not have new unique chemical or industrially applicable properties, the study likely provides a generic synthetic route to binary nanoparticles of tunable phases.

References

(1) Kroto, H. W.; Heath, J. R.; Obrien, S. C.; Curl, R. F.; Smalley, R. E. *Nature* **1985**, *318*, 162-163.

(2) Dabbousi, B. O.; Bawendi, M. G.; Onitsuka, O.; Rubner, M. F. *Appl. Phys. Lett.* **1995**, *66*, 1316-1318.

(3) Alivisatos, A. P. *Science* **1996**, *271*, 933-937.

(4) Miyake, M.; Matsumoto, H.; Nishizawa, M.; Sakata, T.; Mori, H.; Kuwabata, S.; Yoneyama, H. *Langmuir* **1997**, *13*, 742-746.

(5) Kortan, A. R.; Hull, R.; Opila, R. L.; Bawendi, M. G.; Steigerwald, M. L.; Carroll, P. J.; Brus, L. E. *J. Amer. Chem. Soc.* **1990**, *112*, 1327-1332.

(6) Chen, C.-C.; Chao, C.-Y.; Lang, Z.-H. *Chem. Mat.* **2000**, *12*, 1516-1518.

(7) Lu, J.; Xie, Y.; Jiang, X.; He, W.; Du, G. *J. Mater. Chem.* **2001**, *11*, 3281-3284.

(8) Stamm, K. L.; Gamo, J. C.; Liu, G. Y.; Brock, S. L. *J. Am. Chem. Soc.* **2003**, *125*, 4038-4039.

(9) Margitfalvi, J. L.; Borbath, I.; Lazar, K.; Tfirst, E.; Szegedi, A.; Hegedus, M.; Gobolos, S. *J Catal* **2001**, *203*, 94-103.

(10) Stagg, S. M.; Querini, C. A.; Alvarez, W. E.; Resasco, D. E. *J Catal* **1997**, *168*, 75-94.

(11) Arana, J.; de la Piscina, P. R.; Llorca, J.; Sales, J.; Homs, N.; Fierro, J. L. G. *Chem. Mat.* **1998**, *10*, 1333-1342.

(12) Herron, N.; Calabrese, J. C.; Farneth, W. E.; Wang, Y. *Science* **1993**, *259*, 1426-1428.

(13) Cumberland, S. L.; Hanif, K. M.; Javier, A.; Khitrov, G. A.; Strouse, G. F.; Woessner, S. M.; Yun, C. S. *Chem. Mat.* **2002**, *14*, 1576-1584.

(14) Osterloh, F. E.; Hewitt, D. P. *Chem. Comm.* **2003**, 1700-1701.

(15) Gardner, D. R.; Eichhorn, B. W.; Fettinger *Angew. Chem. Int. Ed. Engl.* **1996**, *35*, 2852-2853.

(16) Eichhorn, B. W.; Haushalter, R. C.; Huffman, J. C. *Angew. Chem. Int. Ed. Engl.* **1989**, *28*, 1032-1033.

(17) Charles, S.; Eichhorn, B. W.; Fettinger, J. C.; Bott, S. G. *Inorg. Chem.* **1996**, *35*, 1540-1548.

(18) Charles, S.; Bott, S. G.; Rheingold, A. L.; Eichhorn, B. W. *J. Am. Chem. Soc.* **1994**, *116*, 8077-8086.

(19) Joannis, A. *Comp. Rend.* **1891**, *113*, 795-798.

(20) Joannis, A. *Comp. Rend.* **1892**, *114*, 585-587.

(21) Joannis, A. *Ann. Chim. Phys.* **1906**, *7*, 75.

(22) Kraus, C. A. *J. Am. Chem. Soc.* **1907**, *29*, 1557-1571.

(23) Smyth, F. H. *J. Am. Chem. Soc.* **1917**, *39*, 1299-1312.

(24) Peck, E. B. *J. Am. Chem. Soc.* **1918**, *40*, 335-347.

(25) Kraus, C. A. *J. Am. Chem. Soc.* **1922**, *44*, 1216-1239.

(26) Zintl, E.; Goubeau, J.; Dullenkopf, W. *Z. Phys. Chem. Abt. A* **1931**, *154*, 1.

(27) Zintl, E.; Harder, A. *Z. Phys. Chem. Abt. A* **1931**, *154*, 47.

(28) Zintl, E., Dullenkopf, W. *Z. Phys. Chem. Abt. B* **1932**, *16*.

(29) Diehl, L.; Kummer, D. *Angew. Chem. Int. Ed. Engl.* **1970**, *9*, 895.

(30) Tehan, F. J.; Barnett, B. L.; Dye, J. L. *J. Amer. Chem. Soc.* **1974**, *96*, 7203-7208.

(31) Adolphson, D. G.; Corbett, J. D.; Merryman, D. J. *J. Am. Chem. Soc.* **1976**, *98*, 7234-7239.

(32) Belin, C. H. E.; Corbett, J. D.; Cisar, A. *J. Am. Chem. Soc.* **1977**, *99*, 7163-7169.

(33) Schmettow, W. v. S., H. G. *Angew. Chem. Int. Ed. Engl.* **1977**, *16*, 857.

(34) Critchlow, S. C.; Corbett, J. D. *J. Am. Chem. Soc.* **1983**, *105*, 5715-5716.

(35) Critchlow, S. C.; Corbett, J. D. *Inorg. Chem.* **1984**, *23*, 770-774.

(36) Edwards, P. A.; Corbett, J. D. *Inorg. Chem.* **1977**, *16*, 903-907.

(37) Corbett, J. D.; Edwards, P. A. *J. Am. Chem. Soc.* **1977**, *99*, 3313-3317.

(38) Cisar, A.; Corbett, J. D. *Inorg. Chem.* **1977**, *16*, 2482-2487.

(39) Corbett, J. D. *Inorg. Chem.* **1968**, *7*, 198-&.

(40) Couch, T. W.; Corbett, J. D.; Lokken, D. A. *Inorg. Chem.* **1972**, *11*, 357-&.

(41) Belin, C. H. E. *J. Amer. Chem. Soc.* **1980**, *102*, 6036-6040.

(42) Baudler, M. *Angew. Chem. Int. Ed. Engl.* **1987**, *26*, 419-441.

(43) Fritz, G.; Hoppe, K. D.; Hönle, W.; Weber, D.; Mujica, C.; Manriquez, V.; von Schnering, H. G. *J. Organomet. Chem.* **1983**, *249*, 63-80.

(44) von Schnering, H. G.; Wolf, J.; Weber, D.; Ramirez, R.; Meyer, T. *Angew. Chem. Int. Ed. Engl.* **1986**, *25*, 353-354.

(45) Charles, S.; Eichhorn, B. W.; Bott, S. G.; Fettinger, J. C. *J. Am. Chem. Soc.* **1996**, *118*, 4713-4714.

(46) Kesanli, B.; Charles, S.; Lam, Y.-F.; Fettinger, J. C.; Eichhorn, B. W. *J. Am. Chem. Soc.* **2000**, *122*, 11101-11107.

(47) Baudler, M.; Etzbach, T. *Angew. Chem. Int. Ed. Engl.* **1991**, *30*, 580-582.

(48) Bolle, U.; Tremel, W. *J. Chem. Soc., Chem. Commun.* **1994**, 217-219.

(49) Charles, S.; Eichhorn, B. W.; Bott, S. G. *J. Am. Chem. Soc.* **1993**, *115*, 5837-5838.

(50) Kesanli, B.; Fettinger, J.; Eichhorn, B. *J. Amer. Chem. Soc.* **2003**, *125*, 7367-7376.

(51) Kesanli, B.; Fettinger, J.; Scott, B.; Eichhorn, B. *Inorg. Chem.* **2004**, *43*, 3840-3846.

(52) Urnezius, E.; Brennessel, W. W.; Cramer, C. J.; Ellis, J. E.; Schleyer, P. V. *Science* **2002**, *295*, 832-834.

(53) Lewis, K. L.; Savage, J. A.; Marsh, K. J.; Jones, A. P. C. *Proceedings of SPIE-The International Society for Optical Engineering* **1983**, *400*, 21-28.

(54) Nicolau, Y. F.; Dupuy, M.; Brunel, M. *J. Electrochem. Soc.* **1990**, *137*, 2915-2924.

(55) O'Brien, P.; Nomura, R. *J. Mater. Chem.* **1995**, *5*, 1761-1773.

(56) Jones, A. C. *Chem. Soc. Rev.* **1997**, *26*, 101-110.

(57) Gammon, D.; Snow, E. S.; Shanabrook, B. V.; Katzer, D. S.; Park, D. *Science* **1996**, *273*, 87-90.

(58) Cumberbatch, T. J.; Putnis, A. *Materials Research Society Symposium Proceedings* **1990**, *164*, 129-134.

(59) Robbins, M.; Hauser, J. J.; Plewes, J. T. *J. Electrochem. Soc.* **1986**, *133*, C323.

(60) Senzaki, Y.; Gladfelter, W. L. *Abstr. Pap. Am. Chem. Soc.* **1993**, *206*, 27-INOR.

(61) Gopalakrishnan, J.; Pandey, S.; Rangan, K. K. *Chem. Mat.* **1997**, *9*, 2113-2116.

(62) Massalski, T. B. M., Joanne L.; Bennett, Lawrence H.; Baker, Hugh . *Binary alloy phase diagrams*; American Society for Metals: Metal Park, 1986.

(63) Carmalt, C. J.; Morrison, D. E.; Parkin, I. P. *Polyhedron* **2000**, *19*, 829-833.

(64) Boyen, H. G.; Kaestle, G.; Weigl, F.; Koslowski, B.; Dietrich, C.; Ziemann, P.; Spatz, J. P.; Riethmueller, S.; Hartmann, C.; Moeller, M.; Schmid, G.; Garnier, M. G.; Oelhafen, P. *Science* **2002**, *297*, 1533-1536.

(65) Guczi, L.; Petoe, G.; Beck, A.; Frey, K.; Geszti, O.; Molnar, G.; Daroczi, C. *J. Amer. Chem. Soc.* **2003**, *125*, 4332-4337.

(66) Shaw, G. A.; Parkin, I. P. *Inorg. Chem.* **2001**, *40*, 6940-6947.

(67) Perera, S. C.; Tsoi, G.; Wenger, L. E.; Brock, S. L. *J. Amer. Chem. Soc.* **2003**, *125*, 13960-13961.

(68) Brock, S. L.; Perera, S. C.; Stamm, K. L. *Chem.-Eur. J.* **2004**, *10*, 3364-3371.

(69) Xie, Y.; Lu, J.; Yan, P.; Jiang, X.; Qian, Y. *Chem. Lett.* **2000**, 114-115.

(70) Zhang, X. M.; Wang, C.; Qian, X. F.; Xie, Y.; Qian, Y. T. *J. Solid State Chem.* **1999**, *144*, 237-239.

(71) Malik, M. A.; Revaprasadu, N.; O'Brien, P. *Chem. Mat.* **2001**, *13*, 913-920.

(72) Ward, J. *The Artifacts of R. Buckminster Fuller: A Comprehensive Collection of his Designs and Drawings*; Garland Publishing, Inc.: New York, 1984; Vol. 3.

(73) Fassler, T. F. *Angew. Chem.-Int. Edit.* **2001**, *40*, 4161-4165.

(74) Sevov, S. C.; Corbett, J. D. *Science* **1993**, *262*, 880-883.

(75) Bobev, S.; Sevov, S. C. *J. Amer. Chem. Soc.* **1999**, *121*, 3795-3796.

(76) Shen, M. Z.; Schaefer, H. F. *J. Chem. Phys.* **1994**, *101*, 2261-2266.

(77) Scherer, O. J. *Angew. Chem.-Int. Edit.* **2000**, *39*, 1029-+.

(78) Ha, T. K.; Suleimenov, O.; Nguyen, M. T. *Chem. Phys. Lett.* **1999**, *315*, 327-334.

(79) Moses, M. J.; Fettinger, J. C.; Eichhorn, B. W. *Science* **2003**, *300*, 778-781.

(80) Baruah, T.; Zope, R. R.; Richardson, S. L.; Pederson, M. R. *Physical Review B: Cond. Mat. Mater. Phys.* **2003**, *68*, 241404/241401-241404/241404.

(81) Mednikov Eugeny, G.; Ivanov Sergei, A.; Dahl Lawrence, F. *Angew. Chem. Int. Ed. Eng. 20*, *42*, 323-327.

(82) Olmstead, M. M.; de Bettencourt-Dias, A.; Duchamp, J. C.; Stevenson, S.; Dorn, H. C.; Balch, A. L. *J. Amer. Chem. Soc.* **2000**, *122*, 12220-12226.

(83) Hawkins, J. M.; Meyer, A.; Lewis, T. A.; Loren, S., Eds. *Fullerenes* American Chemical Society: Washington, DC, 1992.

(84) Fenske, D.; Merzweiler, K.; Ohmer, J. *Angew. Chem.* **1988**, *100*, 1572-1573.

(85) Rieck, D. F.; Montag, R. A.; McKechnie, T. S.; Dahl, L. F. *J. Amer. Chem. Soc.* **1986**, *108*, 1330-1331.

(86) Ceriotti, A.; Demartin, F.; Heaton, B. T.; Ingallina, P.; Longoni, G.; Manassero, M.; Marchionna, M.; Masciocchi, N. *J. Chem. Soc., Chem. Commun.* **1989**, 789-787.

(87) Rheingold, A. L.; Foley, M. J.; Sullivan, P. J. *J. Am. Chem. Soc.* **1982**, *104*, 4727-4749.

(88) Wade, K. J. *Adv. Inorg. Chem. Radiochem.* **1976**, *18*, 1.

(89) Mingos, D. M. P. *Nature-Physical Science* **1972**, *236*, 99-&.

(90) Lauher, J. W. *J. Amer. Chem. Soc.* **1978**, *100*, 5305-5315.

(91) Evans, D. F. *J. Chem. Soc., Abst.* **1959**, 2003-2005.

(92) Albano, V. G.; Demartin, F.; Iapalucci, M. C.; Laschi, F.; Longoni, G.; Sironi, A.; Zanello, P. *J. Chem. Soc.-Dalton Trans.* **1991**, 739-749.

(93) Vidal, J. L.; Troup, J. M. *J. Organomet. Chem.* **1981**, *213*, 351-363.

(94) Eichhorn, B. W.; Matamanna, S. P.; Gardner, D. R.; Fettinger, J. C. *J. Am. Chem. Soc.* **1998**, *120*, 9708-9709.

(95) Moses, M. J.; Fettinger, J.; Eichhorn, B. *J. Am. Chem. Soc.* **2002**, *124*, 5944-5945.

(96) Kesanli, B.; Fettinger, J.; Gardner, D. R.; Eichhorn, B. *J. Amer. Chem. Soc.* **2002**, *124*, 4779-4786.

(97) Singleton, M. N., P., Ed.; American Society for Metals: Metal Park, 1986.

(98) *Natl. Bur. Stand. (U.S.)* **1960**, *539*, 42.

(99) Berry, T. *Mem. Geol. Soc. Amer.* **1962**, *85*, 62.

(100) Kesanli, B., 2002.

(101) Gallucci, J. C.; Doecke, C. W.; Paquette, L. A. *J. Amer. Chem. Soc.* **1986**, *108*, 1343-1344.

(102) Baruah, T.; Pederson, M. R.; Zope, R. R.; Beltran, M. R. *Chem. Phys. Lett.* **2004**, *387*, 476-480.

(103) Baruah, T.; Zope, R. R.; Richardson, S. L.; Pederson, M. R. *Abstracts of Papers, 228th ACS National Meeting, Philadelphia, PA, United States, August 22-26, 2004* **2004**, INOR-660.

(104) Oyama, S. T.; Clark, P.; Wang, X.; Shido, T.; Iwasawa, Y.; Hayashi, S.; Ramallo-Lopez, J. M.; Requejo, F. G. *J. Phys. Chem. B* **2002**, *106*, 1913-1920.

(105) Tegus, O.; Brick, E.; Buschow, K. H. J.; de Boer, F. R. *Nature* **2002**, *415*, 150-152.

(106) Ravindran, P.; Delin, A.; James, P.; Johansson, B.; Wills, J. M.; Ahuja, R.; Eriksson, O. *Physical Review B: Cond. Mat. Mater. Phys.* **1999**, *59*, 15680-15693.

(107) Cao, Y. C.; Jin, R.; Mirkin, C. A. *Science* **2002**, *297*, 1536-1540.

(108) Huang, M. H.; Mao, S.; Feick, H.; Yan, H.; Wu, Y.; Kind, H.; Weber, E.; Russo, R.; Yang, P. *Science* **2001**, *292*, 1897-1899.

(109) Huang, Y.; Duan, X.; Cui, Y.; Lauhon, L. J.; Kim, K. H.; Lieber, C. M. *Science* **2001**, *294*, 1313-1317.

(110) Lieber, C. M. *Solid State Comm.* **1998**, *107*, 607-616.

(111) Choi, S. Y.; Lee, S. C.; Lee, H. J.; Ahn, H. S.; Kim, S. W.; Ryu, J. Y. *Physical Review B: Cond. Mat. Mater. Phys.* **2002**, *66*, 155208/155201-155208/155212.

(112) Lu, J.; Wei, S.; Yu, W.; Zhang, H.; Qian, Y. *Inorg. Chem.* **2004**, *43*, 4543-4545.

(113) Coetzer, J.; Louw, V. I. *Chem. Abstr.* **1995**, *122*, 60155b.

(114) Aronsson, B.; Landstron, T.; Rundouist, S. *Borides, Silicides and Phosphides*; Wiley: New York, 1965.

(115) Greenwood, N. N.; Earnshaw, A. *Chemistry of the Elements*; Pergamon Press: Oxford, 1984.

(116) Nesbitt, H. W.; Reinke, M. *Amer. Mineral.* **1999**, *84*, 639-649.

(117) Fleet, M. E. *Amer. Mineral.* **1972**, *57*, 1-9.

(118) Nesbitt, H. W.; Uhlig, I.; Szargan, R. *Amer. Mineral.* **2002**, *87*, 1000-1004.

(119) Fleet, M. E. *Amer. Mineral.* **1973**, *58*, 203-210.

(120) El-Boragy, M.; Bhan, S.; Schubert, K. *J. L.- C. Met.* **1970**, *22*, 445-458.

(121) Peacock *Mineral. Mag.* **1940**, *25*, 557.

(122) Heyding, C. *Can. J. Chem.* **1957**, *35*, 1205.

(123) Yund *Econ. Geol.* **1961**, *56*, 1273.

(124) Nesbitt, H. W.; Legrand, D.; Bancroft, G. M. *Phys. Chem. Mineral.* **2000**, *27*, 357-366.

(125) Bahl, M. K.; Woodall, R. O.; Watson, R. L.; Irgolic, K. J. *J. Chem. Phys.* **1976**, *64*, 1210-1218.

(126) Jackson, D. A.; Nesbitt, H. W.; Scaini, M. J.; Duggal, A.; Bancroft, G. M. *Amer. Mineral.* **2003**, *88*, 890-900.

(127) ICDD: Newtown Square, Vol. Release 1998.

(128) Zhang, J. M.; Dahl, L. F. *J. Chem. Soc.-Dalton Trans.* **2002**, 1269-1274.

(129) Ahlrichs, R.; Anson, C. E.; Clerac, R.; Fenske, D.; Rothenberger, A.; Sierka, M.; Wieber, S. *Eur. J. Inorg. Chem.* **2004**, 2933-2936.

(130) Fenske, D.; Persau, C.; Dehnen, S.; Anson, C. E. *Angew. Chem.-Int. Edit.* **2004**, *43*, 305-309.

(131) Nablant-Esenturk, E. F., J; Lam, Y-F; Eichhorn, B. *Angew. Chem.-Int. Edit.* **2004**, *43*, 2132-2134.

(132) Klemm, W. *Trabajos reunion intern. reactividad solidos, 3 Deg, Madrid, 1956* **1956**, *1*, 447-451, discussion 451-442.

(133) Klemm, W. *Proc. Chem. Soc.* **1959**, 329-341.

(134) Kauzlarich, S. M.; Editor *Chemistry, Structure, and Bonding of Zintl Phases and Ions*, 1996.

(135) Bobev, S.; Sevov, S. C. *Angew. Chem. Int. Ed.* **2000**, *39*, 4108-4110.

(136) Jeitschko, W.; Altmeyer, R. O.; Schelk, M.; Rodewald, U. C. *Z. Anorg. Allg. Chem.* **2001**, *627*, 1932-1940.

(137) O'Keeffe, M.; Brese, N. E. *Acta Cryst., Sec. B: Struct. Science* **1992**, *B48*, 152-154.

(138) Wade, K. *Chem. Br.* **1975**, *11*, 177-183.

(139) Rosch, N.; Ackermann, L.; Pacchioni, G. *Inorg. Chem.* **1993**, *32*, 2963-2964.

(140) Kesanli, B.; Gardner, D. R.; Scott, B.; Eichhorn, B. W. *J. Chem. Soc.-Dalton Trans.* **2000**, *8*, 1291-1296.

(141) Jarvis, J. A. J.; Mais, R. H. B.; Owston, P. G.; Thompson, D. T. *J. Chem. Soc. A: Inorg., Phys., Theo.* **1970**, 1867-1872.

(142) Mlynek, P. D.; Dahl, L. F. *Organometallics* **1997**, *16*, 1641-1654.

(143) Jones, R. A.; Whittlesey, B. R. *Inorg. Chem.* **1986**, *25*, 852-856.

(144) Mlynek, P. D.; Dahl, L. F. *Organometallics* **1997**, *16*, 1655-1667.

(145) Deppisch, B.; Schaefer, H. *Z. Anorg. Allg. Chem.* **1982**, *490*, 129-135.

(146) Ates, M.; Breunig, H. J.; Ebert, K.; Guelec, S.; Kaller, R.; Draeger, M. *Organometallics* **1992**, *11*, 145-150.

(147) Breunig, H. J.; Haeberle, K.; Draeger, M.; Severengiz, T. *Angew. Chem.* **1985**, *97*, 62-63.

(148) Huttner, G.; Lorenz, H. *Chem. Berichte* **1974**, *107*, 996-1008.

(149) Charles, S.; Eichhorn, B. W.; Bott, S. G. *J. Amer. Chem. Soc.* **1993**, *115*, 5837-5838.

(150) Westerhausen, M.; Weinrich, S.; Mayer, P. *Z. Anorg. Allg. Chem.* **2003**, *629*, 1153-1156.

(151) Bolle, U.; Tremel, W. *J. Chem. Soc., Chem. Commun.* **1992**, 91-93.

(152) Breunig, H. J.; Roesler, R. *Coord. Chem. Rev.* **1997**, *163*, 33-53.

(153) Haushalter, R. C.; Eichhorn, B. W.; Rheingold, A. L.; Geib, S. J. *J. Chem. Soc. Chem. Commum.* **1988**, 1027-1028.

(154) Scherer, O. J.; Wiedemann, W.; Wolmershauser, G. *Chem. Ber.* **1990**, *123*, 3-6.

(155) Tran, N. T.; Kawano, M.; Dahl, L. F. *J. Chem. Soc.-Dalton Trans.* **2001**, 2731-2748.

(156) Kawano, M.; Bacon, J. W.; Campana, C. F.; Winger, B. E.; Dudek, J. D.; Sirchio, S. A.; Scruggs, S. L.; Geiser, U.; Dahl, L. F. *Inorg. Chem.* **2001**, *40*, 2554-2569.

(157) Tran, N. T.; Powell, D. R.; Dahl, L. F. *Angew. Chem.-Int. Edit.* **2000**, *39*, 4121-4125.

(158) Lam, R.; McDonald, R.; Mar, A. *Inorg. Chem.* **2001**, *40*, 952-959.

(159) Exner, K.; Schleyer, P. v. R. *Science* **2000**, *290*, 1937-1940.

(160) Xu, L.; Sevov, S. C. *J. Am. Chem. Soc.* **1999**, *121*, 9245-9246.

(161) Brese, N. E.; O'Keeffe, M. *Acta Cryst., Sec. B: Struct. Science* **1991**, *B47*, 192-197.

(162) Harper, J. R.; Rheingold, A. L. *J. Organomet. Chem.* **1990**, *390*, C36-C38.

(163) Huttner, G.; Weber, U.; Sigwarth, B.; Scheidsteger, O. *Angew. Chem.* **1982**, *94*, 210-211.

(164) Weber, U.; Huttner, G.; Scheidsteger, O.; Zsolnai, L. *J. Organomet. Chem.* **1985**, *289*, 357-366.

(165) Cowley, A. H.; Norman, N. C.; Pakulski, M.; Bricker, D.; Russell, D. R. *J. Amer. Chem. Soc.* **1985**, *107*, 8211-8218.

(166) Bartlett, R. A.; Rasika Dias, H. V.; Hope, H.; Murray, B. D.; Olmstead, M. M.; Power, P. P. *J. Amer. Chem. Soc.* **1986**, *108*, 6921-6926.

(167) Huttner, G.; Schmid, H. G.; Frank, A.; Orama, O. *Angew. Chem. Int. Ed. Engl.* **1976**, *15*, 224.

(168) Foust, A. S.; Foster, M. S.; Dahl, L. F. *J. Am. Chem. Soc.* **1969**, *91*, 5631-5633.

(169) DiMaio, A. J.; Rheingold, A. L. *J. Chem. Soc., Chem. Comm.* **1987**, 404-405.

(170) Laikov, D. N. *Chem. Phys. Lett.* **1997**, *281*, 151-156.

(171) Ustynyuk, Y. A.; Ustynyuk, L. Y.; Laikov, D. N.; Lunin, V. V. *J. Organomet. Chem.* **2000**, *597*, 182-189.

(172) Parr, R. G.; Yang, W. *Density-functional theory of atoms and molecules*; Oxford University Press: Oxford, 1989.

(173) Perdew, J. P.; Burke, K.; Ernzerhof, M. *Phys. Rev. Lett.* **1996**, *77*, 3865-3868.

(174) Stevens, W. J.; Basch, H.; Krauss, M. *J. Chem. Phys.* **1984**, *81*, 6026-6033.

(175) Stevens, W. J.; Basch, H.; Krauss, M.; Jasien, P. *Can. J. Chem.* **1992**, *70*.

(176) Cundari, T. R.; Stevens, W. J. *J. Chem. Phys.* **1993**, *98*.

(177) Liao, H. W.; Wang, Y. F.; Zhang, S. Y.; Qian, Y. T. *Chem. Mat.* **2001**, *13*, 6-+.

(178) Hessen, B.; Siegrist, T.; Palstra, T.; Tanzler, S. M.; Steigerwald, M. L. *Inorg. Chem.* **1993**, *32*, 5165-5169.

(179) Kesanli, B.; Charles, S.; Lam, Y.-F.; Fettinger, J. C.; Eichhorn, B. W. *J. Am. Chem. Soc.* **2000**, *122*, 11101-11107.

(180) Meyer, M.; Wallberg, C.; Kurihara, K.; Fendler, J. H. *J. Chem. Soc., Chem. Comm.* **1984**, 90-91.

(181) Ingert, D.; Pileni, M.-P. *Adv. Func. Mater.* **2001**, *11*, 136-139.

(182) Watzke, H. J.; Fendler, J. H. *J Phys Chem-Us* **1987**, *91*, 854-861.

(183) Hazra, P.; Chakrabarty, D.; Chakraborty, A.; Sarkar, N. *Chem. Phys. Lett.* **2003**, *382*, 71-80.

(184) Samii, A. A. Z.; De Savignac, A.; Rico, I.; Lattes, A. *Tetrahedron* **1985**, *41*, 3683-3688.

(185) Rico, I.; Lattes, A. *Surf. Science Ser.* **1987**, *24*, 357-375.

(186) Riter, R. E.; Kimmel, J. R.; Undiks, E. P.; Levinger, N. E. *J. Phys. Chem. B* **1997**, *101*, 8292-8297.

(188) Thommassen *Z. Phys. Chem.* **1929**, *4*, 280.

(189) Saini, e. a. *Can. J. Chem.* **1964**, *42*, 620.

(190) Baudler, M.; Glinka, K. *Chem. Rev.* **1993**, *93*, 1623-1667.

(191) von Schnering, H. G. *Angew. Chem. Int. Ed. Engl.* **1981**, *20*, 33-51.

(192) Baudler, M.; Duester, D.; Langerbeins, K.; Germeshausen, J. *Angew. Chem.* **1984**, *96*, 309-310.

(193) Haushalter, R. C.; Goshorn, D. P.; Sewchok, M. G.; Roxlo, C. B. *Mat. Res. Bull.* **1987**, *22*, 761-768.

(194) Ahlrichs, R.; Fenske, D.; Fromm, K.; Krautscheid, H.; Krautscheid, U.; Treutler, O. *Chem. Eur. J.* **1996**, *2*, 238-244.

(195) Nienhaus, A.; Hauptmann, R.; Fassler, T. F. *Angew. Chem. Int. Ed.* **2002**, *41*, 3213-+.

(196) Yoshifuji, M.; Shima, I.; Inamoto, N.; Hirotsu, K.; Higuchi, T. *J. Am. Chem. Soc.* **1981**, *103*, 4587-4589.

(197) Yoshifuji, M.; Hashida, T.; Inamoto, N.; Kirotsu, K.; Horiuchi, T.; Higuchi, T.; Ito, K.; Nagase, S. *Angew. Chem. Int. Ed. Engl.* **1985**, *24*, 211-212.

(198) Borm, J.; Zsolnai, L.; Huttner, G. *Angew. Chem. Int. Ed. Engl.* **1983**, *22*, 977-978.

(199) Datta, S.; Furdyna, J. K.; Gunshor, R. L. *Superlattices and Microstructures* **1985**, *1*, 327-334.

(200) Rao, C. N. R.; Gopalakrishnan, J. *New Directions in Solid State Chemistry: Structure, Synthesis, Properties, Reactivity, and Material Design*, 1986.

(201) Spanhel, L.; Anderson, M. A. *J. Amer. Chem. Soc.* **1990**, *112*, 2278-2284.

(202) Miller, G. J. In *Chemistry, Structurem and Bonding of Zintl Phases and Ions*; Kauzlarich, S. M., Ed.; VCH Publishers, Inc.: New York, 1996, pp 1-59.

(203) Li, J.; Wu, K. C. *Inorg. Chem.* **2000**, *39*, 1538-1544.

(204) Bobev, S.; Thompson, J. D.; Sarrao, J. L.; Olmstead, M. M.; Hope, H.; Kauzlarich, S. M. *Inorg. Chem.* **2004**, *43*, 5044-5052.

(205) Haeussermann, U.; Woerle, M.; Nesper, R. *J. Amer. Chem. Soc.* **1996**, *118*, 11789-11797.

(206) Xu, Z.; Guloy, A. M. *J. Amer. Chem. Soc.* **1998**, *120*, 7349-7350.